

Ludwig–Maximilians–Universität



The Formation of Dark Matter Halos and High-Redshift Galaxies

Dissertation an der Fakultät für Physik
der Ludwig–Maximilians–Universität München
für den Grad des
Doctor rerum naturalium

vorgelegt von
Shy Genel
aus Herzliya, Israel

München, den 16.12.2010

Erstgutachter: Prof. Dr. Reinhard Genzel
Zweitgutachter: Prof. Dr. Andreas Burkert
Tag der mündlichen Prüfung: 11.03.2011

To my grandmother
and my parents

לסבתי ולחורי

Die Blumen erreicht der Fuß so leicht,
Auch werden zertreten die meisten;
Man gehe vorbei und tritt entzwei
Dir blöden wie die dreisten.

Die Perlen ruhn in Meerestruhn,
Doch weiß man sie aufzuspüren;
Man bohrt ein Loch und spannt sie ins Joch,
Ins Joch von seidenen Schnüren.

Die Sterne sind klug, sie halten mit Fug
Von unserer Erde sich ferne;
Am Himmelszelt, als Lichter der Welt,
Stehn ewig sicher die Sterne.

Heinrich Heine, Kluge Sterne

Contents

Contents	1
Zusammenfassung	9
Abstract	11
1 Introduction	13
1.1 Galaxy formation in the Λ CDM cosmological model	13
1.1.1 The homogeneous Λ CDM Universe	13
1.1.2 Cosmic structure formation	15
1.1.3 Modeling galaxy formation	16
1.2 High-redshift galaxies	17
1.2.1 Observed star-forming galaxies at $z \approx 2$	17
1.2.2 An emerging new theoretical understanding	21
1.2.3 Modeling $z \approx 2$ star-forming galaxies	22
1.3 Mergers	24
1.3.1 The physics of mergers	24
1.3.2 Merger rates	25
1.3.2.1 Observations	25
1.3.2.2 Theory	26
1.4 Star-formation feedback in galaxy formation	27
1.5 The current work	28
1.5.1 Motivation	28
1.5.2 Thesis overview	28
2 The dark matter halo merger rate	31
2.1 Abstract	31
2.2 Introduction	32
2.3 Extracting the merger rate from the Millennium Simulation	34
2.3.1 The Millennium Simulation and its merger trees	34
2.3.2 Constructing new halo merger trees	34
2.3.3 Definitions of the merger rate	39
2.4 Results	41

2.4.1	The merger rate per progenitor halo as a function of mass ratio . . .	41
2.4.2	The major merger rate per progenitor halo	43
2.4.3	The merger rate per descendant halo	46
2.4.4	Comparison between the merger rate definitions	47
2.5	Comparison to previous work	48
2.5.1	Comparison to Fakhouri & Ma (2008)	48
2.5.2	Comparison to the EPS model	51
2.5.3	The role of the halo mass definition	52
2.6	Comparison to observations	58
2.7	Summary and discussion	62
3	Dark matter halo growth: evidence for smooth accretion	65
3.1	Abstract	65
3.2	Introduction	66
3.3	Analysis of merger trees	67
3.3.1	Method	67
3.3.2	Results from the merger trees	69
3.3.2.1	The merger rate	69
3.3.2.2	Halo growth modes	71
3.3.2.3	Comparison to the EPS model	72
3.4	Analysis of particle histories	74
3.4.1	Method	74
3.4.2	Results from the analysis of particles	76
3.4.3	The cycle of particles in and out of halos	78
3.4.4	Alternative trees and halo definitions	79
3.5	Implications for galaxy formation	83
3.6	Comparison to previous work	86
3.7	Summary	88
4	The Millennium Simulation Compared to $z \approx 2$ Galaxies	89
4.1	Abstract	89
4.2	Introduction	89
4.3	Analysis of the Millennium Simulation	91
4.3.1	The Millennium Simulation and its merger trees	91
4.3.2	Constructing new merger trees	91
4.4	Galaxies at $z \approx 2$	92
4.4.1	SINS galaxies	94
4.4.2	SMGs	96
4.5	Fate at $z = 0$	96
4.5.1	Fate of SINS galaxies	96
4.5.2	Fate of SMGs	96
4.6	Summary	99

5	Short-lived giant clumps in $z \approx 2$ disks	101
5.1	Abstract	101
5.2	Introduction	101
5.3	The Simulations: Code and Setup	103
5.4	Results	104
5.5	Comparison to observations	109
5.6	Summary and discussion	113
6	Summary and prospects	115
A	Analytic conversion of merger rate definitions	121
B	Using the substructure to find the end point of mergers	123
	Bibliography	129
	Acknowledgements	141
	Curriculum Vitae	143
	Publication List	145

List of Figures

1.1	Clumpy $z \approx 2$ galaxies	19
1.2	SINS galaxies	20
1.3	Continuum and $H\alpha$ clumps	21
2.1	Temporary FOF groups	35
2.2	Mass functions comparison	38
2.3	The merger rate per progenitor halo	40
2.4	The major merger rate per progenitor halo	43
2.5	The major merger rate per descendant halo	44
2.6	Comparing merger tree construction algorithms as a function of mass ratio	49
2.7	Comparing merger tree construction algorithms for minor mergers	50
2.8	Comparison to the EPS model	53
2.9	Comparing halo mass definitions for approaching mergers	55
2.10	Comparing the merger rate with different halo mass definitions	56
2.11	The role of environment in the comparison of halo mass definitions	57
2.12	Mean mass growth histories for halos that are about to undergo a merger .	59
2.13	The merger fraction as a function of redshift	61
3.1	The merger rate per unit time	70
3.2	The relative contribution of mergers as a cumulative function of mass ratio	73
3.3	The ratio of the merger rate predicted from EPS to our global fit	74
3.4	The fraction of the particles originating from the three accretion modes . .	77
3.5	The fraction of the three modes in the net accretion	79
3.6	The ratio of the gross inflow rate to the net growth rate	80
3.7	Comparison of the contribution of the accretion modes with different trees	81
3.8	Comparison of different simulations and halo definitions	82
3.9	The fraction of mass accretion that arrives smoothly	85
4.1	Halos and galaxies in the mass-accretion rate plane	93
4.2	Comparison of dark matter accretion rates and SFRs	95
4.3	The number of future major mergers	97
4.4	Mass growth to $z = 0$	98
5.1	Global properties of six 'zoom-in' simulations at $z = 2$	105

5.2	Gas properties of the central galaxy <i>s224</i> at $z = 2$	106
5.3	Clump evolution with and without winds	110
5.4	Mock H α line observations	111
5.5	Mock continuum observations	112
B.1	Mass and spatial evolution of subhalos	124
B.2	Spatial subhalo separations before disruption	127
B.3	The fraction of 'open-ended' mergers	128

List of Tables

2.1	Merger scenarios	36
2.2	Fits for the merger rate	42
4.1	Properties of galaxy samples at $z \approx 2$	90
5.1	Galaxy and clump properties	107

Zusammenfassung

Im Λ CDM Modell der Kosmologie entstehen Galaxien in den Zentren von Dunkle-Materie Halos und verschmelzen miteinander, folgend der Verschmelzungen ihrer Wirtshalos. Ausgehend von dieser Grundannahme, quantifizieren wir die Wachstumsmechanismen Dunkler-Materie Halos. Dazu analysieren wir diverse große Vielkörper-Simulationen des Wachstums und der Entwicklung kosmischer Strukturen. Wir entwickeln einen neuartigen Verschmelzungsbaumbaualgorithmus, der in geeigneter Weise die Fragmentation der Halos berücksichtigt. In unseren Untersuchungen finden wir, dass sich die Verschmelzungsrate stark mit der Rotverschiebung ändert, aber nur wenig abhängig ist von der Masse. Weiterhin finden wir eine universelle Proportionalität zwischen Verschmelzungen verschiedener Massenquotienten (z.B. "Major-" und "Minor-Mergers", d.h. Verschmelzungen von Halos mit ähnlichen bzw. stark unterschiedlichen Massen). Wir zeigen auch, dass die Verschmelzungsrate pro Vorläuferhalo (bezogen auf zukünftige Verschmelzungen und auf die Anzahl von Galaxienpaaren) kleiner ist als die Verschmelzungsrate pro Nachkommehalo (bezogen auf vergangene Verschmelzungen und die Anzahl von Galaxien mit unregelmäßigen Morphologien). Weiterhin unterscheiden sie sich in ihren Abhängigkeiten von Rotverschiebung und Masse. Innerhalb der begrenzten Auflösung der Simulation finden wir, dass nur $\approx 60\%$ der von Halos akkretierten Masse aus Verschmelzungen stammt. Der Funktionsverlauf der Verschmelzungsrate allerdings deutet darauf hin, dass der gesamte Anteil von Verschmelzungen nicht höher als dieser Wert ist. Mithilfe der Analyse von vollständigen Teilchenentwicklungshistorien bestätigen wir, dass ein signifikanter Anteil der Halo-Teilchen aus gleichmäßiger Akkretion entstammt. Das hat wichtige Implikationen für die Gleichmäßigkeit der Akkretion von Gas.

Scheibengalaxien bei $z \approx 2$ haben hohe Sternentstehungsraten, zeigen aber gleichzeitig eine geordnete Rotation - indikativ für eine geringe Verschmelzungsaktivität. Wir verwenden eine große Dunkle-Materie-Simulation um zu zeigen, dass sogar nicht-verschmelzende Halos bei $z \approx 2$ schnell genug wachsen, um die beobachteten hohen Sternentstehungsraten zu erklären. Zudem verfolgen wir diese Halos bis $z = 0$, wobei wir feststellen, dass viele von diesen keinerlei Major-Mergers durchlaufen. Die $z \approx 2$ Scheibengalaxien zeigen weiterhin hohe Geschwindigkeitsdispersionen und irreguläre, klumpige, Morphologien. Wir führen spezielle "zoom-in" kosmologische hydrodynamische Simulationen durch, die sich auf die Entwicklung von einzelnen $z \approx 2$ Galaxien konzentrieren. Dabei sehen wir, dass irreguläre, klumpige Morphologien aus gravitationellen Instabilitäten folgen, in denen eine hohe Geschwindigkeitsdispersion dazu führt, dass die Größenordnung der Jeans-

Skalen derjenigen der beobachteten größten Materieverdichtungen ("Clumps") vergleichbar wird. Rückkopplung durch Sternentstehung wird in unserem Modell durch galaktische Winde abgebildet, wobei die Massenausflussraten höher als die Sternentstehungsraten sind. Diese hohen Massenausflussraten verhindern, dass die Clumps virialisieren. Etwa innerhalb einer halben Rotationsperiode einer Galaxie verlieren diese Clumps einen Großteil ihrer Masse, was dazu führt, dass diese aufhören zu kollabieren und (im Folgenden) aufbrechen. Ihre Lebensdauer ist somit kurz und sie migrieren daher nicht in das Zentrum ihrer Galaxie, wie es bislang üblicherweise in der Literatur beschrieben wurde. Mit Hilfe von Strahlungstransportberechnungen vergleichen wir Galaxiensimulationen mit Beobachtungen und erstellen Modell-SINFONI-Datenkuben unter Berücksichtigung reeller Beobachtungsbedingungen. Vergleichend finden wir gute Übereinstimmung zwischen Daten aus tatsächlich beobachteten Galaxien und solchen von uns simulierten im Hinblick auf Farbe, Leuchtkraft, Morphologie und Kinematik. Durch diesen Vergleich schießen wir, dass die Galaxien in unseren Simulationen plausibel realistisch sind.

Abstract

In the concordance Λ CDM cosmological model, galaxies form in the centers of dark matter halos and merge with one another following the mergers of their host halos. Thus, we set out to quantify the growth mechanisms of dark matter halos. For this purpose, we analyze several large N-body simulations of the growth of cosmic structure. We devise a novel merger tree construction algorithm that properly takes into account halo fragmentations. We find that the merger rate evolves rapidly with redshift but depends weakly on mass, and that the proportions between mergers of different mass ratios, e.g. major and minor mergers, are universal. We also show that the merger rate per progenitor halo (related to future mergers and to galaxy pair counting) is smaller than that per descendant halo (related to past mergers and galaxy disturbed morphologies), and that their redshift and mass dependencies are different. We find that only $\approx 60\%$ of the mass accreted onto halos arrives in mergers that are resolved in our simulations. Moreover, the functional form of the merger rate suggests that the merger contribution saturates at that value. Using full particle histories, we confirm that smoothly-accreted particles make a significant fraction of dark matter halos. This has important implications for the smoothness of gas accretion.

Disk galaxies at $z \approx 2$ are rapidly star-forming, but show regular rotation, indicating little merger activity. We use a large dark matter simulation to show that even non-merging $z \approx 2$ halos grow fast enough to explain observed high star-formation rates. We also follow those halos to $z = 0$, finding that many do not undergo major mergers at all. The $z \approx 2$ disks also show high velocity dispersions and irregular clumpy morphologies. We run "zoom-in" cosmological hydrodynamical simulations focusing on the formation of individual $z \approx 2$ galaxies. We find that the clumpy morphologies are a result of gravitational instability, where the high random motions make the (turbulent) Jeans scales as large as the observed giant clumps. Star-formation feedback in our model is implemented as galactic winds with high mass-loading factors. We find that the high mass-loading factors prevent the clumps from virializing. Within roughly half a disk orbital time, they lose a large fraction of their mass, such that they stop collapsing and disrupt. Thus, their lifetimes are short and they do not migrate to the galaxy centers as has been proposed in the literature so far. We compare simulated galaxies to observations using radiative transfer calculations, and by creating mock SINFONI/VLT data cubes with realistic "observing conditions". We find good agreement between "observed" simulated galaxies and real observed ones, in terms of their luminosities, colors, morphologies and kinematics. With this comparison, we conclude that the galaxies formed in our simulations are plausibly realistic.

Chapter 1

Introduction

1.1 Galaxy formation in the Λ CDM cosmological model

1.1.1 The homogeneous Λ CDM Universe

The past two decades have witnessed a wealth of ground-breaking discoveries in Astrophysics and Cosmology. With the advent of new missions, ground-based as well as spaceborne, our knowledge about our Universe, and in particular the young Universe, has much improved. Perhaps most fundamental is the emergence of a concordance cosmological model, according to which the contents of the Universe are dominated by a cosmological constant Λ and Cold Dark Matter - hence the Λ CDM model.

This model is based on the classical Hot Big Bang model, according to which we live in an expanding Universe that is homogeneous and isotropic on large scales, and is therefore described by the Friedmann-Robertson-Walker metric. As the age of the Universe $t \rightarrow 0$, the temperature $T \rightarrow \infty$. In that regime the familiar physical laws break down, so we can only describe the Universe starting from temperatures lower than the Planck scale. However, it is attractive to postulate that the expansion of the Universe began with an Inflationary epoch that made the Universe homogeneous and flat (Guth, 1981). After the end of Inflation, the Universe continued expanding according to the Friedmann equations:

$$H^2 \equiv \left(\frac{\dot{a}}{a}\right)^2 = \frac{8\pi G}{3}\rho - \frac{kc^2}{a^2} + \frac{\Lambda c^2}{3} \quad (1.1)$$

$$\frac{\ddot{a}}{a} = -\frac{4\pi G}{3}\left(\rho + \frac{3p}{c^2}\right) + \frac{\Lambda c^2}{3}, \quad (1.2)$$

where H is the Hubble constant, a is the scale factor, G is Newton's gravitational constant and c the speed of light, k is the curvature of the Universe, ρ is the matter and radiation density of the Universe and p their pressure, and Λ is the cosmological constant.

At early times, or redshift $z \equiv \frac{a_0}{a} - 1 \gtrsim 3000$ (a_0 being a at the current epoch), photons dominated the energy density of the Universe, but after that epoch of matter-radiation-

equality it is matter that became dominant. The matter density is dominated by dark matter, which is composed of non-standard elementary particles (yet to be identified, see Feng (2010) for a review on particle candidates and detection methods) that are effectively collisionless. The dominant ($\approx 70\%$) term in the first Friedmann equation at the current epoch is, however, the Λ term. The cosmological constant can be interpreted in two ways: either as a constant of Nature that appears as an integration constant in Einstein's equations and does not represent a true physical entity, or as a constant density that does not evolve with a , which can be interpreted as a vacuum energy. Only a few Gigayears ago, at $z \approx 1$, the matter became dilute enough, due to the expansion of space, that the cosmological constant term became dominant, causing the Universe to accelerate its expansion. A generalised idea of the vacuum energy concept is "dark energy", which can have a different equation of state than constant density. That equation of state, and therefore density evolution, is not yet well constrained, but current observations are consistent with the simplest form of a constant Λ .

The fundamental cosmological parameters have been measured more and more precisely in recent years, and a field of "precision cosmology" has emerged (e.g. Spergel et al., 2007; Komatsu et al., 2009). These measurements are based on several types of observations.

- The anisotropies in the cosmic microwave background (CMB) radiation, constraining the curvature of the Universe, its matter and baryon densities, and the primordial power spectrum of perturbations (Dunkley et al., 2009).
- The distance to high-redshift supernovae, which serve as "standard candles", constraining the expansion history of the Universe and thereby providing evidence for a cosmological constant or dark energy (Riess et al., 1998; Perlmutter et al., 1999).
- Baryonic acoustic oscillations (BAO) measured in the large-scale galaxy distribution serve as "standard rulers", constraining the cosmic expansion history, and thereby the equation of state of dark energy (Blake & Glazebrook, 2003).
- Weak lensing, constraining the cosmic matter density and the primordial power spectrum of perturbations (Hoekstra et al., 2002).
- Big Bang nucleosynthesis, constraining the cosmic baryon density (Yang et al., 1984; Iocco et al., 2009).

Specifically, several lines of argument exist for the existence of dark matter.

- Historically it was proposed in order to explain the inferred virial mass of the Coma cluster, which is much larger than its luminous mass (Zwicky, 1933). This argument, namely that the mass content of galaxy clusters is significantly larger than their baryonic masses, still holds today, and is aided by mass measurements from strong and weak gravitational lensing (e.g. the "bullet cluster"; Clowe et al., 2004).
- The fact that the rotation curves of spiral galaxies are flat or rising rather than falling at large radii, where the visible mass becomes very small, suggests that there is

unvisible, or "dark", mass in large abundance in the outskirts of galaxies (Oort, 1940; Ostriker et al., 1974; Faber & Gallagher, 1979; Rubin et al., 1980). This argument, though, is where modified gravity theories like MOND (Milgrom, 1983b) have been most successful suggesting an alternative (Milgrom, 1983a).

- The theory of Big Bang nucleosynthesis as well as observations in the local Universe strongly suggest a cosmic baryon content that is more than an order of magnitude smaller than the critical density of the Universe (Yang et al., 1984; Iocco et al., 2009; Fukugita et al., 1998), while CMB observations suggest that the Universe is flat, i.e. that it does have the critical density.
- A crucial argument in favor of non-baryonic dark matter is that the non-linear density contrasts in the local Universe would not have had enough time to evolve from the tiny anisotropies observed in the CMB at $z \approx 1100$, unless already at that time there had been underlying, "dark", stronger anisotropies (Silk & Wilson, 1981; Wilson & Silk, 1981; Bond & Efstathiou, 1984). This leads us to the formation of cosmic structures.

1.1.2 Cosmic structure formation

The cosmic large-scale structure is formed when primordial (weak) density fluctuations are amplified by gravitational instability. The fluctuations are thought to be Gaussian and have (at least nearly) a flat $n = 1$ Harrison-Zel'Dovich (Harrison, 1970; Zel'Dovich, 1972) power spectrum. These fluctuations originate from quantum fluctuations of the inflaton field that are spatially blown up during Inflation (Hawking, 1982; Guth & Pi, 1982, 1985). The gravitational growth of the minuscule density fluctuations is linear at early epochs, but ever larger mass scales enter, as cosmic time goes by, into a non-linear regime of gravitational collapse (Zel'Dovich, 1970; Press & Schechter, 1974). Since dark matter dominates the mass budget, it is the nature of dark matter that determines the evolution of the fluctuations. In the current paradigm dark matter is "cold" (CDM; Peebles, 1982; Blumenthal et al., 1984), a term reflecting the negligible thermal motions that dark matter particles had when galaxy-scale fluctuations entered the horizon. Thus, the primordial fluctuations evolve, throughout cosmic time, into the "Cosmic Web", characterised by sheets, filaments and voids. Embedded within this web are virialized regions, i.e. dark matter halos, which grow hierarchically from small progenitors to massive descendants, and merge with one another.

The highly non-linear nature of structure formation lends numerical cosmological simulations the only tool for detailed studies of this process. Those are computationally expensive, but are an *ab initio* tool. The results of N-body (collisionless) simulations are fairly robust to the freedom in choices of the gravitational softening kernel or temporal integration algorithms, and the initial conditions are well-defined (see Bertschinger (1998) and Bagla (2005) for reviews). Therefore, they are considered to be robust and accurate. N-body simulations of large cosmological volumes are used, for example, for studying the abundance of halos, their clustering, and their formation histories (Davis et al., 1985; Efstathiou et al.,

1985; Springel et al., 2005b; Stewart et al., 2008; Klypin et al., 2010). The large-scale distribution of galaxies probed by large galaxy surveys (Colless et al., 2001; Gott et al., 2005) confirm the prediction of the Cosmic Web as seen in those simulations.

Dark matter halos have universal density and phase-space profiles (Navarro et al., 1997). In "zoom-in" cosmological simulations (Diemand et al., 2007a; Springel et al., 2008) one chooses an appropriate halo from a low resolution cosmological box and resimulates it using high resolution around the halo itself and low resolution far away from the halo. This allows detailed investigations of, e.g. halo substructure and inner profile, at the expense of a weaker statistical sampling of different halos.

1.1.3 Modeling galaxy formation

In the current paradigm, the baryonic matter at first follows the gravitational potential set by the collapse of the dark matter and shock-heats up to the virial temperature of the dark matter halo, but the physical processes that govern its subsequent evolution are far more complex. The gas then radiatively cools and falls to the central region of the dark matter halo, where it collapses into stars, thereby making galaxies (White & Rees, 1978; see Benson (2010) for a review).

In comparison to modeling the evolution of the dark matter, understanding the baryonic process of galaxy formation is much more complicated, for several reasons. First, crucial physical aspects of the problem, such as hydrodynamical processes in the multi-phase interstellar medium (ISM), star-formation, supernova feedback and black hole growth and feedback, are insufficiently understood both theoretically and observationally. Second, physical processes occurring at small scales affect galaxy formation on the largest scales, such that current available computational power is far from being enough for resolving the full dynamic range of the significant scales.

Moreover, hydrodynamical calculations are a computationally challenging task, and this is further aggravated by the fact that the parameter space required for the description of the different baryonic processes is large and not well constrained. This means that investigating that parameter space by simultaneously simulating dark matter and hydrodynamics in cosmological-sized boxes becomes prohibitively computer power-consuming. For that reason, semi-analytical models, known as SAMs, have been introduced (Kauffmann et al., 1993; Cole et al., 1994; Somerville & Primack, 1999; Croton et al., 2006; De Lucia & Blaizot, 2007; Benson & Bower, 2010; Neistein & Weinmann, 2010; see Baugh (2006) for a review). These models are built over merger trees of dark matter halos, and implement simplified recipes for baryonic processes, including for the hydrodynamics. There are indeed great successes to such models, but there are still basic observables they cannot reproduce. A different approach to galaxy formation is halo occupation distribution (HOD) models, where observed galaxy populations are matched to simulated dark matter halos or subhalos (Klypin et al., 1999; Zehavi et al., 2005; Skibba & Sheth, 2009; Hopkins et al., 2009b; Wetzel & White, 2010). These are thus not *ab initio* models, but they do allow capturing certain constraints on galaxy formation.

Nevertheless, hydrodynamical cosmological simulations are an important tool for study-

ing galaxy formation, since they model self-consistently the coupled evolution of dark matter structure formation and hydrodynamics. The two principal numerical approaches to simulating the hydrodynamics are the Lagrangian *smoothed particle hydrodynamics* method (SPH; Lucy, 1977; Gingold & Monaghan, 1977; Springel & Hernquist, 2002; Wadsley et al., 2004; Springel, 2005; see Springel (2010) for a review) and the Eulerian mesh approach, whether using a uniform grid (Stone & Norman, 1992; Cen, 1992; Ryu et al., 1993) or the *adaptive mesh refinement* technique (AMR; Berger & Olinger, 1984; Bryan & Norman, 1997; Teyssier, 2002). Baryonic processes other than hydrodynamics are usually referred to as "sub-grid" processes, and their inclusion in the calculations has to rely on simplified recipes. The two most basic sub-grid processes are radiative gas cooling and star-formation (Cen & Ostriker, 1992; Katz et al., 1992, 1996). Another key component of baryonic physics is star-formation feedback, where stars inject energy into the interstellar gas, mimicking supernova explosions (Katz et al., 1992; Navarro & White, 1993; Springel & Hernquist, 2003b; Stinson et al., 2006). Without feedback, far too much gas cools and condenses into galaxies (the "over-cooling problem"; White & Rees, 1978).

In "zoom-in" hydrodynamical simulations (Katz & White, 1993; Navarro & White, 1994; Navarro & Steinmetz, 1997; Naab et al., 2007; Brooks et al., 2007; Governato et al., 2010), different physical processes in the galaxy of interest can be resolved, while the system as a whole evolves inside a realistic halo within the full cosmological context, including mergers with other systems, continuous smooth accretion from the cosmic web, the influence of tidal forces and the angular momentum evolution of the large scale structure.

Forming disk galaxies in hydrodynamical cosmological simulations has proven hard. The standard scenario of disk formation is that as gas cools and falls from the halo onto the disk galaxy, it keeps the angular momentum that it acquired together with its dark matter halo from cosmological tidal torques (Fall & Efstathiou, 1980). Based on that assumption Mo et al. (1998) constructed a model for disk formation inside CDM halos. However, in hydrodynamical simulations the angular momentum of the gas is typically not conserved during its collapse, but is rather transferred to the dark matter. Thus, in *ab initio* simulations, the disks that form are small and with low angular momentum, in sharp disagreement with observations (Katz & Gunn, 1991; Navarro & White, 1994; Abadi et al., 2003; Joung et al., 2009). This is the so-called "angular momentum problem". It is generally agreed that feedback processes are key to solving this problem and reproducing realistic disk galaxies (Weil et al., 1998; Sommer-Larsen et al., 2003; Scannapieco et al., 2008; Governato et al., 2009; Agertz et al., 2010; Brook et al., 2010), but the details are not yet agreed upon.

1.2 High-redshift galaxies

1.2.1 Observed star-forming galaxies at $z \approx 2$

The first objects to be detected at $z \gtrsim 1$ were quasars (e.g. Carswell & Strittmatter, 1973) and radio galaxies (e.g. Spinrad & Djorgovski, 1984), both associated with emission

from supermassive black holes. In the early 1990's there were no more than a handful of detected "normal" galaxies at $z \gtrsim 1$. Since then, thousands of high-redshift galaxies have been detected and enormous progress has been made in understanding early galaxy formation (for a review, see Ellis, 2008). The current "golden era" of high-redshift galaxy formation research can be attributed to major advances in several aspects.

- The opening of new observable wavelength windows, resulting from space-borne missions, which do not suffer from atmospheric absorption and scattering, such as the *Hubble Space Telescope*, as well as from new detector capabilities, e.g. in infrared wavelengths. Only a decade ago, very little was known about galaxies in the redshift range $1.4 \lesssim z \lesssim 2.5$, coined the "redshift desert", because in this range rest-frame optical spectroscopic lines are redshifted into the infrared, while the rest-frame ultraviolet lines still remain in the observed ultraviolet regime (Steidel et al., 2004).
- The improvement of sensitivity, which resulted both from the advent of the 8-10-meter-class telescopes and the replacement of photographic plates with CCDs that have over an order of magnitude better quantum efficiency. Various fields with deep multi-wavelength exposures have been introduced, such as the Hubble Deep Fields (Williams et al., 1996; Ferguson et al., 2000).
- Increased angular resolution thanks to space-borne missions or the technology of Adaptive Optics (AO; Davies et al., 2010) that allows correction of atmospheric distortions. Galaxies at $z \approx 2$ can be resolved today with a Point Spread Function (PSF) of $\approx 0.15''$, corresponding to physical scales of ≈ 1 kpc.
- The introduction of efficient selection methods for high-redshift galaxies based on their broad-band colours. Steidel & Hamilton (1992, 1993) developed a technique for identifying star-forming galaxies at $z \gtrsim 3$ based on a spectral break at their rest-frame 912\AA Lyman limit, which has then been applied to large surveys of the so-called Lyman Break Galaxies (LBGs; Steidel et al., 1996; Giavalisco, 2002). Later on, Daddi et al. (2004) and Adelberger et al. (2004) introduced efficient colour-colour selection criteria for star-forming and passive galaxies at $1 \lesssim z \lesssim 3$ (BzK, BX, and BM galaxies).
- The advent of Integral-Field Units (IFUs; e.g. SINFONI on the VLT; Eisenhauer et al., 2003) has created the possibility to spatially resolve spectroscopic features, thereby measuring the kinematics of the ISM of high-redshift galaxies.

Galaxy populations evolve with redshift. Up to $z \approx 1$ disk galaxies do not evolve strongly in size, but they do become bluer and more star-forming with increasing redshift (Lilly et al., 1998). The number of irregular, and blue, galaxies evolves rapidly with redshift, such that the conventional Hubble classification system becomes less and less relevant (Abraham et al., 1996). The "redshift desert" is a critical epoch in which modern galaxies assemble and form. The morphologies of $z \approx 2$ galaxies are mostly either compact and barely resolved or extended and irregular, while there are almost no local spiral

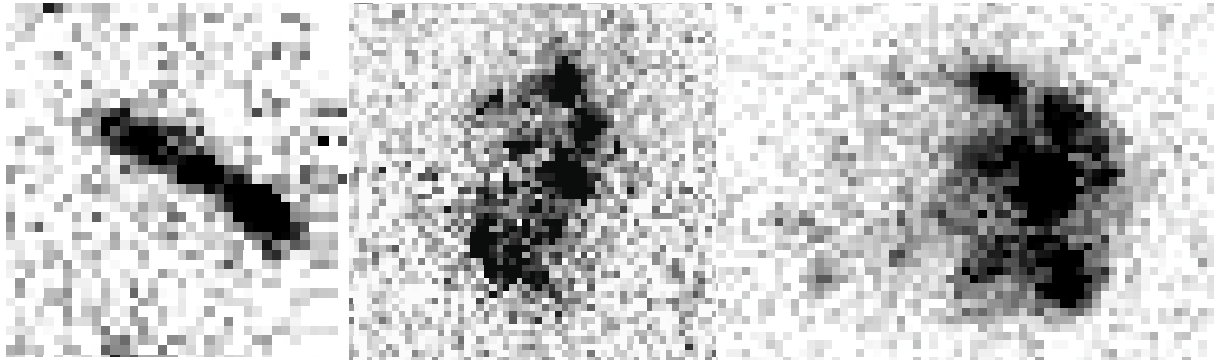


Figure 1.1: Clumpy $z \approx 2$ galaxies. *Left*: A chain galaxy, *Middle*, *Right*: clump-cluster galaxies. Adopted from Elmegreen et al. (2004).

galaxies analogues (Dickinson, 2000). The irregular morphologies have been classified as "clump clusters" and "chain galaxies" (e.g. Elmegreen et al., 2004, 2007, see Figure 1.1), and characterised quantitatively also by Conselice et al. (2008).

The cosmological epoch of $z \approx 2$ is special in that it is the time when the cosmic star-formation history peaks (Madau et al., 1996; Hopkins & Beacom, 2006). This is not only true for the whole Universe, but also individual $z \approx 2$ galaxies show high star-formation rates and high infrared luminosities. In fact, "normal" star-forming $z \approx 2$ galaxies are (Ultra) Luminous Infrared Galaxies (ULIRGs/LIRGs), and by local standards they are "starbursting". There is a rather tight correlation between stellar mass and SFR (Daddi et al., 2007; Noeske et al., 2007), which indicates that star-formation is not episodic but a rather continuous process with a high duty cycle. Moreover, the normalisation of that tight correlation evolves strongly with redshift: a galaxy of a given mass at $z \approx 2$ forms stars at a rate higher by a factor of ≈ 10 compared to a galaxy of the same mass in the local Universe.

Spectroscopy of nebular lines reveals the kinematics of the ionised ISM, which can be used to learn about the dynamical state of galaxies. Utilising slit spectroscopy, Erb et al. (2004) found large velocity gradients and high velocity dispersions in a sample of $z \approx 2$ galaxies. Observations with IFUs strengthened those early results by revealing regular velocity fields indicative of rotating disks. The largest sample of such observations is the SINS survey, that includes ≈ 100 objects, of which ≈ 15 have high resolution AO data (Genzel et al., 2006; Förster Schreiber et al., 2006, 2009).

Evidence for the existence of large gaseous rotating disks in optically/NIR-selected populations exist for a sample of > 30 $z \approx 2$ galaxies in the SINS survey. These can be distinguished using detailed dynamical modeling (Genzel et al., 2008; Cresci et al., 2009) or using kinemetry (Shapiro et al., 2008). Direct kinematical evidence for major merger events do exist for some objects in the SINS survey too. These studies concluded that a significant population at $z \approx 2$, in particular the larger and more massive star-forming galaxies, are rotationally-supported (albeit thick) disks with large gas-phase velocity disper-

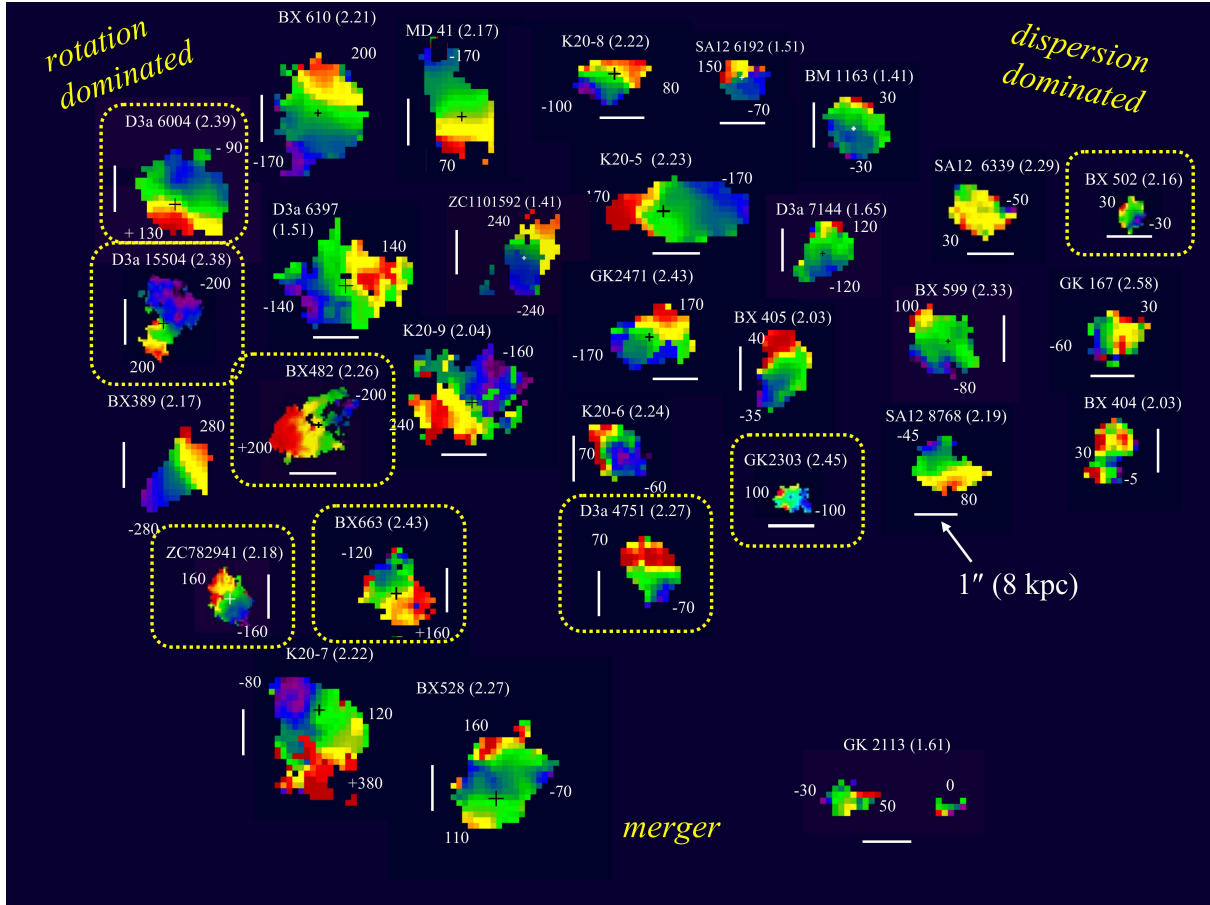


Figure 1.2: Velocity maps of SINS galaxies. *Top left*: rotation-dominated galaxies, which show large and regular rotation patterns, *Top Right*: dispersion-dominated galaxies, which show small velocity gradients, *Bottom*: merger-dominated galaxies, which show disturbed and irregular velocity patterns. Adopted from Förster Schreiber et al. (2009).

sions. A third kinematical category of galaxies in the SINS survey is dispersion-dominated galaxies (Förster Schreiber et al., 2009, see also Law et al., 2007), which show small velocity gradients v but large velocity dispersions σ such that $v/\sigma \lesssim 2$. Their nature is not yet clear. Figure 1.2 shows velocity fields of a sample taken from the SINS survey.

Even the large rotation-dominated disks differ from local disk galaxies in a number of important characteristics: they are very gas-rich (with typically comparable mass in stars and gas), very turbulent (with the ratio of the rotational velocity to the velocity dispersion being $v/\sigma \approx 2 - 8$, in contrast with $v/\sigma \approx 10 - 20$ locally) and clumpy. A fraction $\gtrsim 0.25$ of the total star-formation takes place in just a few massive ($\approx 10^8 - 10^{10} M_\odot$) large (≈ 1 kpc) clumps. When the systems are observed edge-on, the clumps seem to be very well aligned, in further support of their origin not being galaxy mergers, but rather in situ formation (Elmegreen & Elmegreen, 2005, 2006). Some galaxies have very flat mass profiles, while in

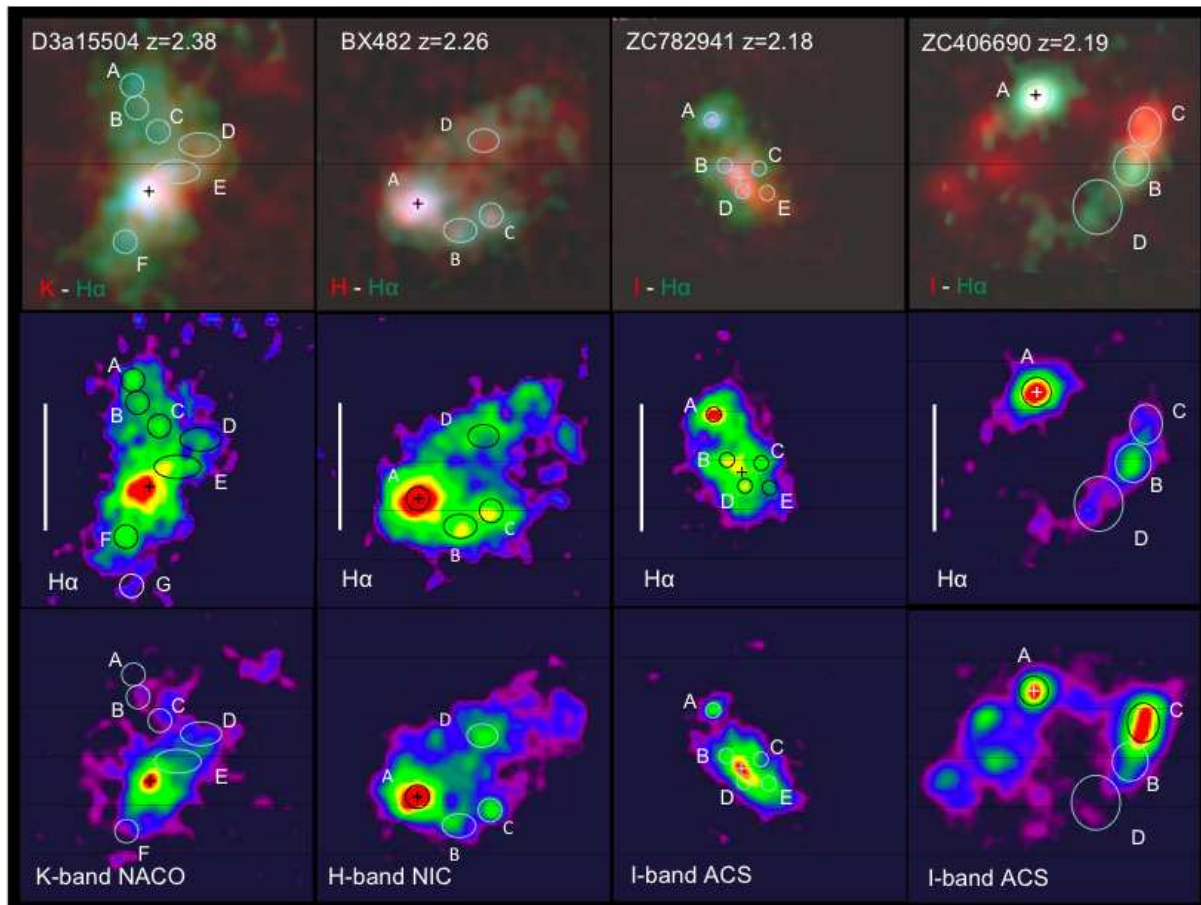


Figure 1.3: Clumpy galaxies shown in continuum (*Bottom*) and in the $H\alpha$ line (*Middle*). *Top*: false color images, demonstrating in some cases a central concentration of continuum emission, and in some cases the greatly varied $H\alpha$ -to-continuum ratio. Adopted from Genzel et al. (2010).

others there exists an indication for a central mass concentration (a "bulge") in addition to the gaseous disk component. Furthermore, there is evidence for a correlation between the age of a system and the fraction of its mass that is in a bulge-like component (Genzel et al., 2008). Figure 1.3 shows clumpy $H\alpha$ and continuum morphologies for four galaxies. It also demonstrates that the $H\alpha$ and continuum clumps are not always aligned.

1.2.2 An emerging new theoretical understanding

The rapidly emerging theoretical understanding of galaxy formation at $z \approx 2$ has several ingredients. First, high accretion rates of "fuel" for star formation, i.e. cold gas, must be delivered into galaxies over long periods, comparable to the Hubble time at $z \approx 2$, while still allowing a relatively relaxed dynamical state of a disk to exist. This is believed to

be possible thanks to the geometry of the cosmic web, from which halos are fed. In halos more massive than a threshold of $\lesssim 10^{12} M_{\odot}$ a virial shock develops that heats the gas trapped in the gravitational potential of the halo to the virial temperature $T \gtrsim 10^6 K$ (Birnboim & Dekel, 2003). This gas then has to cool down in order to be able to sink into the center of the halo where the massive galaxy resides, therefore the mass accretion rate onto the galaxy itself is much lower than that onto the halo as a whole. However, it was shown recently that narrow dense streams of gas, where the cooling time is very short, can penetrate this hot halo and supply gas to the central halo at a rate comparable to the cosmic accretion rate onto the halo (Kereš et al., 2005; Dekel et al., 2009a).

Second, the large turbulent velocities of the star-forming gas probably play a fundamental role in shaping the differences between $z \approx 2$ disk galaxies and the ones in the local Universe. The $z \approx 2$ disks are observed to be in a marginally-unstable state, with a Toomre's Q parameter around 1, which means that the gas is undergoing fragmentation into Jeans-mass clumps (Genzel et al., 2008; Dekel et al., 2009b). The large turbulent velocities make the Jeans mass and Jeans length much larger than any star-forming region in the local Universe. Thus, gravitational instability is thought to be the origin of the observed massive star-forming clumps. The mechanism creating and preserving the large turbulent velocities is still debated. It has been suggested that it is driven by the gravitational instability itself in a self-regulated way (Dekel et al., 2009b), or by the impact of the infalling gas (Genzel et al., 2008), or even by internal feedback processes from supernova explosions or young stars.

Third, a bulge-like mass concentration forms in the center of the system by coalescence of the massive clumps, as their orbits decay due to dynamical friction (Noguchi, 1999; Immeli et al., 2004b,a; Bournaud et al., 2007; Genzel et al., 2008). This scenario can explain the observed correlation between age and bulge dominance. It has been suggested that the coalescence of the clumps may dynamically resemble a 3D major merger and thus create a "classical" bulge (Elmegreen et al., 2008a). Minor mergers with infalling galaxies may also play a role in the formation of a bulge, as it is difficult to avoid them in the Λ CDM paradigm. The process of bulge formation also raises the question of black hole formation, as there is a tight correlation in the local Universe between properties of the two. An attractive possibility, although far from being demonstrated, is that intermediate-mass black holes form inside the star-forming clumps, and migrate with them to the centers of the systems (Elmegreen et al., 2008b).

1.2.3 Modeling $z \approx 2$ star-forming galaxies

In large cosmological simulations, either of dark matter only combined with a SAM, or hydrodynamical simulations, individual galaxies are poorly resolved, but implications of the large-scale cosmological structure formation can be investigated. Early numerical investigations of high-redshift galaxies were of these type, and focused on LBGs at $z \approx 3$. Those studies focused mostly on the abundance and clustering of those galaxies (Governato et al., 1998; Cen et al., 1998; Kauffmann et al., 1999; Katz et al., 1999) or on their star-formation histories (Baugh et al., 1998; Somerville et al., 2001; Weinberg et al., 2002). The general

conclusion was that LBGs represent the most massive structures at their cosmic epoch, while the role of mergers in their formation remained debated. Mo et al. (1999) used a simple disk formation model inside CDM halos to find good agreement with observed sizes, luminosities and kinematics of LBGs.

Guo & White (2009) revisited those issues, as well as the problem of identifying descendants at $z = 0$, with a modern SAM, for $z \approx 3$ LBGs and $z \approx 2$ BX galaxies, while Marchesini & van Dokkum (2007) and Lo Faro et al. (2009) showed that current SAMs do not simultaneously reproduce the observed galaxy luminosity functions at different redshifts. Tonini et al. (2010) used a SAM to investigate the colours of $z \approx 2$ galaxies. Conroy et al. (2008) combined a cosmological N-body simulation and a HOD model to study the evolution of $z \approx 2$ star-forming galaxies to $z = 1$ and $z = 0$, finding that they become partly faint red satellites and partly "typical" $\approx L^*$ galaxies. Low resolution (> 1 kpc) hydrodynamical simulations were used to study the rate and geometry of gas inflow into the central regions of massive $z \approx 2$ halos (Kereš et al., 2005; Kereš et al., 2009; Dekel et al., 2009a). Sales et al. (2009) and Sales et al. (2010) used higher-resolution cosmological simulations to investigate the rotation, sizes and morphologies of $z \approx 2$ disk galaxies.

A different approach to galaxy formation modeling is using high-resolution simulations of isolated systems. These can investigate the simulated galaxies in great detail, but their relevance to galaxies forming as part of the large-scale structure can be questioned, as they may miss critical ingredients like proper initial conditions, continuous growth and interaction with their environment. Simulations of this kind relating to $z \approx 2$ disk galaxies include the early works of Noguchi (1999) and Immeli et al. (2004a,b), who showed that massive gas disks are unstable to gravitational fragmentation, and therefore form clumps that migrate to the galaxy centers to form a bulge. Elmegreen et al. (2008a) suggested that the clumps are tightly bound and are unlikely to be disrupted by supernova feedback. Bournaud et al. (2007) showed that a disk that finally formed after this process has an exponential or double-exponential profile, while Bournaud et al. (2009) discussed the remnant thick stellar disk left behind after an unstable clumpy phase. Bournaud & Elmegreen (2009) argued that an unstable clumpy phase disallows the pre-existence of a significant bulge, and that therefore the clumpy disks cannot be merger remnants, as opposed to the claim made by Robertson & Bullock (2008).

Numerous fully cosmological "zoom-in" simulations have been used to study the formation of galaxies at $z = 0$ or the formation of the first stars and galaxies at very high redshifts, but only very few focused on $z \approx 2 - 3$ galaxies (Gnedin & Kravtsov, 2010; Saro et al., 2009). Agertz et al. (2009) and Ceverino et al. (2010) ran AMR simulations of several "zoomed-in" halos to achieve high spatial resolutions of ≈ 50 pc. They demonstrated the formation of star-forming fragmenting gas disks in a cosmological context, in qualitative agreement with the scenario described above. Since the sample is still small, it is not yet clear whether the star-formation rate and large masses and sizes of some of the observed galaxies can be reproduced with the current models. It has also not been made clear what are the prerequisites of the models in order to reproduce the observed systems, and what are the general implications of using such models on galaxy formation.

1.3 Mergers

1.3.1 The physics of mergers

Galaxy mergers are theoretically believed to play an important role in galaxy formation and evolution. First, mergers are an important mechanism by which galaxies grow their mass (Kauffmann et al., 1993; Khochfar & Silk, 2006; Guo & White, 2008; Eliche-Moral et al., 2010). Second, simulations show that mergers are able to destroy thin disks, thereby transforming disk galaxies into elliptical galaxies (Toomre & Toomre, 1972; White, 1978; Barnes, 1988; Hernquist, 1992; Bournaud et al., 2005). During mergers, gas is driven towards the galaxy centers due to tidal torques (Hernquist, 1989; Barnes & Hernquist, 1991; Hopkins et al., 2009a), a process that can feed starbursts (Mihos & Hernquist, 1996; Teysier et al., 2010) and potentially central supermassive black holes (Hopkins & Quataert, 2010). The properties of merger remnants depend on the mass ratio of the merging galaxies (Naab & Burkert, 2003; Cox et al., 2008; Lotz et al., 2010b), their gas fractions (Springel & Hernquist, 2005; Cox et al., 2006a; Lotz et al., 2010a), their structure and morphologies (Naab et al., 2006b; Johansson et al., 2009), their collision orbit and relative orientation (Robertson et al., 2006), and different feedback processes such as from star-formation and black holes (Springel et al., 2005a; Cox et al., 2006b).

Galaxy mergers of all mass ratios are frequent in a Λ CDM Universe, but a special role is reserved to major mergers, i.e. mergers of galaxies with similar masses, where a mass ratio of $4 - 3 : 1$ is usually taken as the defining value. Those are thought to play a significant role in the buildup of the red sequence by transforming blue star-forming late type galaxies to red (&dead) passive early type galaxies (Toomre, 1977; Hopkins et al., 2008a). For instance, the most intense starbursts - the rare ULIRGs (Sanders & Mirabel, 1996) - are local examples of major mergers of gas rich galaxies that demonstrate the dominant role of major mergers in assembling $10^{11} M_{\odot}$ early type galaxies (Genzel et al., 2001; Dasyra et al., 2006).

Major mergers of dark matter halos involve violent relaxation, where the rapidly changing gravitational potential transfers orbital energy and angular momentum into internal degrees of freedom, and makes the halos merge and mix within a dynamical time (Lynden-Bell, 1967). In minor mergers, the smaller halo is being stripped of most of its mass shortly after entering the larger halo due to tidal stripping and gravitational shocking (Hayashi et al., 2003; Kazantzidis et al., 2004; Choi et al., 2009). However, its core can survive as a distinct substructure (subhalo) for a long time (Moore et al., 1999; Diemand et al., 2007b; Giocoli et al., 2008), during which its orbit decays due to dynamical friction on the background halo (Taylor & Babul, 2001; Gan et al., 2010). A dynamical friction merging timescale was given by Binney & Tremaine (1987) based on the idealised case formula of Chandrasekhar (1943), but there is some uncertainty in how to directly apply such estimates. In addition, results from N-body and hydrodynamical simulations of mergers seem to differ from such simplified recipes, as well as between themselves (Boylan-Kolchin et al., 2008; Jiang et al., 2008). Finally, mixing is not perfect, and phase-space remnants of disrupted subhalos, such as tidal streams, survive for long cosmological

times (Maciejewski et al., 2010).

Galaxy mergers follow their dark matter halo mergers, but the connection between the two is not straight-forward (Wetzel & White, 2010). On one hand, galaxies - being more concentrated - are less affected by tidal stripping compared to their host subhalos, such that they may only lose orbital angular momentum until they fall to the halo center and merge with the larger central galaxy (Barnes & Hernquist, 1992). On the other hand, galaxies are affected not only by gravity but also by hydrodynamical processes. Thus, gas can be stripped off of galaxies by ram pressure (Gunn & Gott, 1972). Moreover, the baryonic merger could be very dissipative and therefore might occur on a short timescale if the galaxies reach a small separation, while a dark matter subhalo remnant may survive close passages with the host halo's center (Diemand et al., 2007b). Furthermore, smaller galaxies may be completely stripped inside the larger galaxies' halos and contribute to the buildup of intracluster light (Merritt, 1983; Purcell et al., 2007) instead of merging with the larger galaxies themselves. It should be noted that the presence of galaxies affects the dynamics of the dark matter itself (Romano-Díaz et al., 2010), complicating the comparison even further. Finally, the mass ratio of merging galaxies differs from that of their host halos, due to the strong trend of galaxy-to-halo mass ratio with halo mass, and so it is not always clear what is the most appropriate definition for the mass ratio of a merger (Stewart, 2009). For example, galaxy baryonic disks can be perturbed by interactions with dark subhalos (Chakrabarti & Blitz, 2009).

1.3.2 Merger rates

1.3.2.1 Observations

Large observational efforts are devoted to measuring the fraction of galaxies that are showing signs of merger activity. This fraction has been quantified for different masses, luminosities, and redshifts in recent years, and trends with these parameters have been sought. There are two main approaches used to tackle this problem. One principal approach is pair counting (Le Fèvre et al., 2000), which means identifying close pairs of galaxies, typically in reciprocal distances of ≈ 10 kpc. The second principal approach is identification of mergers through their morphological signatures (Conselice, 2003), such as asymmetry, tidal tails, etc., which aims at identifying mergers in their relatively late stages, when the galaxies are already partly merged.

Both methods suffer from the problem of false positives, i.e. the possibility of false identification as mergers of galaxies that have projected companions, irregular morphologies, clumpy distributions of extinction or star formation rate, etc., and on the other hand - the possibility of missing mergers due to faint companions or faint merger features. It is difficult to compare the results of different studies because a variety of identification methods and different wavebands are used. Moreover, there is the problem of cosmic variance, since the fields studied so far are small. For these reasons, different observational studies do not agree concerning the evolution of the merger fraction with redshift (e.g. Le Fèvre et al., 2000; Conselice et al., 2003; Bundy et al., 2004; Lin et al., 2004; Bell et al., 2006b). Most

studies parameterise the major merger fraction of galaxies as $\propto (1+z)^m$ and find m to have values between ≈ 0 and ≈ 6 , but also more complex forms have been put forward (e.g. Ryan et al., 2008). Also, mostly mergers at $z < 1$ have been explored, but only a few studies extend out to $z \approx 3$.

Galaxy mergers at high redshift can also be studied utilising measurements of galaxy kinematics (e.g. Cooke et al., 2010), as morphological studies alone may be biased due to the short rest-frame wavelengths probed at high redshift, or due to a secular origin of complex morphologies. In particular, Tacconi et al. (2006, 2008) and Engel et al. (2010) have shown that bright sub-mm-selected galaxies (SMGs) have larger velocity widths and are much more compact than optically-selected galaxies, hence, have lower angular momenta and higher matter densities than the UV/optically-selected populations. Thus, dissipative major mergers may be the dominant mechanism for galaxies undergoing a sub-mm phase, resulting in the formation of early spheroids, similarly to local ULIRGs.

A key point to keep in mind is that observationally, only merger fractions f_m can be obtained, but in order to transform them into merger rates R_m , which can be directly compared with theoretical models, the timescale of the observed events T_m must be introduced via the general relation $R_m = f_m/T_m$. Such timescales are uncertain and approximated very crudely (although recent progress has been made; e.g. Lotz et al., 2008b; Kitzbichler & White, 2008), and thereby are a major source of uncertainty in obtaining merger rates.

1.3.2.2 Theory

An analytical model which describes the formation of dark matter halos is the Press-Schechter model (Press & Schechter, 1974), which is based on linear growth theory and spherical collapse theory, and predicts the mass function of dark matter halos as a function of redshift. The extended Press-Schechter model (EPS; Bond et al., 1991; Bower, 1991) can in addition predict evolution probabilities for individual halos, i.e. the probability for a halo of mass M_0 at redshift z_0 to have a progenitor of mass $M_1 < M_0$ at $z_1 > z_0$, or the "conditional mass function". Therefore, it allows the construction of merger trees that describe the merging history of an ensemble of dark matter halos using Monte Carlo realisations of the probability function (e.g. Kauffmann & White, 1993; Lacey & Cole, 1993; Somerville & Kolatt, 1999). By considering ellipsoidal rather than spherical collapse, the EPS formalism can achieve better results for the unconditional and conditional mass functions (Sheth & Tormen, 2002; Li et al., 2007; Zhang et al., 2008b).

Some merging properties of dark matter halos have been considered starting from the earliest cosmological N-body simulations (Frenk et al., 1985, 1988), where it was found that the merger rate is higher at higher redshifts. Studies that focus on the merger rate of dark matter halos came only with the increased dynamic range of simulations (Governato et al., 1999; Somerville et al., 2000; Gottlöber et al., 2001; Cohn et al., 2001), while modern dark matter simulations (Stewart et al., 2008, 2009; Fakhouri & Ma, 2008, 2009; Neistein et al., 2010) allow detailed computations of merger rates in a Λ CDM Universe as a function of halo mass, redshift, merger mass ratio, and environment.

As noted in Section 1.3.1, relating galaxy mergers to dark matter halo mergers is a difficult theoretical problem. Nevertheless, several methods can be employed to theoretically predict the merger rate of galaxies. First, SAMs naturally include galaxy mergers that can be readily quantified, but these are very sensitive to the details and parameters of the models, and so the predicted merger rates differ significantly between different works (Hopkins et al., 2010b). Second, HOD models can be combined with parameterization of the dark matter halo merger rate and assumptions about merger timescales to give galaxy merger rates (Stewart et al., 2009; Hopkins et al., 2010a). Finally, the galaxy merger rate can be directly measured from cosmological hydrodynamical simulations, where galaxies form *ab initio* (Maller et al., 2006). However, since such simulations are still far from correctly reproducing the observed statistical properties of galaxies (Section 1.1.3), they cannot yet give very reliable constraints on the galaxy merger rate.

1.4 Star-formation feedback in galaxy formation

Over the past decade it has become widely recognized that galactic-scale outflows, or "superwinds", play a fundamental role in galaxy formation. On the observational side, outflows have been detected at various redshifts and from a variety of galaxy masses and classes (Martin, 1998; Heckman et al., 2000; Veilleux et al., 2005; Rupke et al., 2005; Steidel et al., 2010). Measuring their outflow rates is difficult, yet the best estimates are that mass is blown out of star-forming galaxies at rates exceeding their internal star-formation rates (i.e. high wind mass-loading factors; Martin, 1999; Pettini et al., 2000; Heckman, 2003). Wind velocities have also been measured, and found to scale with galaxy mass or star-formation rate (Martin, 2005; Weiner et al., 2009). Winds are observed to be multi-phased, comprising of cold molecular gas, warm neutral and ionized gas, as well as hot X-ray emitting gas (Heckman et al., 1990; Walter et al., 2002).

On the galaxy formation modeling side, gas flowing out of galaxies into the intergalactic medium is nowadays recognized as a key ingredient, from SAMs (Guo et al., 2010) to cosmological hydrodynamical simulations (Springel & Hernquist, 2003b; Governato et al., 2010). Vigorous outflows are considered to be responsible, for example, for the mass-metallicity relation of galaxies (Erb et al., 2006), for the metal enrichment of the intergalactic medium (Tornatore et al., 2010), and for the low "baryon conversion efficiencies" of low and medium-mass dark matter halos. The latter is related to the outstanding "missing baryons" (Fukugita et al., 1998) and "missing satellites" (Kravtsov, 2010) problems in galaxy formation - only about 3% of the baryon content of the Universe is today locked in stars, and small dark matter halos seem to be extremely inefficient in making galaxies. Efficient feedback from star-formation is believed to be a key to solving those problems (Cen & Ostriker, 2006).

However, it has not yet been theoretically established what physical processes are responsible for the superwinds. The standard scenario is that supernovae and stellar winds create over-pressured bubbles of hot gas, entraining large masses of colder gas during their "blow out" into the intergalactic medium (Heckman et al., 1993). However, hydro-

dynamical simulations aimed at reproducing superwinds do not reproduce as high mass-loading factors as revealed by observations (Mac Low & Ferrara, 1999; Dubois & Teyssier, 2008; Scannapieco & Brügggen, 2010; Shen et al., 2010). Due to the lack of detailed understanding of the physical processes involved and because of limited resolution, sub-grid prescriptions in cosmological simulations are not well constrained and the implementation of superwinds in galaxy formation models is to a large degree *ad hoc*. In addition, feedback in the form of radiation pressure from luminous sources such as young OB stars or black holes is usually neglected despite the fact that the total energy output in UV radiation from young stars, integrated over the stellar initial mass function, is comparable to that from supernovae. Recent analytic work (Murray et al., 2005; Thompson et al., 2005; Zhang & Thompson, 2010; Murray et al., 2010a) suggests that radiative pressure from UV radiation that couples to the interstellar dust and gas can generate "momentum-driven winds" and may play an important role at high-redshift. Scaling relations resulting from momentum-driven winds are consistent with observed superwind scalings, and cosmological simulations that adopted those scalings as "sub-grid" prescriptions (Oppenheimer & Davé, 2006; Finlator & Davé, 2008) had many successes.

1.5 The current work

1.5.1 Motivation

After decades of research, an accurate determination of the role of mergers in galaxy formation in a Λ CDM Universe still remains elusive. In particular, whether they play a dominant role in the evolution of various high-redshift galaxy populations, and the relative importance of mergers and smoother growth, are issues of high importance. A first, but crucial, step forward on those issues requires a better understanding of the growth modes of dark matter halos, and in particular a robust determination of their growth rates, merger rates, and the relative role mergers play in their growth.

Several major questions arise from the emerging observational picture of star-forming galaxies at $z \approx 2$. How can such high star-formation rates, which in the local Universe exist only in merging starburst galaxies, be sustained over Gyr-long periods, and what mechanism provides the fuel for such high star-formation rates? What is the physics behind the large star-forming clumps - how do they form, what is their internal structure, how long do they survive? Are the observed mass concentrations "classical" bulges formed by major mergers, or are they a result of secular evolution? What are the local descendants of those $z \approx 2$ galaxies?

In this thesis we try to make a small step towards answering these questions.

1.5.2 Thesis overview

This thesis is organised as follows. In §2 we investigate the merger rate of dark matter halos in the cosmological N-body Millennium Simulation and discuss the implications for

measurements of the galaxy merger fraction. In §3 we expand our analysis of the Millennium Simulation and apply it to several additional simulations to investigate the growth modes of dark matter halos with a very large dynamic range. We find evidence for a component of smooth accretion that contributes significantly to halo mass buildup, in addition to the merging process. In §4 we use the Millennium Simulation to quantify the growth rate of dark matter halos, and relate this growth to observations of $z \approx 2$ galaxies. We further use the simulation to follow halo formation histories throughout cosmic time, and identify the possible local descendants of star-forming $z \approx 2$ galaxies. In §5 we use hydrodynamical cosmological "zoom-in" simulations focused on individual dark matter halos to reproduce observed clumpy turbulent $z \approx 2$ star-forming galaxies. We study the effect of strong galactic superwinds on the evolution of giant star-forming clumps in the simulated galaxies, and make comparisons to observations. Finally, in §6 we summarise our findings, discuss some future prospects, and conclude.

Chapter 2

The dark matter halo merger rate

Note: This chapter has been published in Genel et al. (2009).

2.1 Abstract

We have developed a new method to extract halo merger rates from the Millennium Simulation. First, by removing superfluous mergers that are artifacts of the standard friends-of-friends (FOF) halo identification algorithm, we find a lower merger rate compared to previous work. The reductions are more significant at lower redshifts and lower halo masses, and especially for minor mergers. Our new approach results in a better agreement with predictions from the extended Press-Schechter model. Second, we find that the FOF halo finder overestimates the halo mass by up to 50% for halos that are about to merge, which leads to an additional $\approx 20\%$ overestimate of the merger rate. Therefore, we define halo masses by including only particles that are gravitationally bound to their FOF groups. We provide new best-fitting parameters for a global formula to account for these improvements. In addition, we extract the merger rate per *progenitor* halo, as well as per descendant halo. The merger rate per progenitor halo is the quantity that should be related to observed galaxy merger fractions when they are measured via pair counting. At low mass/redshift the merger rate increases moderately with mass and steeply with redshift. At high enough mass/redshift (for the rarest halos with masses a few times the "knee" of the mass function) these trends break down, and the merger rate per progenitor halo decreases with mass and increases only moderately with redshift. Defining the merger rate per progenitor halo also allows us to quantify the rate at which halos are being accreted onto larger halos, in addition to the minor and major merger rates. We provide an analytic formula that converts any given merger rate per descendant halo into a merger rate per progenitor halo. Finally, we perform a direct comparison between observed merger fractions and the fraction of halos in the Millennium Simulation that have undergone a major merger during the recent dynamical friction time, and find a fair agreement, within the large uncertainties of the observations. Our new halo merger trees are available at <http://www.mpe.mpg.de/ir/MillenniumMergerTrees/>.

2.2 Introduction

In the current paradigm for structure formation, the cold dark matter model (White & Rees, 1978; Blumenthal et al., 1984; Davis et al., 1985; Springel et al., 2006), galaxy mergers play an important role in galaxy formation and evolution. Galaxy mergers drive gas towards central starbursts (e.g. Mihos & Hernquist, 1996) and supermassive black holes (e.g. Hernquist, 1989), and transform galactic morphology (e.g. Naab & Burkert, 2003; Bournaud et al., 2005). Many parameters, like the gas fraction and morphology of the merging galaxies, as well as their relative orbits and orientations, affect the properties of the merger remnant. One of the most important factors is the mass ratio of the merging galaxies (e.g. Naab et al., 2006a). Galaxy mergers of all mass ratios are frequent in a Λ CDM Universe (e.g. Stewart et al., 2008), but special importance is given to major mergers, usually considered as those with mass ratios less than $\approx 3 : 1$. These are thought to play a significant role in the buildup of the red sequence (Toomre, 1977; Hopkins et al., 2008a) by transforming blue star-forming late type galaxies into red passive early type galaxies.

Many observational studies have been carried out in recent years to investigate the fraction of galaxies that show signs of major merger activity as a function of mass, luminosity and redshift. Observationally, only merger fractions can be obtained, and in order to transform them into merger rates, which can be directly compared with theoretical models, the time scale of the observed events must be estimated (e.g. Patton et al., 2000). Two principal approaches are used to observe galaxy merger fractions. One is pair counting (e.g. Patton et al., 1997; Le Fèvre et al., 2000; Bell et al., 2006a; Ryan et al., 2008; Lin et al., 2008), i.e. identifying galaxies separated from one another by less than typically ≈ 20 kpc. This method probes the pre-merger stage and is therefore a "progenitor galaxy" merger fraction (De Propris et al., 2007). The second approach is identification of mergers through morphological signatures such as asymmetry and tidal tails (e.g. Le Fèvre et al., 2000; Conselice et al., 2003; Lotz et al., 2008a). This method aims at identifying mergers in their relatively late stages, and is therefore a "descendant galaxy" merger fraction. For each of the principal approaches different authors use different methods, as well as different selection criteria, which create systematic effects that are not easily comparable. Moreover, the intrinsic uncertainties of each method, and the effect of cosmic variance (e.g. Conselice et al., 2008) contribute further to the large scatter between the obtained results.

De Propris et al. (2007) and Conselice (2006) have noticed that the merger fractions obtained with the two principal methods should be carefully defined, and cannot be directly compared to each other, as they are actually different quantities. Both authors proposed (different) simple conversions between the two quantities. Nevertheless, both disregarded the fact that the mass difference between the progenitors and the descendant is up to a factor of 2 (in equal-mass binary mergers). That may result in very large differences in the number densities of progenitors and of descendants. Since the measured merger *fraction* implicitly includes the information of the *number* of objects, different number densities are implicitly included in the merger rate or merger fraction per progenitor galaxy versus per

descendant galaxy. Bell et al. (2006b) and Lotz et al. (2008a) realised this, and have taken the different number densities into account when comparing merger fractions obtained with different methods. We show in this chapter that the different definitions of the merger rate, per descendant or per progenitor halo, lead to significantly different results, particularly for major mergers, high redshift mergers, and high mass mergers.

Galaxy mergers follow their dark matter halo mergers, but the connection between the two is not straightforward. When two dark matter halos merge, the orbital angular momentum is transferred into internal degrees of freedom, while the more concentrated galaxies are at first not much affected. The galaxies lose relative angular momentum due to dynamical friction, and they start merging as well when they are more tightly bound (Barnes & Hernquist, 1992). All of the baryonic physics involved in galaxy mergers makes it difficult theoretically to quantify the galaxy merger rate reliably (Hopkins et al., 2010b). Nevertheless, a first step towards quantifying the galaxy merger rate would be to understand the dark matter halo merger rate, which can be studied more robustly.

Lacey & Cole (1993) estimated the halo merger rate with the extended Press-Schechter (EPS) model (Press & Schechter, 1974; Bond et al., 1991; Bower, 1991). Neistein & Dekel (2008b) and Zhang et al. (2008a) have recently constructed EPS-based approximations that are self-consistent, and Zhang et al. (2008b) have done so for the ellipsoidal collapse model. All these models differ by factors of a few tenths up to a few. N-body simulations have only recently been used to study the halo merger rate with a large dynamical range (D’Onghia et al., 2008; Stewart et al., 2009; Fakhouri & Ma, 2008, hereafter FM08). FM08 have investigated this problem based on the large Millennium Simulation (Springel et al., 2005b). They have found that the dark matter halo merger rate has an almost universal form that can be separated into its dependencies on mass ratio, descendant mass and redshift. Nevertheless, the analysis of N-body simulations is also subject to uncertainties, in particular in identifying halos. FM08 present 3 ways to analyse the simulation, which differ from one another by $\approx 25\%$, and by a more significant amount compared to the Lacey & Cole (1993) analytical approximation. All of these investigations have quantified the halo merger rate per *descendant* halo. Recent work has also used N-body simulations to study mergers of subhalos (Angulo et al., 2009; Wetzel et al., 2009).

In this chapter we extract the dark matter halo merger rate from the Millennium Simulation using a new method for identifying halos and mergers, as well as a new definition of the merger rate. In §2.3.1 we review the Millennium Simulation and its post-processing. In §2.3.2 we describe how we create merger trees that are free of artificial effects not considered previously. In §2.3.3 we define the merger rate per descendant halo, as well as the merger rate per progenitor halo, which is related to observed galaxy merger fractions when they are measured via pair counting. In §2.4 we describe our results and in §2.5 we compare them to previous work. In §2.6 we calculate the halo merger fraction in the Millennium Simulation and compare to observations. In §2.7 we discuss our results and their relevance to observations, and summarise.

2.3 Extracting the merger rate from the Millennium Simulation

2.3.1 The Millennium Simulation and its merger trees

The Millennium Simulation is a cosmological N-body simulation following 2160^3 dark matter particles, each of mass $8.6 \times 10^8 h^{-1} M_\odot$, in a box of $500h^{-1}$ Mpc on a side, with 64 generated output times (“snapshots”) from $z = 127$ to $z = 0$. The cosmology is set to Λ CDM with $\Omega_m = 0.25$, $\Omega_\Lambda = 0.75$, $\Omega_b = 0.045$, $h = 0.73$, $n = 1$ and $\sigma_8 = 0.9$, which we will adopt throughout this chapter.

In the Millennium Simulation there are two levels of structure identification. First, the friends-of-friends (FOF) algorithm (Davis et al., 1985; with a linking length $b = 0.2$ of the mean particle separation) creates a catalogue of FOF groups in every snapshot. In the limit of a large number of particles, FOF groups enclose the particles within isodensity contours of $\approx b^{-3}$ times the mean matter density (Frenk et al., 1988; Lacey & Cole, 1994; Jenkins et al., 2001), and their mean densities correspond approximately to the overdensities of virialised halos expected from the spherical collapse model (Lacey & Cole, 1994). Thus, FOF groups are considered to represent dark matter halos. However, substructure as traced by local density maxima are not distinguishable within the FOF groups. For this purpose, the algorithm SUBFIND (Springel et al., 2001) identifies substructures in each FOF group, by finding gravitationally self-bound groups of particles around maxima in their smoothed density field. Thus, each FOF group contains at least one subhalo, and the subhalo with the “most massive history” is chosen to be the *main* subhalo (De Lucia & Blaizot, 2007).

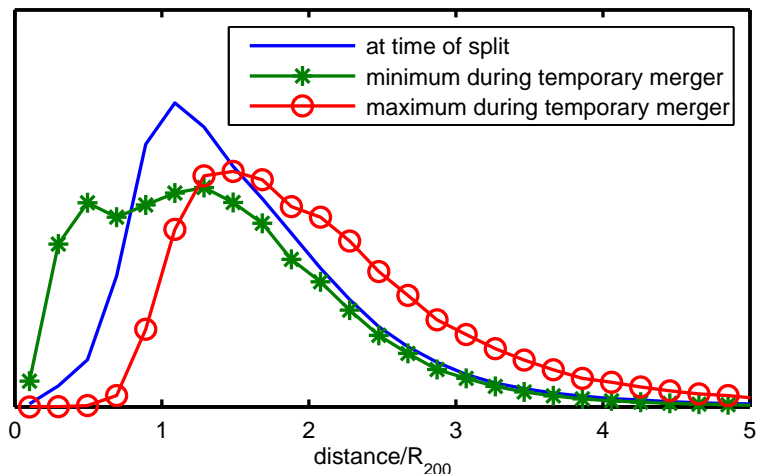
The Millennium merger trees¹ are constructed from the subhalos by finding a single descendant for each subhalo at the following snapshot. The FOF groups themselves play no role in constructing the merger trees. Nevertheless, if the halo merger rate is to be studied, then new merger trees, in which each node is a halo rather than a subhalo, must be built.

2.3.2 Constructing new halo merger trees

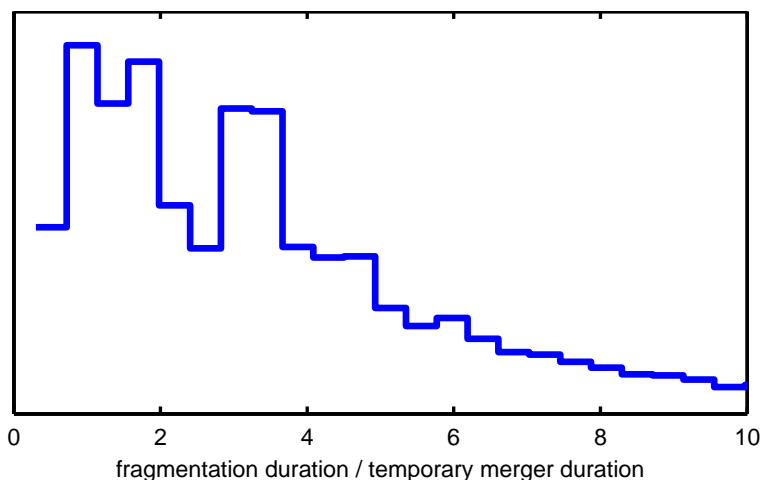
We build new halo-based, that is FOF group-based, merger trees by defining one descendant for each FOF group. The main subhalo in each FOF group is identified and followed to its subhalo descendant using the original subhalo trees. Then, the FOF group to which that subhalo descendant belongs is defined as the FOF group descendant of the FOF group in question.

In practice, FOF groups not only merge, but may also split. This is not compatible with the simplified notion of hierarchical build-up and indeed not described at all by an analytical model such as EPS. Yet, this phenomenon is robust in numerical N-body

¹Structure catalogues and the derived merger trees have been made public by the Virgo Consortium: <http://www.mpa-garching.mpg.de/millennium>.



(a)



(b)

Figure 2.1: *Top*: The distribution of relative distances (with respect to R_{200} at each snapshot) between subhalos that only temporarily belong to the same FOF group. The solid blue curve shows the distribution at the last snapshot of the temporary merger, the green curve with asterisks shows the minimum relative distances during the temporary merger, and in red with circles is the distribution of maximum distances. These distributions are shifted slightly towards lower (higher) values at lower (higher) redshifts and for more minor (major) mergers. *Bottom*: The distribution of the ratio between the fragmentation duration (the time between the fragmentation itself and the subsequent re-merger) and the first, temporary, merger that precedes the fragmentation, for cases where the fragmentation lasts more than three snapshots. The fragmentation duration is typically much longer (mean ≈ 4 , median ≈ 3) than the temporary merger duration, indicating that the temporary merger is usually only an artifact of the FOF algorithm.

first merger duration in snapshots	∞	≤ 3	≤ 3	≤ 3	> 3	> 3	> 3
fragmentation duration in snapshots	-	≤ 3	> 3	∞	≤ 3	> 3	∞
abundance	78%	7.6%	4.4%	3.5%	2.5%	1.9%	2.1%
snipping	1	2	2	1	2	2	1
stitching-3	1	1	2	1	1	2	1
stitching- ∞	1	1	1	1	1	1	1
splitting-3	1	1	1	0	2	2	1
splitting	1	1	1	0	1	1	0

Table 2.1: Merger scenarios, their abundance, and the different counting by different algorithms. In bold font are scenarios for which a certain algorithm over-counts the number of mergers. For details see §2.3.2. A merger duration of ∞ snapshots denotes a merger with no fragmentation, and a fragmentation duration of ∞ snapshots means that the fragments never re-merge by $z = 0$. The abundances of the different scenarios are calculated using all the mergers in the Millennium Simulation.

simulations. A FOF group is described as “split” when a *subhalo* belonging to it at a given snapshot is no longer part of it at a later snapshot.

Those subhalos that were split out of their FOF groups can be classified according to several criteria, describing their past and future histories: where they were created, what structure they belong to right after the split, and where they end up at later times. Almost all subhalos are not *formed* inside their host FOF groups, but originate from previous mergers in which they were accreted onto them. Thus, most split subhalos are part of mergers that started in the past but were cut by the split, before the subhalos merged. The location of the split subhalo in the immediate snapshot after the split can be either as an independent FOF group or as a subhalo in another FOF group. After the split, the split subhalo may re-merge with the FOF group from which it was split, or it may not do so at all.

A very typical case is that of two FOF groups that merge, with one becoming a subhalo of the other, which then later split again into two distinct FOF groups. If they never re-merge, it is clear that a “merger” interpretation of such an event would not be appropriate. Most likely, a temporary bridge of particles caused the FOF algorithm to identify them as one FOF group (White, 2001; Lukić et al., 2009). If they eventually do re-merge after a few snapshots, the first merging and splitting merely shows that they were relatively close and that some interaction took place. However, the actual point of merging should correspond to the merger event after which there is no more splitting. To support that interpretation, we show in Figure 2.1(a) that in 65% (85%) of temporary mergers the distance between the subhalos never decreases below R_{200} ($R_{200}/2$) of the joint FOF group. The undesired implications of the way splits appear in the original merger trees are artificial changes in the halo mass function and merger counts. As shown by FM08 and as will be shown later on in this chapter, different algorithms that deal with this phenomenon change the halo

mass function only slightly, but have a pronounced effect on the merger rate.

It is common not to treat such fragmentation cases in any special way, thereby allowing the split fragments to have no progenitors (e.g. FM08’s ”snipping” method). In that case, the split fragment may re-merge (even several times) with the same halo. One approach of dealing with this issue (e.g. Helly et al., 2003; Harker et al., 2006) is via different algorithms for splitting FOF groups that are artificial combinations of several halos. Another approach was taken by FM08, who chose in their fiducial ”stitching-3” method to merge back the split fragments when a future merger takes place within three subsequent snapshots after the fragmentation. They also presented a method, ”stitching- ∞ ”, where subhalos are never allowed to split out of their FOF groups. In the present chapter we eliminate the occurrence of halo fragmentation in our new trees, in a way similar to Helly et al. (2003). We do so by identifying any FOF group at redshift z_p that contains at least a pair of subhalos that at some lower redshift $z_f < z_p$ do not belong to the same FOF group. Such a FOF group is split by our algorithm into several fragments in the following way. Subhalos which belong to different FOF groups at z_f will belong to different fragments at z_p as well, while subhalos that do stay together at z_f will not be separated at z_p . Any new fragment our algorithm creates, as well as any untouched FOF group, is considered hereafter simply as a ”halo”. Fakhouri & Ma (2009) (hereafter FM09) have suggested a variant of this algorithm, ”splitting-3”, that splits the progenitors of fragmenting FOF groups only 3 snapshots backwards.

We identify two possible advantages of our ”splitting” method over ”snipping”, ”stitching” and ”splitting-3” algorithms. The first has to do with double counting of mergers. Table 2.1 presents the possible scenarios for binary merging and fragmentation events, and the number of mergers that each of the methods presented above counts for those scenarios. Printed in a bold font are cases where a method counts more mergers than appropriate. Only our ”splitting” method never counts artificial mergers as real ones. Moreover, all other methods except from ”stitching- ∞ ” leave spurious fragmentations in the tree, which may be mistakenly interpreted as extremely high (positive and negative) ”smooth” changes in the halo mass, not associated with any merger. We note, however, that any algorithm that does not double-count mergers, e.g. a combination of ”stitching-3” for short fragmentations and ”splitting” for long fragmentations, is valid from this perspective.

The second advantage relates to the timing of the merger, and makes us always prefer ”splitting” over a combination of ”splitting” and ”stitching”. In cases described by the second column of Table 2.1, where both the first, temporary, merger and the fragmentation duration are shorter than three snapshots and comparable to each other, there’s no significant difference between ”stitching” and ”splitting”. In such cases it is difficult to determine conclusively what the ”correct” time is, i.e. that of the first or the second merger (but note that Figure 2.1(a), as mentioned earlier, suggests that the later merger is usually the more physical choice). Nevertheless, when the time spent between the fragmentation and the re-merging is larger than 3 snapshots, the different algorithms perform very differently: ”stitching- ∞ ” counts it at the time of the first merger, while our method counts it at the time of the re-merger. As Figure 2.1(b) shows, in those cases when the fragmentation phase lasts more than three snapshots, it is mostly a few times longer than

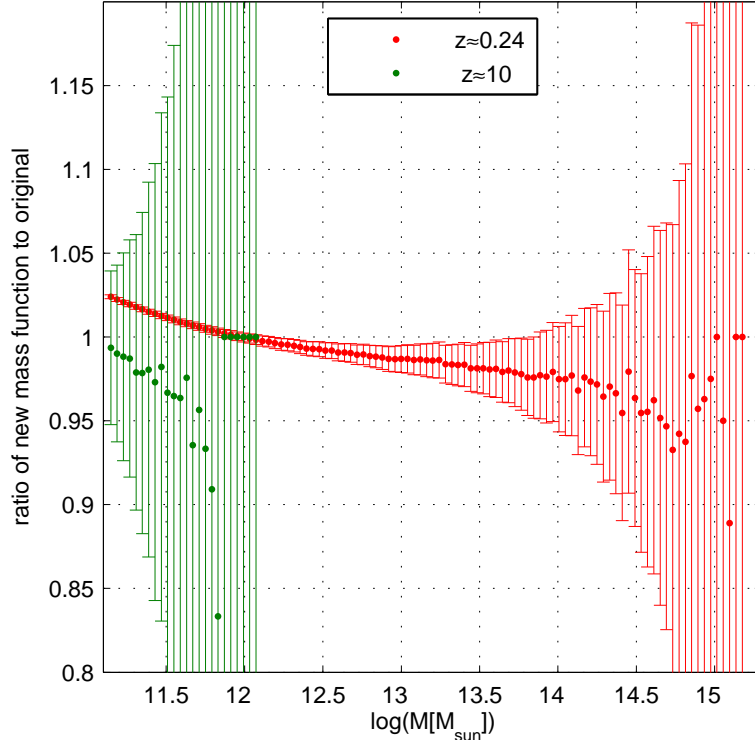


Figure 2.2: The ratio between the halo mass function after applying our splitting algorithm and the original mass function. The difference does not exceed $\approx 15\%$, and where it is statistically significant (according to Poisson errors, which are shown by the error bars) it does not exceed $\approx 3\%$, for $M > 1.5 \times 10^{11} M_{\odot}$ at all redshifts.

the first, temporary, merger. This further suggests that the point of re-merging should be usually considered as the more physically appropriate time of merging.

Our splitting algorithm changes the halo mass function $n(> M, z)$ only slightly. In our new halo catalogues there are naturally fewer massive halos and more small halos, compared to the original FOF group catalogues. Figure 2.2 shows that the change does not exceed $\approx 15\%$, while where the change is statistically significant (according to Poisson errors) it does not exceed $\approx 3\%$, for $M > 1.5 \times 10^{11} M_{\odot}$ at all redshifts. This difference is smaller than the uncertainty due to e.g. different identification methods for halos or different simulation codes (e.g. Lukić et al., 2007; Heitmann et al., 2008).

Our method implicitly assumes that no splits occur after $z = 0$, which is of course physically wrong but technically unavoidable, since the simulation terminates at $z = 0$. The typical time it takes the subhalos to disappear after having merged with bigger FOF groups is comparable to the cosmic lookback time at $z \approx 0.1$. Therefore, starting from $z \approx 0.2$, it becomes impossible to identify a non negligible fraction of the artificially linked FOF groups - those that would have split after $z = 0$ had the simulation continued running. In particular, FOF groups at the last snapshot of the simulation are never split

by our splitting algorithm, since it is impossible to know which subhalos of theirs would split “in the future”. Our results are therefore valid only for $z \gtrsim 0.2$, and for use at lower redshifts an extrapolation should be used.

We define the mass of a halo as the mass of all the particles gravitationally bound to it, i.e. the sum of its subhalos’ masses. For $\approx 80\%$ ($\approx 95\%$) of the halos, the unbound particles, which we don’t take into account, are less than 5% (20%) of the total FOF mass. Also, the halo mass function $n(> M, z)$ changes by just a few percent if also the unbound particles are included. Nevertheless, including the unbound particles (as in e.g. FM08) has a significant effect on the inferred merger rate. In §2.5.3 we describe this difference, explain its source and justify our choice of not including the unbound particles in the mass of halos.

2.3.3 Definitions of the merger rate: per progenitor halo and per descendant halo

We identify a merger whenever two or more halos at snapshot s have a common descendant at snapshot $s + 1$, and use the time/redshift difference between the two snapshots to define the merger rate per unit time/redshift, respectively. We define a merger as a two-body event, in a way that if $n > 2$ halos merge, then $n - 1$ mergers are recorded, each between the most massive one and one of the others. The possibility that the mergers occur in a different order, i.e. that some of the smaller progenitors merge with one another before merging together with the most massive progenitor, is sufficiently small so that our results are not strongly affected by it, as shown by FM08.

We derive the merger rate per *progenitor* halo per unit time (or redshift) per mass ratio x : $\frac{1}{N_{\text{prog-halo}}} \frac{dN_{\text{merger}}}{dt dx}(x, z, M)$. Our book-keeping is performed as follows. For a merger between two halos of masses M_1 and M_2 we record one merger at mass M_1 with ratio $x = M_1/M_2$ and one merger at mass M_2 with ratio $x = M_2/M_1$. In this way, all the mergers of each halo with any other halo, less or more massive, are recorded. There is no double counting in this method, since we are interested in the merger rate *per halo* rather than the absolute number of mergers. We attribute a merger to each halo in the pair, and each merger event is counted as $2/2 = 1$ merger per halo.

In comparison, for the merger rate per *descendant* halo, only one merger is recorded at mass $M_1 + M_2$ with ratio $x = M_1/M_2$ (where the indices are defined so that $M_1 \geq M_2$). To better understand the difference, let us consider equal-mass mergers ($x = 1$). The merger rate derived by using the descendant halo would be one $x = 1$ merger per halo at $2M$, while according to our progenitor method it would be one $x = 1$ merger per halo at M . Therefore, the typical time scale for a halo of mass M to encounter another halo of mass M is the reciprocal of the merger rate *per progenitor halo* at mass M and $x = 1$. The merger rate per descendant halo at mass M can be quantitatively very different (§2.4.4) and has a different physical meaning. The merger rate per descendant halo gives the time scale on which the population of halos of mass M is *created* by equal-mass mergers. It is important to keep in mind the physical meaning of each of the definitions when implementing them

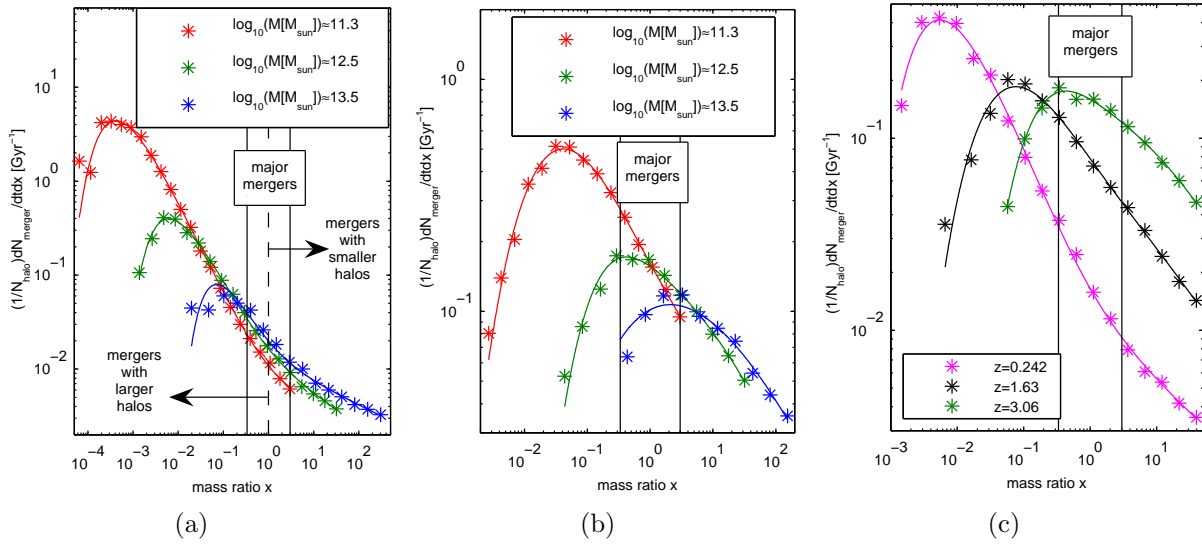


Figure 2.3: The merger rate $\frac{1}{N_{\text{prog-halo}}} \frac{dN_{\text{merger}}}{dt dx}(x, z, M)$ as a function of mass ratio x . Panel (a) displays the rates for several progenitor masses, at fixed redshift $z \approx 0.24$, and Panel (b) shows the same for $z \approx 3$. Panel (c) displays the rates at different redshifts, for $10^{12} M_{\odot} < M < 2 \times 10^{12} M_{\odot}$ halos. Asterisks show data based on the simulation, and the solid curves show our fit based on equation (2.1) and Table 2.2. To guide the eye, two vertical lines show the range of x within which we define *major* mergers. We note that x is limited at large values by the mass resolution limit of the simulation: we show only mergers between M and $M/x > 2 \times M_{\text{min}} = 4.72 \times 10^{10} M_{\odot}$. At small values x is limited by the simulation box size. The bins in x are logarithmically equally-spaced, except for at the left-most side of each curve, where bins were constructed so that they contain no less than 5 mergers.

to physical problems. For example, as we will discuss in §2.7, the appropriate quantity to use when considering merger fractions derived via pair counting is the merger rate per progenitor halo.

In the binary merger approximation, which we find to be a good one, both definitions of the merger rate are interchangeable, given that the halo mass function is known (Appendix A). Nevertheless, the merger rate per progenitor halo quantifies also the rate at which halos merge with *more massive* halos, i.e. the range $x < 1$, in addition to $x > 1$. This is important because the merger rate per descendant halo is given only for the range $x > 1$, which represents the rate at which halos of mass M_1 merge with (or accrete) less massive halos of mass M_1/x . However, the range $x < 1$ represents the rate at which halos of mass M_1 merge with (or are accreted onto) more massive halos of mass M_1/x . To illustrate the importance of this difference, consider the way a major merger between halos of masses M_1 and $M_2 = M_1/2$ is recorded. When using the descendant halo, one merger with $x = 2$ is recorded at mass $3/2M_1 = 3M_2$, while the fact that the halo with M_2 experienced a major merger is not *explicitly* accounted for. In contrast, when using the progenitor halos, two mergers are recorded: one with $x = 2$ at mass M_1 and one with $x = 1/2$ at mass M_2 .

2.4 Results

2.4.1 The merger rate per progenitor halo as a function of mass ratio

Figure 2.3 shows the merger rate $\frac{1}{N_{\text{prog-halo}}} \frac{dN_{\text{merger}}}{dtdx}(x, z, M)$ as a function of mass ratio x , for a constant redshift at different mass bins (Figure 2.3(a) and Figure 2.3(b)), as well as for a constant mass bin at different redshifts (Figure 2.3(c)). In all curves, the relation is close to a power law at large x . As x decreases, the slope becomes steeper in most curves. At further lower x , in all curves, there is a flattening and the sign of the slope changes rapidly as the function starts decreasing towards very small x . We fit this shape with the following fitting function:

$$\frac{1}{N_{\text{prog-halo}}} \frac{dN_{\text{merger}}}{dtdx}(x, z, M) = Ax^b(1 + 1/x)^c \exp(-(xM_c/M)^d) \text{Gyr}^{-1}, \quad (2.1)$$

with $A = A(z, M)$, $b = b(z, M)$, $c = c(z, M)$, $d = d(z, M)$ and $M_c = M_c(z)$.

The x^b term describes the shape of the curves for $x \gg 1$, the $(1 + 1/x)^c$ term increases the slope at $x \lesssim 1$, and the exponential term causes the cut-off at small x , depending on the mass of the halos in question and the parameter M_c . We interpret the exponential cut-off as a consequence of the exponential cut-off in the mass function: at $M/x \ll M_c$ this term's contribution is negligible, while at $M/x \gtrsim M_c$ the function decreases exponentially because there is an exponentially small number of halos of mass M_c for halos of mass M to merge with. Indeed, there is a close relationship between M_c and the dark matter halo mass at the knee of the halo mass function M_* (based on EPS; Mo & White, 2002),

Panel	Low mass [M_\odot]	High mass [M_\odot]	z	A	b	c	d	M_c [$10^{10} M_\odot$]
a	$10^{11.25}$	$10^{11.35}$	0.24	0.006	-0.18	0.82	-0.79	32290
a	$10^{12.3}$	$10^{12.7}$	0.24	0.011	-0.32	0.57	-0.89	32290
a	$10^{13.3}$	$10^{13.7}$	0.24	0.012	-0.23	0.78	-1.12	32290
b	$10^{11.25}$	$10^{11.35}$	3.06	0.32	-0.57	0.62	-0.35	13.4
b	$10^{12.3}$	$10^{12.7}$	3.06	1.2	-0.71	1.14	-0.38	13.4
b	10^{13}	10^{14}	3.06	2.23	-0.67	0 ¹	-0.26	13.4
c	$10^{12.4}$	$10^{12.6}$	0.24	0.011	-0.32	0.62	-0.73	32290
c	$10^{12.4}$	$10^{12.6}$	1.63	0.1	-0.51	0.53	-0.48	698
c	$10^{12.4}$	$10^{12.6}$	3.06	1.409	-0.74	1.37	-0.39	13.4

Table 2.2: Fits for the merger rate as a function of mass ratio in Figure 2.3. (1) For such high mass at high redshift, the exponential cut-off affects the merger rate at x large enough that the upturn provided by the $(1+1/x)^c$ term is absent. The lowest χ^2 is actually achieved in this case with $c < 0$, but we do not allow that, hence $c = 0$ is forced.

with $M_c \approx 30M_*$. At high redshift, the exponential cut-off affects the function already at $x \lesssim 1$, so the parameters c , d and M_c become somewhat degenerate. Therefore, we make use of the relationship between M_c and M_* to reduce the freedom of the fitting by setting $\log_{10}(M_c[M_\odot]) \approx 14.8 - 1.2z$. Table 2.2 shows the best-fitting numerical values for the parameters of the fitting function, for the curves that appear in Figure 2.3.

To investigate the sensitivity of our results to the time resolution of the snapshots in the simulation, we have performed the following test. For any progenitor snapshot s , we have extracted the merger rate skipping the two subsequent snapshots, as though the next available snapshot was only $s + 3$. At low redshift we find a negligible change in the results. At increasing redshift, Δz increases, so when 2 snapshots are skipped, there occurs a non-negligible effect of averaging the redshift dependence of the merger rate. This is why at $z \approx 3$ a decrease of up to $\approx 20\%$ can be seen for this "skip 2" method, a difference that is consistent with being just the result of averaging the redshift dependence. This Δz -convergence is comparable to the one found by FM08.

As can be seen in Figure 2.3 and Table 2.2, the shape of $\frac{1}{N_{\text{prog-halo}}} \frac{dN_{\text{merger}}}{dt dx}(x, z, M)$ changes with mass and redshift, so that no global values for the fitting parameters A , b , c & d can be obtained. This reflects deviation from self similarity, in the sense that halos of different masses and at different redshifts have different weights for merging with halos of different mass ratios. At a given redshift (Figure 2.3(a) and Figure 2.3(b)), more massive halos have slightly more minor mergers ($x \gtrsim 1$, consistently with FM08) while they are being accreted onto larger halos ($x \ll 1$) at a much lower rate than less massive halos. Similarly, for a given halo mass (Figure 2.3(c)), at high redshift the minor merger rate (per unit time) is higher, while the rate of being accreted onto bigger halos is lower.

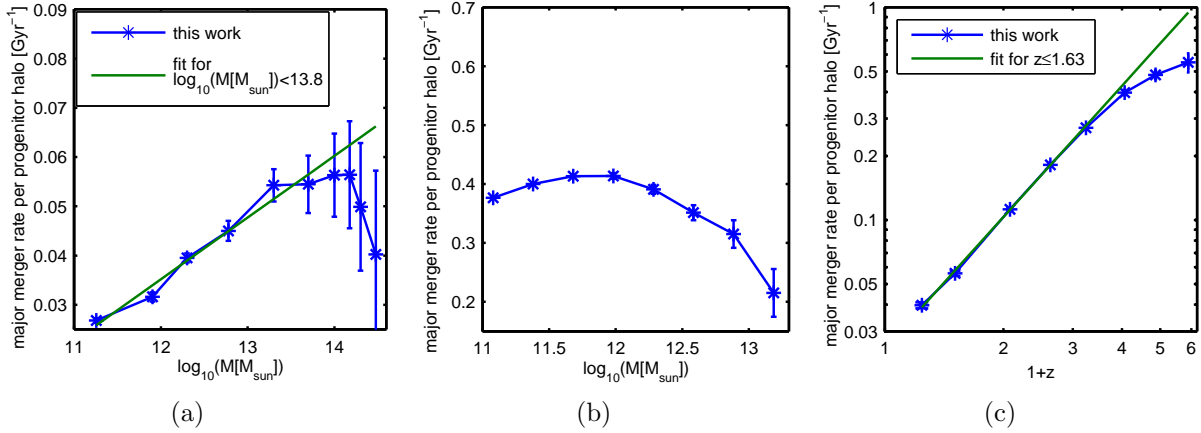


Figure 2.4: The major merger rate per progenitor halo as a function of mass at $z \approx 0.24$ (a) and at $z \approx 3$ (b), and as a function of redshift for $10^{12.4} M_{\odot} < M < 10^{12.6} M_{\odot}$ (c). The asterisks show our analysis of the simulation, while the solid green curves show the fitting function equation (2.5). The fitting functions fit the data well for low enough values of mass and redshift so that equation (2.4) holds. In this regime the major merger rate per unit time increases steeply with increasing redshift and mildly with increasing mass. Above the threshold set by equation (2.4), we find the mass/redshift dependencies to break. Specifically, at high redshift (b) the whole mass range available from the simulation is above the exponential cut-off mass given by equation (2.4), therefore the major merger rate is seen to almost always *decrease* with increasing mass. Equation (2.5) is not valid in that regime.

2.4.2 The major merger rate per progenitor halo as a function of mass and redshift

For a quantitative comparison between similar masses at different redshifts or different masses at fixed redshifts, a specific value or range in x must be chosen. We investigate the dependence on mass and redshift of the possibly most interesting range: $1/3 < x < 3$, i.e. the major merger rate:

$$\frac{1}{N_{\text{prog-halo}}} \frac{dN_{\text{major-merger}}}{dt}(z, M) = \int_{1/3}^3 \frac{1}{N_{\text{prog-halo}}} \frac{dN_{\text{merger}}}{dt dx}(x, z, M) dx. \quad (2.2)$$

Note that, following the discussion in §2.3.3, in cases where integrating over the range $1/3 < x < 3$ counts the same merger twice, also both halos are counted in $N_{\text{prog-halo}}$. In other words, each merger always contributes exactly one count to the merger rate *per halo*, so there is no double counting in equation (2.2).

Figure 2.4(a) shows the dependence of $\frac{1}{N_{\text{prog-halo}}} \frac{dN_{\text{major-merger}}}{dt}(z, M)$ on mass at $z \approx 0.24$. At $M \lesssim 10^{13.8} M_{\odot}$ the major merger rate increases with increasing mass, and a relation of

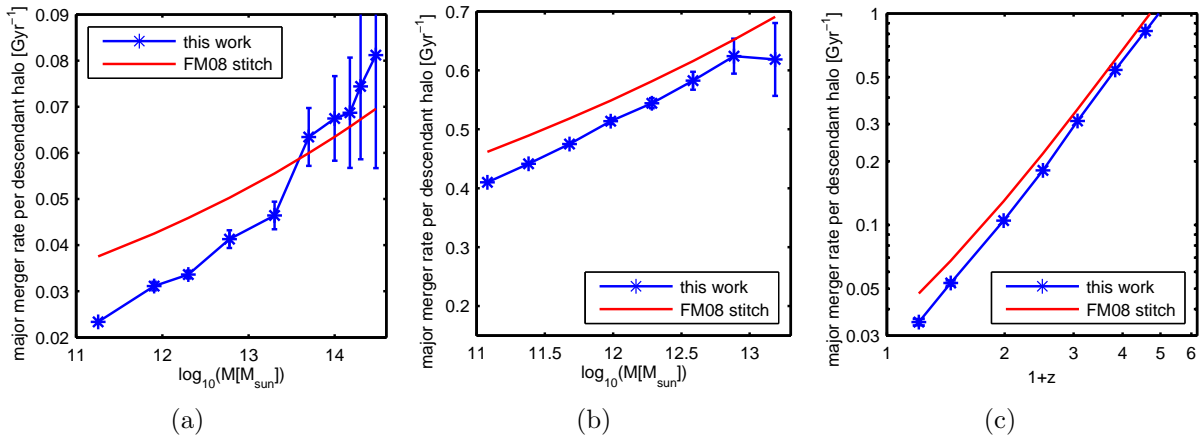


Figure 2.5: The major merger rate per descendant halo as a function of mass at $z \approx 0.24$ (a) and at $z \approx 3$ (b), and as a function of redshift for $10^{12.4} M_{\odot} < M < 10^{12.6} M_{\odot}$ (c). The asterisks show our analysis of the simulation and the red curves show the merger rate as quantified by FM08’s fitting formula (and integrated over the major merger range of mass ratios, between $x = 1$ and $x = 3$). A comparison to Figure 2.4 shows that even above the threshold set by equation (2.4) the mass/redshift dependencies of the merger rate per descendant halo do not change, in contrast with the merger rate per progenitor halo. A comparison to FM08’s results shows that the major merger rate is lower once our splitting algorithm and our mass definition are used.

the form

$$\frac{1}{N_{\text{prog-halo}}} \frac{dN_{\text{major-merger}}}{dt}(z, M) \propto \log(M) + \alpha \quad (2.3)$$

holds, as the solid green line in Figure 2.4(a) shows. However, for higher masses the major merger rate *decreases* with increasing mass, because the exponential cut-off of $\frac{1}{N_{\text{prog-halo}}} \frac{dN_{\text{merger}}}{dt}(x)$ at small x affects even the range $x > 1/3$. At each redshift the critical mass above which equation (2.3) no longer holds is different. At high redshift there are less massive halos, so the exponential cut-off occurs at $x = 1/3$ already for lower masses, compared with low redshift. We find that equation (2.3) is valid for

$$M \lesssim M_c(z)/5 \approx 6M_*(z) \approx 10^{14.1-1.2z} M_\odot. \quad (2.4)$$

Similarly, for a given mass M , at low enough redshifts the major merger rate increases with increasing redshift, as shown in Figure 2.4(c). The relation is of the form $\frac{1}{N_{\text{prog-halo}}} \frac{dN_{\text{major-merger}}}{dt}(z, M) \propto (1+z)^\beta$ with $\beta \approx 2$. But since $M_*(z)$ decreases with increasing redshift, there is a redshift above which $M > 6M_*(z)$. At that redshift the major merger rate begins to be affected by the exponential cut-off, and the power law approximation breaks down. The major merger rate starts *decreasing* with increasing redshift only at much higher redshifts (e.g. while $6M_*(z \approx 0.9) = 10^{13} M_\odot$, the major merger rate of $10^{13} M_\odot$ halos starts decreasing with increasing redshift only at $z \gtrsim 3$). We note that the regime that is affected by the cut-off exists for the merger rate per progenitor halo that we present in this Section. It does not appear in the merger rate per descendant halo, as will be shown in §2.4.3 and §2.4.4.

As long as equation (2.4) holds, we find the following fitting function for the major merger rate as a function of mass and redshift:

$$\frac{1}{N_{\text{prog-halo}}} \frac{dN_{\text{major-merger}}}{dt}(z, M) = R(\mu_{10} + \alpha)(1+z)^\beta, \quad (2.5)$$

with $R = 0.0075 \text{ Gyr}^{-1}$, $\alpha = 1 \pm 0.1$, $\beta = 2.1 \pm 0.1$ and $\mu_{10} \equiv \log_{10}(\frac{M}{10^{10} M_\odot})$. It is accurate to within $\approx 10\%$, an inaccuracy that is included in the errors quoted for the fitting parameters. Because of the inability to properly split halos in the very last snapshots of the simulation at $z \lesssim 0.2$ (as explained in §2.3.2) we do not include this range in our fitting.

An illustration of the regime where equation (2.4) does not hold is shown in Figure 2.3(b) and Figure 2.4(b). Since $M_c(z = 3) \lesssim 10^{11.5} M_\odot$, all the mass ranges we can probe at this redshift are in the regime where equation (2.4) doesn't hold. In Figure 2.3(b) it is shown that at $z \approx 3$ the exponential cut-off occurs at much larger x (compared with Figure 2.3(a)), so that also the major and minor merger regimes are affected. This means that the merger rate is *lower* for *more* massive halos even at $x > 1$, as opposed to low redshift, where this is true only for $x \lesssim 0.1$. The major merger rate, explicitly as a function of mass, is shown in Figure 2.4(b).

It is interesting to note that the major merger rate per unit redshift,

$$\frac{1}{N_{\text{prog-halo}}} \frac{dN_{\text{major-merger}}}{dz}(z, M) = \frac{dt}{dz} \frac{1}{N_{\text{prog-halo}}} \frac{dN_{\text{major-merger}}}{dt}(z, M), \quad (2.6)$$

is approximately constant with redshift for the range that is not affected by the exponential cut-off, since $\frac{dt}{dz}(z)$ approximately cancels out the redshift dependence in equation (2.5). At redshifts higher than the break redshift, the major merger rate per unit redshift decreases steeply with increasing redshift. The bimodal fit:

$$\begin{aligned} 0.38 \pm 0.02, z \lesssim 2.5, \\ 0.38 - 0.063(z - 2.5), z \gtrsim 2.5 \end{aligned} \quad (2.7)$$

describes the major merger rate per unit redshift for $10^{12} M_{\odot}$ halos as a function of redshift. It can be applied for different masses using equation (2.5) to scale with mass, and equation (2.4) to find the ‘‘break’’ redshift.

If the mass dependence of the major merger rate, which is weak, is neglected, equation (2.5) can be integrated between z_i and $z_f < z_i$ to achieve the average number of major mergers throughout the formation history of halos. If a population of halos of mass M is chosen at redshift z_i where $M < 6M_*(z_i)$, then for $z < z_i$ the major merger rate per unit redshift is roughly constant with redshift. Therefore the very simple linear relation for the average number of major mergers halos of mass M at redshift z_i will undergo until redshift z_f is

$$\bar{N}_{\text{MM,per-prog}}(z_i, z_f, M) \approx 0.13 \times (\mu_{10} + 1)(z_i - z_f), \quad (2.8)$$

while the number of major mergers individual halos undergo is of course distributed around this average.

2.4.3 The merger rate per descendant halo

We find that the merger rate per descendant halo can be fit much better with a global fitting formula, compared with the rate per progenitor halo. We adopt the fitting form of FM08 (albeit keeping our mass ratio variable $x = 1/\xi$), and give different best-fitting parameters that express our different treatment of fragmentations (§2.3.2) and different mass definition (§2.5.3):

$$\frac{1}{N_{\text{desc-halo}}} \frac{dN_{\text{merger}}}{dzdx}(x, z, M) = AM_{12}^{\alpha} x^b \exp((\tilde{x}/x)^{\gamma}) \frac{d\delta_c}{dz}, \quad (2.9)$$

where $M_{12} = M/10^{12} M_{\odot}$ and $\delta_c \approx 1.69/D(z)$, which we estimate using the approximation provided by Neistein & Dekel (2008a).

Our best-fitting parameters are: $A = 0.06$, $\alpha = 0.12$, $b = -0.2$, $\tilde{x} = 2.5$ and $\gamma = 0.5$. Note that with the mass ratio definition used by FM08 our parameters correspond, in their

notation, to: $A = 0.06$, $\alpha = 0.12$, $\beta = -b - 2 = -1.8$, $\tilde{\xi} = 1/\tilde{x} = 0.4$, $\gamma = 0.5$, $\eta = 1$ and $\tilde{M} = 10^{12} M_{\odot}$. A detailed comparison with the results of FM08 is presented in §2.5.1.

We find this formula to fit the merger rate per descendant halo per unit redshift with deviations of up to $\approx 20\%$ for all the mass range probed by the Millennium Simulation at redshifts $z \lesssim 4$. One systematic exception is at $0.5 \lesssim z \lesssim 1.5$ and $30 \lesssim x \lesssim 1000$, where the fitting formula tends to overestimate the merger rate by up to 50%. At $z \gtrsim 4$ the redshift dependence as well as the mass dependence become stronger, and we do not make an attempt to fit that regime.

Also the merger rate per descendant halo can be integrated across cosmic times (neglecting its mass dependence) to obtain the mean number of major mergers that halos of mass M at redshift z_f have undergone since redshift z_i . If we approximate $\frac{d\delta_c}{dz}$ as 1.25 at $z > 1$ and $0.8 + 0.32z$ at $z \leq 1$ (an approximation that holds with deviations $< 10\%$) then we obtain

$$\bar{N}_{\text{MM,per-desc}}(z_i, z_f, M) \approx 0.43 M_{12}^{\alpha} \times \begin{cases} (z_i - z_f) & \text{if } 4 \gtrsim z_i, z_f \geq 1 \\ z_i - 0.65z_f - 0.14z_f^2 - 0.21 & \text{if } 4 \gtrsim z_i > 1, z_f < 1 \\ 0.65(z_i - z_f + (z_i^2 - z_f^2)/5) & \text{if } z_i, z_f \leq 1. \end{cases} \quad (2.10)$$

2.4.4 Comparison between the merger rate per progenitor halo and per descendant halo

For mergers of $x \approx 1$ at high mass/redshift the different definition of the merger rate, i.e. per progenitor halo versus per descendant halo (§2.3.3), is an important issue. Where equation (2.4) is no longer satisfied, the functional behaviour of the two is different: defining the merger rate per progenitor halo, the exponential cut-off of the merger rate enters into the $x > 1$ range, whereas defining it per descendant halo, the function increases all the way to $x = 1$, beyond which x is no longer defined. This difference is caused by attributing major mergers (e.g. between identical halos of mass M) to their approximate sum of masses. The same number of mergers is recorded by both methods, but there are far fewer halos with mass $2M$ than halos with mass M in the exponential cut-off regime.

For $x \gg 1$, or the minor merger regime, the difference between the two definitions is small. For example, the integrated rate of mergers with $10 < x < 100$ per progenitor halo is lower by $\approx 10\%$ at $z < 1$ and $M \approx 10^{13} M_{\odot}$ than the same rate per descendant halo.

We further consider the major merger rate, i.e. the merger rate integrated over $1/3 < x < 3$ (or $1 < x < 3$ for the merger rate per descendant halo). Figure 2.5 shows the merger rate per descendant halo, keeping our halo mass definition and treatment of halo fragmentation (*blue, asterisks*). Comparing Figure 2.5 to Figure 2.4 illustrates that in the low mass/redshift regime where equation (2.4) holds, the major merger rate is only slightly affected by the merger rate definition. As described in §2.4.2, above the threshold set by equation (2.4), we find the mass/redshift dependencies of the merger rate per progenitor halo to break, a different behaviour than that of the merger rate per descendant halo. At high redshift (Figures 2.5(b) and 2.4(b)), where all the masses that can be probed using

the Millennium Simulation are above the "break mass" (equation (2.4)), the different definitions lead to very different results at almost all masses.

Finally, only the merger rate per progenitor halo quantifies the rate of "destruction" events, where halos are accreted onto more massive halos, in an explicit way. This "destruction" merger rate, $x < 1$, is not defined by the merger rate per descendant halo alone. To obtain the merger rate with $x < 1$ from the merger rate per descendant halo, the halo mass function must be known. In Appendix A we develop analytic formulae that convert merger rates per descendant halo into merger rates per progenitor halo and vice versa, and also relate the merger rate per progenitor halo at $x < 1$ to that at $x > 1$. The conversion formula from the merger rate per descendant halo to the merger rate per progenitor halo is given by

$$R_p(z_p, M, x > 1) = R_d(z_d, \frac{x+1}{x}M, x) \frac{x+1}{x} N_h(z_d, \frac{x+1}{x}M) / N_h(z_p, M), \quad (2.11)$$

$$R_p(z_p, M, x < 1) = R_d(z_d, (\frac{1}{x} + 1)M, \frac{1}{x}) (\frac{1}{x} + 1) N_h(z_d, (\frac{1}{x} + 1)M) x^{-2} / N_h(z_p, M), \quad (2.12)$$

where R_p is the merger rate per progenitor halo, R_d is the merger rate per descendant halo, N_h is the mass function defined as $N_h(M) \equiv \frac{dn(>M)}{dM}$, and z_p and z_d are the progenitor and descendant redshifts, respectively. We verified numerically that those formulae describe the relations between the different merger rate definitions well.

2.5 Comparison to previous work

2.5.1 Comparison to FM08

In Section 2.3.2 we have described the differences between our method and FM08's method for building new halo trees and defining the halo mass. We show in this section that those differences have a significant effect on the results. We first discuss the differences between the dependencies on mass ratio, then compare integrated minor and major merger rates, and finally indicate the different time and mass evolutions.

Figure 2.6 shows the merger rate per descendant halo as a function of mass ratio for $10^{14} M_\odot$ halos at $z \approx 0.4$. For minor mergers FM08² also find that the merger rate varies as a power law of the mass ratio. However, they find the power law index b to be ≈ 0 ($\beta = -2.01$), i.e. find more minor mergers. This can be seen at $x \gg 1$ in Figure 2.6. The difference arises because FM08 accept most temporary links between FOF groups as mergers. This leads to an artificial inflation of the number of minor mergers. This was

²FM09's "splitting-3" method gives an almost identical merger rate to FM08's fiducial "stitching-3" method, in spite of the differences between the algorithms. An examination of Table 2.1 shows that it is probable that those differences compensate each other between the scenarios in the third and fifth columns of that Table.

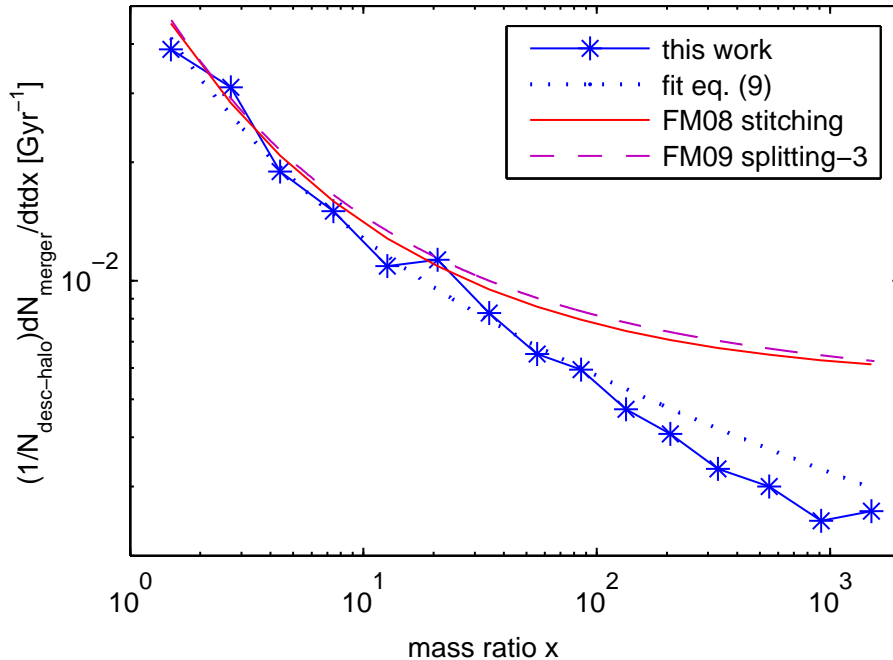


Figure 2.6: The merger rate per descendant halo for $10^{14} M_{\odot}$ halos at $z \approx 0.4$, comparing the results of our splitting algorithm to FM08’s ”stitching” algorithm and FM09’s ”splitting-3” algorithm (C.-P. Ma, priv. comm.), which both give virtually the same results. We find a lower merger rate, starting from $\approx 6\%$ at $x \lesssim 10$ and increasing steadily to a factor of 2 at $x \approx 1000$. About half of the difference originates in the different halo mass definition (§2.5.3), and about half from our algorithm that never counts the same merger more than once.

anticipated by FM08 themselves, and is also supported by the finding that subhalos that are ejected out of their host halos are preferentially of low mass (Ludlow et al., 2009). The second significant parameter that depends on the tree building method is \tilde{x} (see equation (2.9)). For the ”snipping” method FM08 found that the best-fitting value is ≈ 58 , and for the ”stitching” method ≈ 10 , while we find the best value to be $\tilde{x} = 2.5$. This means that the dependence of the merger rate on mass ratio in our method is closer to a pure power-law (since the exponential term affects mostly $x \lesssim \tilde{x}$). The larger the number of false (mostly minor) mergers that are counted, the stronger the exponential term should be, and the steeper the power-law.

The integrated minor merger rate per descendant halo of mergers between 10 : 1 and 100 : 1 at $z \approx 0.24$ as a function of mass is shown in Figure 2.7. It shows that the ”snipping” and ”stitching” methods (*dashed and solid curves*) overestimate the minor merger rate that we find. Roughly half of this difference originates from properly removing all artificial mergers, and equally important is the difference in the mass definition of halos (see §2.5.3). Note that while Table 2.1 shows that $\approx 80\%$ of all mergers are treated equally by all

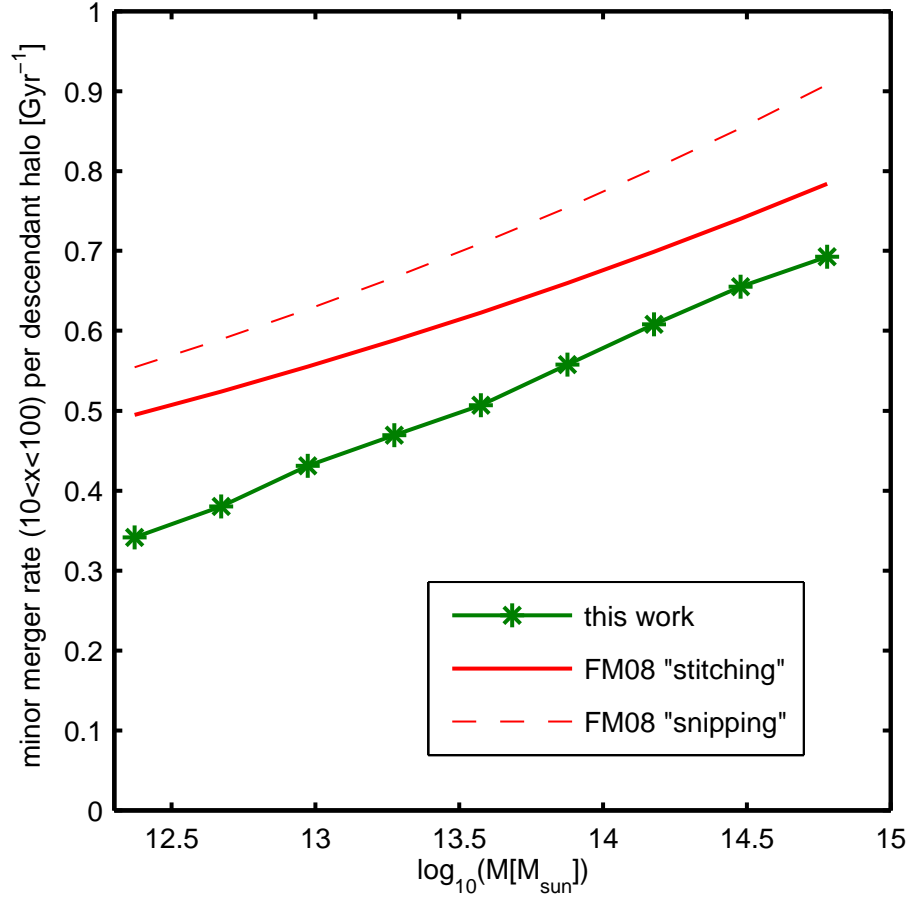


Figure 2.7: The integrated merger rate per descendant halo per unit time of minor mergers between 10 : 1 and 100 : 1, as a function of mass at $z \approx 0.24$. The mass resolution of the simulation allows this rate to be directly measured only for $M \gtrsim 10^{12.4} M_{\odot}$. Appropriate treatment of halo fragmentation and an appropriate halo mass definition are significant in this regime. Not giving any special treatment to the fragmentation of halos, thereby counting artificial mergers (FM08’s ”snipping” method, *dashed red*) leads to a significant overestimate of the merger rate. FM08’s ”stitching” method (*solid red*) still overestimates this minor merger rate by a factor ≈ 1.3 compared to our method (*green, asterisks*), due to their acceptance as mergers of most temporary links between FOF groups and their definition of a halo mass.

methods, a large fraction of all mergers are rather major mergers between rather low mass halos, simply because of the large abundance of low mass halos. Among minor mergers, which involve halos much more massive than the mass resolution limit, many belong to the other $\approx 20\%$ that are treated differently by the different methods.

The comparison in the major merger regime can be seen in Figure 2.5. The merger rate we find is systematically lower than FM08's also due to our splitting algorithm but, in this regime, mainly due to the different halo mass definition. This is especially true at low mass (Figure 2.5(a)) and low redshift (Figure 2.5(c)).

We find the redshift dependence of the merger rate to be proportional to $\frac{d\delta_c}{dz}$, while FM08 find a slightly weaker redshift evolution at low redshift by introducing $(\frac{d\delta_c}{dz})^\eta$ with $\eta \approx 0.3$. The consequence of $\eta = 1$ is discussed further in §2.5.2. We also find a slightly stronger mass dependence, $\alpha = 0.12$ rather than $\alpha \approx 0.08$.

2.5.2 Comparison to the EPS model

Figure 2.8 compares different results for the merger rate per descendant halo of $10^{14} M_\odot$ halos at $z \approx 0.4$. The merger rate per descendant halo is the natural quantity that is obtained from the EPS model, and does not require explicitly the mass function of halos.

FM08 found that the EPS model predicts more major mergers and (especially) fewer minor mergers compared with the Millennium Simulation. The slope of the merger rate at $x \gg 1$ is determined by the parameter b in equation (2.9). The larger it is, the more minor mergers dominate the number of mergers. Indeed, FM08's "snipping" method, which doesn't reject any artificial mergers, finds $b = 0.17$, while their fiducial "stitching" method (red curve in Figure 2.8(a)) finds $b = 0.01$. The value we find, by rejecting *all* artificial mergers (blue curve with asterisks in Figure 2.8(a)), is $b = -0.2$, while the Lacey & Cole (1993) EPS prediction (green curve with open circles in Figure 2.8(a)) is $b \approx -0.5$. Therefore, we find, like FM08, that the EPS model overpredicts the major merger rate, but we find a better agreement with EPS in the minor merger regime, because we don't accept artificial minor mergers.

Recently Neistein & Dekel (2008b) have constructed a new method for predicting merger rates from the EPS model, by avoiding the assumption of binary mergers, which leads to inconsistency within EPS. They find, in agreement with the simulation, that the Lacey & Cole (1993) merger rates are too low in the minor merger regime. Moreover, we find that the Neistein & Dekel (2008b) merger rate (green curve with filled circles in Figure 2.8(a)) has at $x \gg 1$ a slope of $b = -0.19 \pm 0.02$, i.e. its shape agrees remarkably well with what we find in the Millennium Simulation. The Neistein & Dekel (2008b) merger rate is higher than the merger rate we find in the Millennium Simulation by a factor of $\approx 1.5 \pm 0.3$, for all mass ratios, halo masses and redshifts, with almost no systematic dependence on any of those parameters.

This result is further demonstrated in Figure 2.8(b). The Neistein & Dekel (2008b) merger rate is constant with respect to the natural dimensionless EPS time variable δ_c , which is exactly the same dependence we find in the simulation. Figure 2.8(b) compares the major merger rate per descendant halo of $M \approx 10^{12.5} M_\odot$ halos between FM08's "stitching"

method, the method presented here, and Neistein & Dekel (2008b). The redshift dependence of FM08’s method is significantly different at low redshift (originating numerically from their best-fitting value of $\eta \approx 0.3$), because artificial mergers appear preferentially at low redshift. The redshift dependence of the merger rate in the Millennium Simulation based on our method matches well that of EPS (see also Neistein & Dekel, 2008a), but the normalisation, as already mentioned, has an offset.

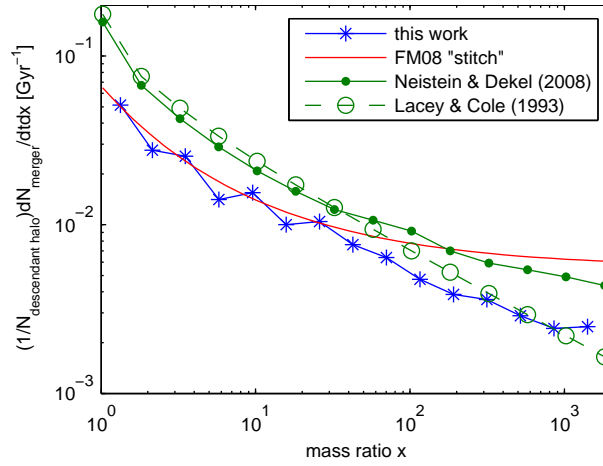
2.5.3 The role of the halo mass definition

There is a substantial uncertainty as to how to determine the boundaries of halos in N-body simulations. Sometimes the mass of halos is taken as the mass inside a sphere, within which the density equals the expected density of virialised groups in the spherical collapse model. This class of definitions is not well-suited for our purposes, because they are less reliable for halos undergoing mergers (White, 2001; Lukić et al., 2009). Particles grouped together by the FOF algorithm are considered to correspond to virialised dark matter halos, because their average density approximately equals the expected density of virialised groups in the spherical collapse model, yet the halos can have any shape and are not assumed to be spherical. On the other hand, undesired effects like particle bridges between halos (as discussed in §2.3.2) and spurious linkage of particles to groups are inherent to the algorithm. An advantage of SUBFIND over FOF is that it subjects the (geometrically-identified) groups of particles to a dynamical test. Only particles that are found to be gravitationally bound to their subhalo are included as part of their subhalo’s mass. Therefore, two reasonable definitions we consider for the mass of a halo are: (1) the total mass of all the particles associated with the halo by the FOF algorithm (as in e.g. FM08), and (2) the total mass of all the particles that belong to the halo and are also gravitationally bound to any of its subhalos.

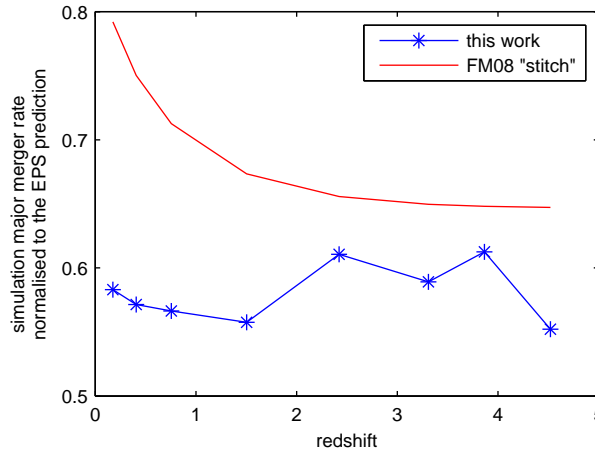
As described in §2.3.2, for the population of halos as a whole, the difference between those two definitions is not large. For example, the average fraction of unbound particles is $\approx 3\%$. Nevertheless, there is a distinct population of halos for which the typical fraction is much larger. These are halos that are about to undergo a significant merger, i.e. undergo a major merger or be accreted onto a more massive halo. First we describe how this affects the merger rate, and then interpret this phenomenon and justify our choice of not including the unbound particles when computing the merger rate.

Halos at snapshot s that are about to undergo a merger have on average higher ratios of total FOF mass over bound SUBFIND mass. We find that the total-over-bound mass ratio of a halo correlates with two quantities related to a halo’s next merger: 1) the time before the next merger begins, relatively to the dynamical time $\propto H(z)^{-1}$, and 2) the mass ratio of that merger. Specifically, as a halo approaches a merger with another halo of comparable or larger mass, its total-over-bound mass ratio increases with time, an effect that is stronger as the mass of the other halo is larger. This phenomenon can be well quantified for $x \leq 3$ by

$$\frac{M_{FOF}}{M_{bound}}(x \leq 3) = 1.02 \times t_{left,dyn}^{-0.018} \times x^{-0.005 \times t_{left,dyn}^{-0.55}}, \quad (2.13)$$



(a)



(b)

Figure 2.8: A comparison between different results for the merger rate per descendant halo per unit time. Panel (a) illustrates the merger rate for $M \approx 10^{14} M_{\odot}$ at $z \approx 0.4$. Four different methods are shown: using the splitting algorithm and the mass definition presented in §2.3 (*blue, asterisks*), FM08’s fit to their “stitching” method (*dashed red*), the Neistein & Dekel (2008b) EPS method (*green, filled circles*) and the Lacey & Cole (1993) EPS method (*dashed green, open circles*). At $x \lesssim 30$, the two EPS methods are similar and exceed the two methods based on the Millennium Simulation by $\approx 70\%$. As x increases towards more minor mergers, FM08’s merger rate is the shallowest, finding the highest number of minor mergers, while the EPS method of Lacey & Cole (1993) is the steepest, finding the lowest number of minor mergers. On the other hand, the slopes found by our analysis and by the EPS method of Neistein & Dekel (2008b) are similar, so that a roughly constant ratio is kept between the inferred merger rates (§2.5.2). Panel (b) compares the integrated major merger rate ($1 \leq x \leq 3$) of $M \approx 10^{12.5} M_{\odot}$ halos, as a function of redshift, that results from our method (*blue, asterisks*), FM08’s “stitching” method (*dashed red*) and the Neistein & Dekel (2008b) EPS method, with which both other methods are normalised. The redshift dependence resulting from our analysis of the simulation agrees well with that of the EPS prediction (yet, again, with an offset in the normalisation), while FM08 find more mergers at low redshift because their method is more sensitive to artificial mergers, which are more common at low redshift.

where $t_{left,dyn} \equiv t_{left}H(z)$, and t_{left} is the time left before the merger starts (which is defined for this purpose as the middle of the time interval between the adjacent snapshots of the progenitors and the descendant). $\frac{M_{FOF}}{M_{bound}}$ denotes the geometrical mean over all halos, a quantity that is used because the scatter is large. Halos that are approaching a minor merger ($x > 3$) show almost no enhancement of the total-over-bound mass ratio, therefore we fit it as

$$\frac{M_{FOF}}{M_{bound}}(x > 3) = 1.02 \times t_{left,dyn}^{-0.007}. \quad (2.14)$$

Figure 2.9 demonstrates this phenomenon and its description by equations (2.13) and (2.14) for halos at $z \approx 3$.

Since the more massive halo of the merging pair (or group) retains the typical value of ≈ 1.03 , and the less massive halos have untypically large total-over-bound mass ratios, the mass ratios of mergers shift towards smaller values (mergers become more equal-mass) when the total mass is taken into account, compared with the choice of the bound mass as the halo mass. The effect on the merger rate is pronounced. When the halo mass is taken as the total mass, there is a deficiency of very high mass ratio mergers near the resolution limit, but since we restrict our analysis to mergers with halos of $M/x > 2 \times M_{min}$, this is not seen. What is seen is an enhancement of the merger rate for every $x < M/(2 \times M_{min})$. The merger rate using the total FOF mass is larger by typically 20% and up to $\approx 50\%$ than our fiducial method. Figure 2.10 demonstrates this difference. Furthermore, Figure 2.10 shows that using the mean relations equations (2.13) and (2.14) to interchange between the two halo mass definitions allows reproducing the different resulting merger rates.

The total-over-bound mass ratio of halos correlates also with the environment in which they reside. Figure 2.11 shows that halos in denser environments have higher total-over-bound mass ratios (*solid curves*). This trend holds also among halos that are about to undergo a $x < 1$ merger in the following snapshot (*thin blue*). Yet, once each halo's total-over-bound mass ratio is normalised by the value expected for it by equations (2.13) and (2.14), the correlation with the environment almost disappears (*dashed curves*). The difference, at a given overdensity, between all halos and halos about to undergo a $x < 1$ merger shows that it is not possible to use the correlation with the environmental overdensity to disentangle the dependence shown in Figure 2.9. This means that the environmental dependence is probably just a second-order correlation, originating from the correlation shown in Figure 2.9 in combination with the correlation between mergers and environment (cf. FM09).

The strong correlation of the total-over-bound mass ratio of halos with their proximity to their next merger and its mass ratio, and the fact that there is almost no additional dependence on environment, suggest that the mergers themselves are responsible for the change in the total-over-bound mass ratio. The question to be asked is whether this is a gravitational effect, which changes the bound mass even before the FOF groups merge, or a numerical effect, which changes the FOF group mass even before the gravitational interaction is significant. To give a fully satisfactory answer to that question, a detailed dynamical analysis is needed, which cannot be obtained with just the merger trees, and is

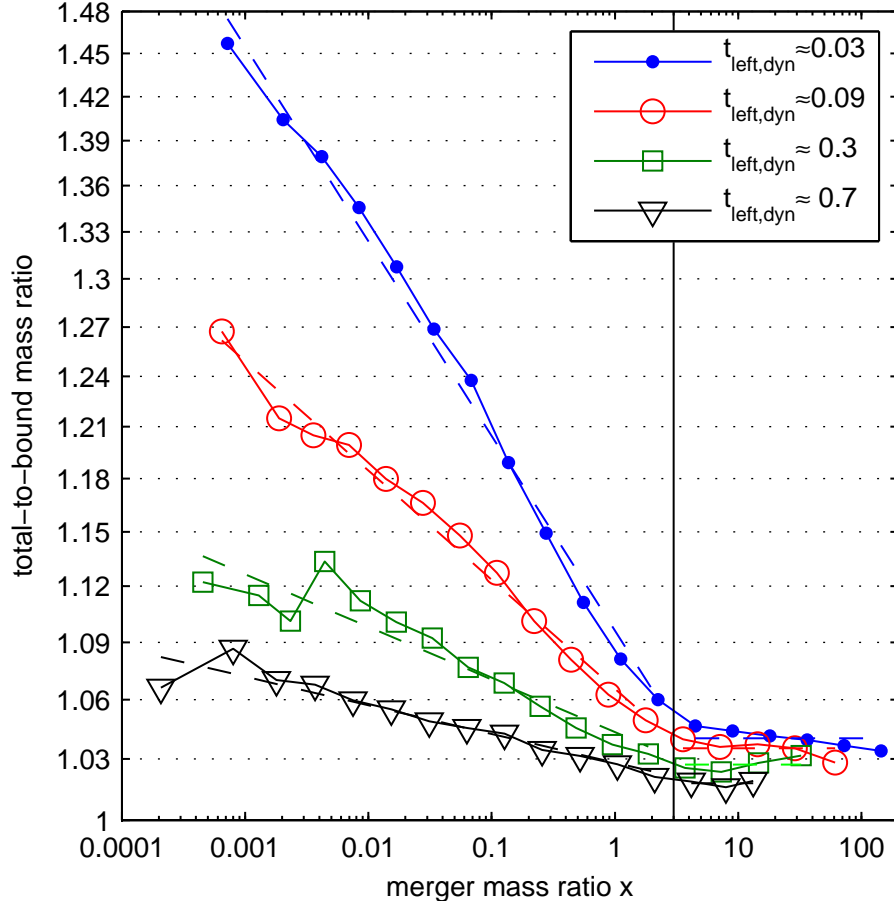


Figure 2.9: The ratio of the total FOF mass of halos to their total SUBFIND bound mass, as a function of the mass ratio of the merger they are about to undergo. The more massive the other halo (the smaller x), the larger the total-over-bound mass ratio enhancement, but minor mergers ($x > 3$, to the right of the horizontal line) have almost no effect. The more imminent the merger, normalised to the dynamical time, the larger its influence on the halo’s total-over-bound mass ratio. These trends are shown by 4 different curves, each representing halos that are about to undergo such a merger in a fixed ”normalised time” into their future, as indicated by the legend. All halos shown here are at the same snapshot, $z \approx 3$, but the fitting formulas equations (2.13) and (2.14), which are shown by the dashed curves, hold for all redshifts. Since $H(z \approx 3) \approx 0.3 \text{ Gyr}^{-1}$, the curves in this figure correspond to halos that are about to undergo a merger in 0.1, 0.3, 1, 2.4 Gyr into their future, which corresponds to 1, 2, 5, 10 simulation snapshots, from top to bottom respectively.

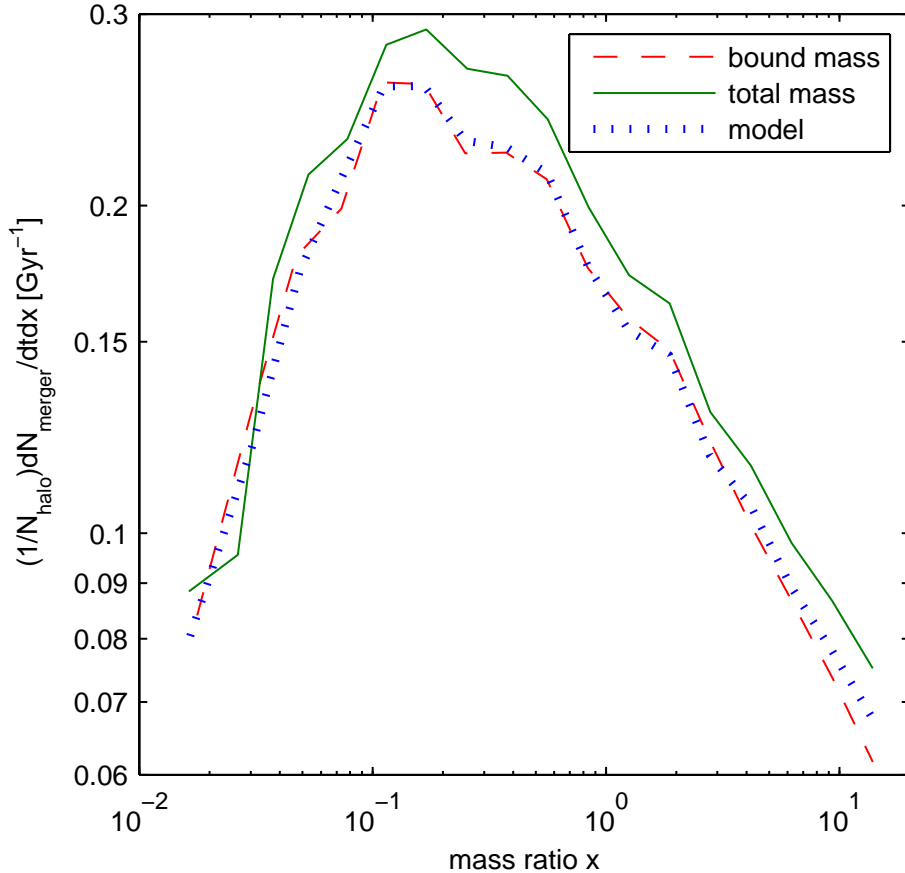


Figure 2.10: The merger rate per progenitor halo for halos of $M \approx 10^{12} M_{\odot}$ at $z \approx 3$, extracted using the total FOF group mass as the halo mass (*solid green*) and using only the bound mass as the halo mass (*dashed red*). When the halo mass is defined as the total FOF mass, including gravitationally unbound particles, the inferred merger rate is higher by up to 50% (in a similar way for all masses at all redshifts). This is caused by the fact that halos that are about to merge with more massive halos have unusually high total-to-bound mass ratios. To check whether this is the only source of difference, we used the merger trees in which the mass is defined as the total mass, and changed them according to equations (2.13) and (2.14), computing $t_{left,dyn}$ for $z \approx 3$ and a 1 snapshot difference. Specifically, each halo’s mass was reduced by 4.55%, except for the mass of halos about to undergo a merger of mass ratio $x \leq 3$, which was reduced by a factor of $1.087x^{-0.0348}$. Although this model doesn’t include the scatter in the total-over-bound mass ratio, the result (*dotted blue*) is very similar to the results achieved directly with each halo’s bound mass. The integral of the merger rates with both mass definitions between $x = 0$ and $x = M/M_{min}$ is by construction equal. Nevertheless, we restrict our results to $x \leq M/(2 \times M_{min})$, so the sharp, artificial, drop of the solid green curve at $x > M/(2 \times M_{min})$ is not seen.

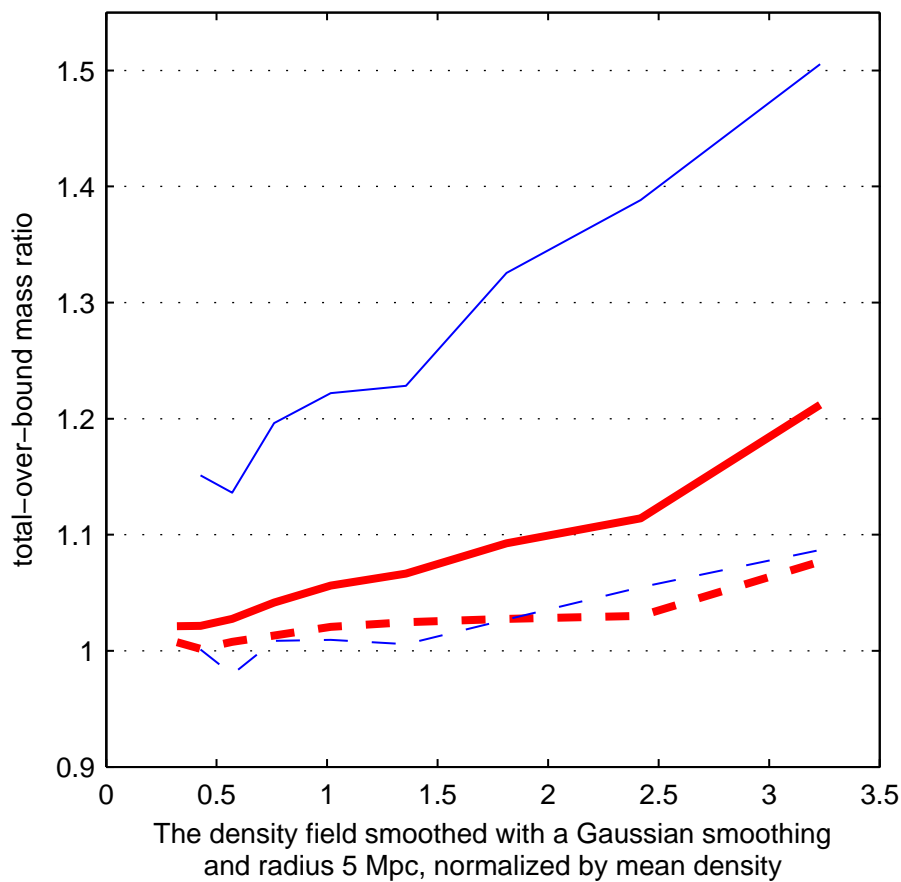


Figure 2.11: The total-over-bound mass ratio of FOF groups as a function of their environment and merging state. Halos residing in denser environments have on average higher total-over-bound mass ratios (*thick red*). The same is true for a sub-population of halos that are just about to merge onto a more massive halo (*thin blue*). Also, for a given overdensity, halos that are just about to merge onto a more massive halo have significantly higher total-over-bound mass ratios, in accordance with Figure 2.9. Yet, once each halo’s total-over-bound mass ratio is normalised by the value expected for it by equations (2.13) and (2.14), the correlation with the environment almost disappears (*dashed curves*). This figure shows halos at $z \approx 1$, but we find the same trends at any redshift, and for any available choice of a smoothing length: 1.25, 2.5, 5, 10 Mpc.

outside the scope of this chapter. Nevertheless, Figure 2.12 shows that it is not the bound mass that decreases before the merger, but the total mass that increases more rapidly, that causes the total-over-bound mass ratio to increase. We postulate that a significant amount of particles are added to the outskirts of the FOF group during the few snapshots before the merger, but are not found to be bound to it. Therefore, we favour the interpretation of the bound mass as the "true" mass of the halo.

2.6 Comparison to observations

The two different definitions of the merger rate, per progenitor halo and per descendant halo, have different physical meanings, and they correspond to the two different observational approaches towards measuring the galaxy merger rate. When the merger rate is measured via pair counting, the mass (or luminosity) of each galaxy in the pair is measured separately, and the merger fraction/rate is attributed to the measured progenitor galaxy mass. The merger rate in this case is related to the time scale for galaxies of a given mass/luminosity to encounter other galaxies of a given mass/luminosity, analogously to the merger rate per progenitor halo. In the case of morphological/kinematical identification of disturbed galaxies that show signs of mergers, it is difficult to infer the mass of each of the original components that have merged, and the merger is then attributed to the total mass of the system, i.e. the descendant mass. In that case, the merger rate is related to the time scale on which a population of galaxies is created by mergers. While such observations still suffer from large uncertainties, it is important to realise that the merger rates that are inferred by both methods are not the same quantity. Those two quantities are related to each other by our conversion formula, in a fully analogous way to the two definitions of the merger rate of dark matter halos.

Some evidence for the expected difference between the two methods can be found in the literature. For example, Maller et al. (2006) measure the galaxy major merger rate in a cosmological hydrodynamic simulation, and define it as being per descendant galaxy. They find a steep monotonic relation between increasing mass and increasing merger rate, similar to the trend of the halo merger rate per descendant. Also Conselice et al. (2008), measuring the merger fraction using a morphological investigation, find that the merger fraction (at $z \gtrsim 1.5$) increases strongly with increasing mass. On the other hand, Patton & Atfield (2008) find that the major merger rate of galaxies, obtained via observed pair counting, peaks with respect to luminosity, therefore also with respect to mass. This different dependence, which at first might seem to be at odds with the findings of Maller et al. (2006) and Conselice et al. (2008), is actually qualitatively expected once it is taken into account that Patton & Atfield (2008) measure (implicitly) the merger rate per *progenitor* galaxy. Therefore, when comparing either observed or simulated galaxy merger rates, the nature of the observations and the definition used to analyse the simulations must be taken into account. Similarly, Conselice et al. (2008) find that the redshift dependence of the merger fraction becomes stronger for higher mass galaxies, while de Ravel et al. (2009), measuring the pair fraction of galaxies, find exactly the opposite trend, i.e. that higher mass galaxies

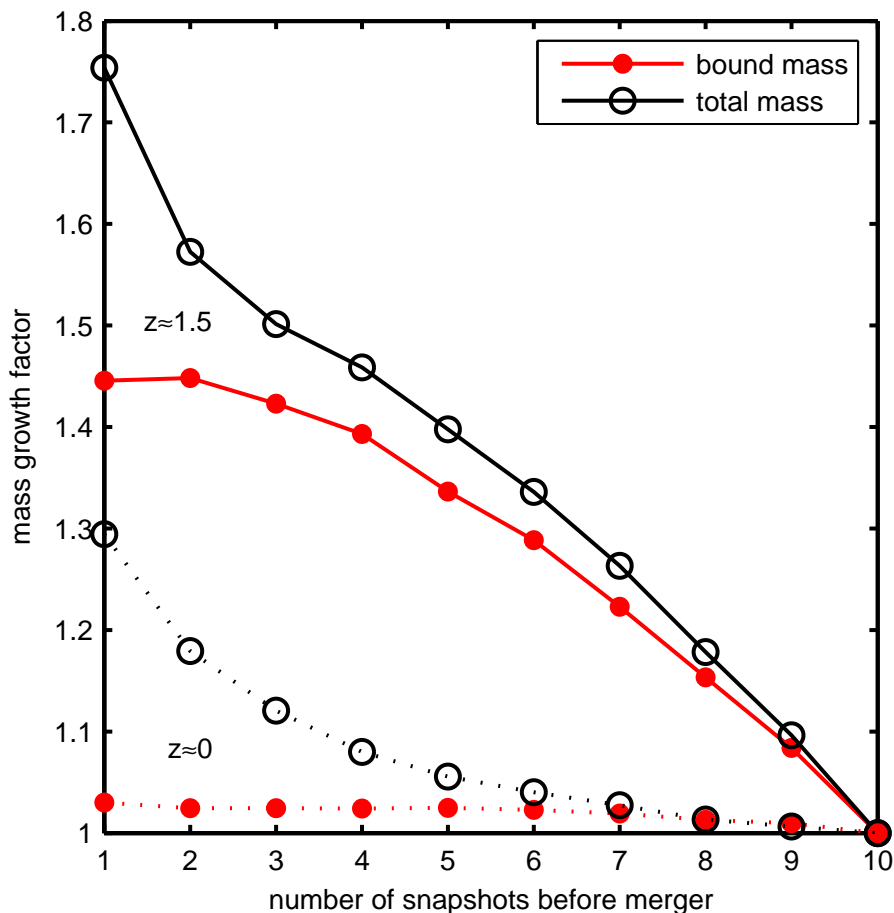


Figure 2.12: Mean mass growth histories for halos that are about to undergo a merger of $0.0005 < x < 0.01$ at $z \approx 0$ (*dotted*) or $z \approx 1.5$ (*solid*), for 10 subsequent snapshots before the merger. Both the total FOF group mass (*empty circles*) and the bound mass (*filled circles*) are shown. Each curve is normalised to 1 at the time of 10 snapshots before the merger. It is seen that the total mass grows faster than the bound mass, which results in increased total-over-bound mass ratios as these halos approach a merger with a more massive halo. For halos not about to undergo a significant merger, the total and bound mass grow at the same rate, thereby conserving the mean ratio of ≈ 1.03 .

have a shallower redshift evolution. This is again in qualitative agreement with our expectations based on the difference between merger rates per progenitor and per descendant halo/galaxy.

To quantitatively compare observations with the frequency of galaxy mergers predicted by simulations, a treatment of baryonic physics must be included. Such a comparison is outside the scope of this chapter, but can be found in e.g. Bertone & Conselice (2009) and Hopkins et al. (2010b). However, we make here a comparison between the halo merger fraction (per descendant halo) in the Millennium Simulation and galaxy merger fractions (per descendant galaxy) from observations. In Figure 2.13 we show a compilation of observed galaxy merger fractions as a function of redshift. Two features are apparent: the merger fraction increases with redshift, and the scatter at any given redshift is roughly a factor of 5. If we distinguish between fractions according to a rough luminosity/mass criteria, the large scatter remains. This is because the scatter is caused by numerous factors, e.g. selection of different populations and different wavebands, different techniques for identifying mergers, as well as cosmic variance.

To extract merger fractions from the simulation, a time scale must be associated with mergers (see also Genel et al., 2008). We use the dynamical friction time scale for dark matter halo mergers found by Boylan-Kolchin et al. (2008) based on merger simulations. We average the orbital parameters and thereby obtain $T_{\text{merger}} = 0.7 \frac{r^{1.3}}{\ln(1+r)} \frac{H(z=0)}{H(z)}$ Gyr, where r is the mass ratio and $H(z)$ is the Hubble constant at redshift z . Whenever a major merger occurs between snapshots s and $s+1$ (§2.3.3), we tag the most massive progenitor at snapshot s , and its descendants in following snapshots, as "undergoing a major merger" for a time T_{merger} after snapshot s . This allows us to determine, for any snapshot and halo mass range, the fraction of halos that are instantaneously undergoing major mergers, i.e. the major merger fraction. In Figure 2.13 we plot the resulting major merger fraction as a function of redshift for three halo masses.

We note that by tagging the progenitor halo only at snapshot s and the descendant halos in the following snapshots for a duration T_{merger} , we derive a merger fraction that is mostly "per descendant halo". We do that for two reasons. First, while a halo that is a descendant of a merger is a halo that hosts galaxies that are about to merge, it is probably observationally less relevant when two halos are still approaching their merger. Second, it is unclear what time scale should be used for an imminent halo merger. The dynamical friction time scale is relevant only after the halos have started coalescing (Boylan-Kolchin et al., 2008). In other words, there is no proper definition for a "halo pair". We also note that the exact algorithm used for building the merger tree and the halo mass definition become relatively unimportant in this comparison due to the large uncertainties. Stewart et al. (2009), who performed a similar analysis, have also shown that it is possible to find a good rough agreement with observations while having much freedom in parameters like mass ratio and time scale.

The theoretical expectation for the dark matter halo merger fraction brackets the observations reasonably well. This suggests that, at least within the current uncertainties, the galaxy merger fraction roughly follows the dark matter halo merger fraction. This con-

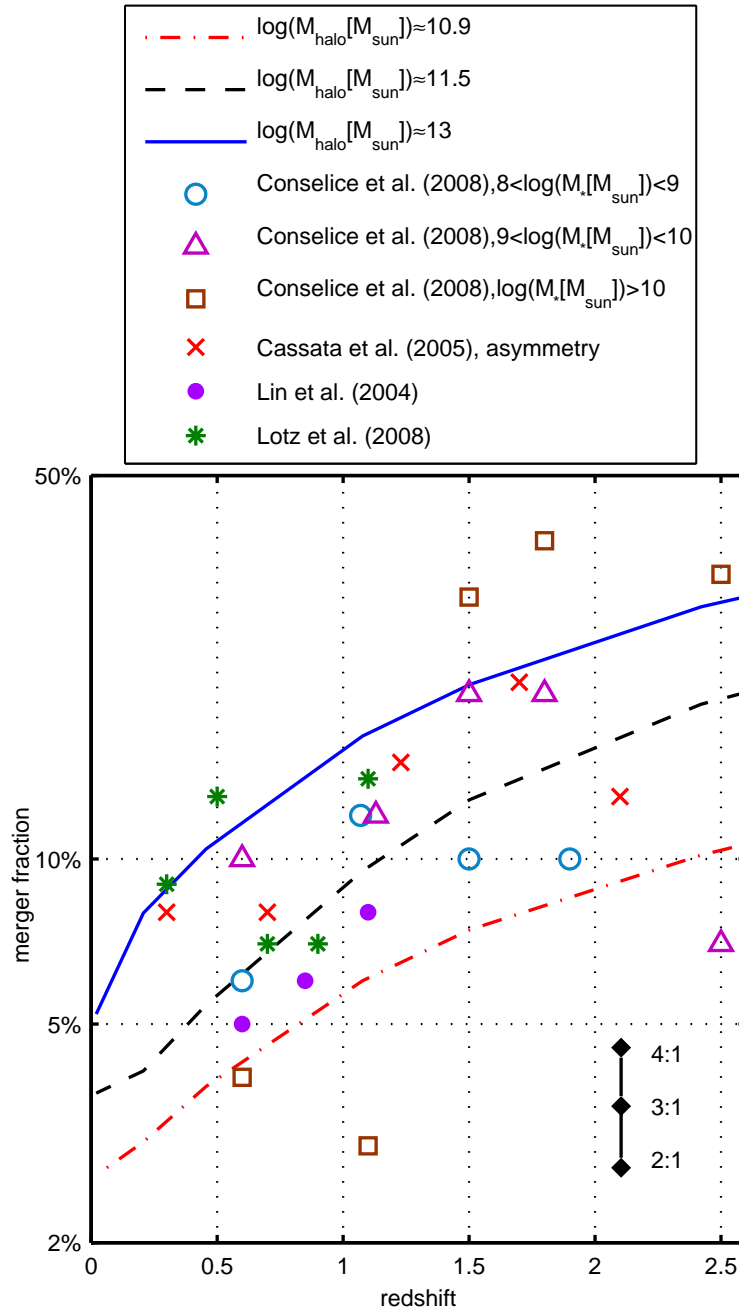


Figure 2.13: The merger fraction as a function of redshift. Values for dark matter halos undergoing major mergers (with a mass ratio threshold of 3) in the Millennium Simulation are shown for 3 different halo masses, starting from the lowest halo mass we can reliably probe, that is $\approx 10^{10.9} M_{\odot}$. The sensitivity to the chosen mass ratio threshold is indicated in the lower right corner. A compilation of observational values that were obtained in different methods and with different selections nevertheless shows a rough agreement, also with the results from the simulation. The error bars of the observations are largely comparable or smaller than the spread, and for the simulation (Poisson errors) they are very small. They have been suppressed to allow better readability.

clusion may seem to be different from the findings of Guo & White (2008), namely that the role of major mergers in galaxy growth is different from that in halo growth, but the two conclusions are actually consistent with each other. Guo & White (2008) found that the specific formation rate of halos through major mergers increases steeply with redshift but depends weakly on mass, and vice versa for galaxies. Nevertheless, the specific formation rate they introduced is a different quantity from the merger fraction we show in Figure 2.13. Guo & White (2008) defined the specific formation rate such that it equals the merger rate per descendant halo as defined in this work, times the Hubble time, with no dependence on the duration of mergers. Thus, the difference they found between halos and galaxies originates solely from the difference of the merger *rate* between halos in the dark matter simulation and the galaxies in the semi-analytical model. Guo & White (2008) found that the galaxy specific formation rate via major mergers is roughly constant with redshift, therefore by dividing it by the Hubble time, we learn that the galaxy major merger rate scales roughly as $(1+z)^{1.3}$. In comparison, they find that the halo specific formation rate via major mergers scales as $(1+z)^1$, which after being divided by the Hubble time means that the halo major merger rate scales as $(1+z)^{2.3}$. This is consistent with our finding that the halo major merger rate scales roughly as $(1+z)^2$. However, the merger *fraction* is proportional also to the merger time scale. The time scale of halo mergers T_{merger} scales roughly as $(1+z)^{-1.3}$ via its dependence on the Hubble time, while the observed time scale for galaxy mergers is probably approximately constant with redshift (e.g. Conselice, 2006; Kitzbichler & White, 2008). Combining these dependencies, one finds that both the halo merger fraction and the galaxy merger fraction scale roughly as $(1+z)^1$, which is indeed what is seen on average in Figure 2.13.

2.7 Summary and discussion

We have used the Millennium Simulation to extract merger rates of dark matter halos. Our method differs from previous work in three main aspects.

First, we reject any merger between FOF groups whose descendant subhalos, at any future time, do not belong exclusively to the same FOF group. This is done by keeping such FOF groups distinct until they (if at all) irrevocably merge. Rejecting only a fraction of such events, as in previous work, leads to double counting of mergers, and to false counting of fly-by events as mergers. Therefore, our method results in a lower merger rate, especially in the minor merger regime. Ludlow et al. (2009) find that ejections of low mass subhalos out of their host halos typically occur in a configuration where a bound group of subhalos (which was created via past mergers) is accreted onto a large halo, and its low mass members are propelled onto high energy orbits by the multiple-body interaction. In the context of merger counting, it is not clear whether the merger of the low mass halo with the group should be counted as a merger, or merely regarded as an interaction that was interrupted by the accretion of the group onto the large halo. Our method assumes the latter for reasons described in §2.3.2. Therefore, in a more conservative approach, our results can be regarded to as a strong lower limit for the merger rate.

Second, we define each halo’s mass as the mass of all the particles gravitationally bound to it, rather than of all the particles constituting the FOF group. This definition reduces the inferred merger rate by typically 20%. The motivation for this definition is our finding that the total (bound & unbound) mass of FOF groups artificially increases by up to 50% as they approach more massive FOF groups on their way to merge with them. This effect distorts the appropriate mass ratios of mergers, thereby changing the merger rate. A detailed discussion of this issue appears in §2.5.3.

These two improvements make our inferred merger rate more consistent with the new predictions of Neistein & Dekel (2008b) based on the EPS model, in the sense that the functional dependencies of the merger rate on mass ratio, halo mass and redshift are very similar. There is a constant factor of ≈ 1.5 between the EPS merger rate and the Millennium Simulation merger rate. In §2.4.3 we provide a simple global fitting formula (equation (2.9)) for the merger rate per descendant halo that holds for $z \lesssim 4$ and all masses probed by the Millennium Simulation.

Third, we also extract the merger rate per *progenitor* halo. This allows us to find a merger rate for the full range of mass ratios. For halos of any mass M , we can measure the rate at which they undergo minor mergers, major mergers and the rate at which they are being accreted as satellite halos onto more massive halos. This has significant implications for the redshift and mass dependencies of the major merger rate. We find the merger rate, in the regime where both halo masses are smaller than the knee of the mass function, to increase steeply with redshift and only slightly with mass, in a similar way to what was found in previous work. However, at high enough mass or redshift, the number of halos decreases exponentially and therefore the mass dependence of the major merger rate changes sign and starts decreasing with increasing mass. Also, the redshift dependence significantly weakens. In §2.4.4 we provide an analytic expression for converting merger rates per descendant halo to merger rates per progenitor halo, which can be used for any theoretical merger rate.

The two different definitions of the merger rate, per progenitor halo and per descendant halo, have different physical meanings. They also correspond to the two different observational approaches towards measuring the galaxy merger rate, namely pair counting and morphological/kinematical identification. In §2.6 we discuss the importance of this distinction and its relevance to observations. Finally, we find that observed galaxy merger fractions are consistent with the halo merger fraction in the Millennium Simulation within the large observational uncertainties and uncertainties in parameters (like mass ratio or time scale) needed to compare the two. More refined comparisons still await significant improvements both in observational techniques and consistency and in the theoretical treatment of baryonic physics.

Chapter 3

Dark matter halo growth: evidence for smooth accretion

Note: This chapter has been published in Genel et al. (2010a).

3.1 Abstract

We study the growth of dark matter halos in the concordance Λ CDM cosmology using several N-body simulations of large cosmological volumes. We construct merger trees from the Millennium and Millennium-II Simulations, covering the ranges $10^9 - 10^{15} M_{\odot}$ in halo mass and $1 - 10^5$ in merger mass ratio. Our algorithm takes special care of halo fragmentation and ensures that the mass contribution of each merger to halo growth is only counted once. This way the integrated merger rate converges and we can consistently determine the contribution of mergers of different mass ratios to halo growth. We find that all resolved mergers, up to mass ratios of $10^5 : 1$, contribute only $\approx 60\%$ of the total halo mass growth, while major mergers are subdominant, e.g. mergers with mass ratios smaller than $3 : 1$ ($10 : 1$) contribute only $\approx 20\%$ ($\approx 30\%$). This is verified with an analysis of two additional simulation boxes, where we follow all particles individually throughout cosmic time. Our results are also robust against using several halo definitions. Under the *assumption* that the power-law behaviour of the merger rate at large mass ratios can be extrapolated to arbitrarily large mass ratios, it is found that, independent of halo mass, $\approx 40\%$ of the mass in halos comes from genuinely smooth accretion of dark matter that was never bound in smaller halos. We discuss possible implications of our findings for galaxy formation. One implication, assuming as is standard that the pristine intergalactic medium is heated and photoionized by UV photons, is that all halos accrete $> 40\%$ of their baryons in smooth "cold" $T \gtrsim 10^4$ K gas, rather than as warm, enriched or clumpy gas or as stars.

3.2 Introduction

The way galaxies gain their mass affects almost every aspect of galaxy evolution. The distinction between, e.g., accretion of gas versus stars, spherical versus filamentary accretion, or clumpy versus smooth accretion will result in very different star-formation histories, colours, morphologies, angular momentum contents and sizes. Mergers are believed to play an important role in the evolution of galaxies, in particular of elliptical galaxies via the morphological transformation from disk-dominated galaxies to spheroids (e.g. Toomre, 1977; Barnes & Hernquist, 1992; Naab & Burkert, 2003; Naab et al., 2006b; Cox et al., 2006a; Hopkins et al., 2008a; Naab et al., 2009; Conselice et al., 2003; Bell et al., 2006a; Lotz et al., 2008a). Both theoretical and observational work have also emphasised the importance of smooth accretion of gas, in particular for the buildup of massive galaxies at high redshift and for the subsequent evolution of disk galaxies (e.g. White & Frenk, 1991; Murali et al., 2002; Ocvirk et al., 2008; Dekel et al., 2009b; Goerdt et al., 2010; Daddi et al., 2007; Förster Schreiber et al., 2009; Conselice & Arnold, 2009; Kauffmann et al., 2010). The gas can be accreted in a spherically symmetric mode of cooling halo gas or in a filamentary mode directly from the cosmic web.

In the cold dark matter paradigm for structure formation (Blumenthal et al., 1984), galaxy formation is closely related to the formation of dark matter halos (White & Rees, 1978), albeit in a complex way. Baryons follow the flow of the gravitationally-dominating dark matter and fall into dark matter halos, and galaxy mergers follow the mergers of their host dark matter halos. Understanding the process of halo mass assembly is an important step towards a better understanding of galaxy formation. In this chapter we use high resolution dark matter simulations to study the relative importance of mergers versus smooth accretion for the buildup of halos and galaxies.

The non-linear nature of the evolution of gravitational instabilities into virialised structures makes N-body simulations the most reliable tool available for studying the mass buildup of dark matter halos. Massive dark matter particles in N-body simulations are believed to give a good representation of the coarse-grained phase-space structure of real dark matter. However, the interpretation of dark matter simulations is subject to some freedom and uncertainty in subsequent steps in making the connection to galaxies, such as the definition of a dark matter halo (e.g. White, 2001, 2002; Cohn & White, 2008; Tinker et al., 2008) and algorithms of merger tree construction.

One of the largest simulations used so far for studying the growth of dark matter halos is the Millennium Simulation (hereafter MS; Springel et al., 2005b). Fakhouri & Ma (2008) analysed the MS and found that the dark matter halo merger rate has a nearly universal form that can be separated into its dependencies on mass ratio, descendant mass, and redshift. They presented three algorithms for merger tree construction that result in merger rates differing by $\approx 25\%$. In Genel et al. (2009) (hereafter G09) we introduced a novel merger tree construction algorithm termed as "splitting" (see also Fakhouri & Ma, 2009 and Maller et al., 2006) that incorporates the complicated process of halo fragmentation and re-merging such that a given pair of halos is never considered to merge more than once. This resulted in a different set of parameters for the Fakhouri & Ma (2008) global

fitting formula for the merger rate extracted from our trees of the MS.

Thanks to ever increasing computation power, the dynamic range of N-body simulations increases too. As a result, several recent works have studied the growth rate of dark matter halos. When Stewart et al. (2008) integrated the merger contribution and extrapolated to include *all* unresolved mergers, they found that only $\approx 50\% - 70\%$ of the final mass of halos was assembled by mergers. Rather dissimilar results were found by Madau et al. (2008), who investigated the formation of one halo in a cosmological 'zoom-in' simulation, and by Angulo & White (2010), who investigated the growth of dark matter halos using high-resolution extended Press-Schechter (EPS; Press & Schechter, 1974; Bond et al., 1991; Bower, 1991) trees. These works concluded that the mass accretion of dark matter halos is largely dominated by mergers. In this chapter we perform a similar analysis to that of Stewart et al. (2008) with a larger dynamic range using a combination of the MS and the higher resolution Millennium-II Simulation (hereafter MS2; Boylan-Kolchin et al., 2009), and emphasise the importance of choosing an appropriate merger tree construction algorithm. We show that all resolved mergers contribute $\lesssim 60\%$ to halo mass growth, and suggest that $\approx 40\%$ of the accretion rate may be genuinely smooth. We also provide further support for these results by directly following the histories of dark matter particles in two smaller cosmological boxes, and make detailed comparisons with the previous results mentioned above.

This chapter is organised as follows. In §3.3.1 we review the Millennium Simulations, structure identification and merger-tree construction. In §3.3.2.1 we provide a fitting function that describes the halo merger rate, and in §3.3.2.2 we discuss the contribution of mergers and smooth accretion to halo mass buildup. In §3.3.2.3 we compare our results to the EPS model. In §3.4.1 we describe our direct analysis of dark matter particles histories in two additional simulations, and in §3.4.2 we present the results of that analysis. We discuss implications of our results to galaxy formation in §3.5 and compare our results to previous work in §3.6. We summarise in §3.7.

3.3 Analysis of merger trees

3.3.1 Method

The MS is a cosmological N-body simulation that follows 2160^3 dark matter particles, each of mass $8.6 \times 10^8 h^{-1} M_\odot$, in a periodic box of $500 h^{-1}$ Mpc on a side. The cosmology is Λ CDM with $\Omega_m = 0.25$, $\Omega_\Lambda = 0.75$, $\Omega_b = 0.045$, $h = 0.73$, $n = 1$ and $\sigma_8 = 0.9$. The MS2 uses the same cosmology and follows the same number of particles, but in a box 5 times smaller on a side. Thus, the MS2 particle mass is 125 times smaller, i.e. $6.885 \times 10^6 h^{-1} M_\odot$.

Structure identification in the simulations proceeds in two steps. First, the friends-of-friends (FOF) algorithm (Davis et al., 1985; with a linking length parameter $b = 0.2$) creates at every snapshot a catalogue of FOF groups that are considered to represent dark matter halos. Second, the algorithm SUBFIND (Springel et al., 2001) identifies subhalos inside FOF groups by finding gravitationally self-bound collections of particles around max-

ima in the smoothed density field. The terminology is such that even smooth FOF groups with no identified substructures contain one *subhalo* (often referred to in the literature as the "main" or "background" subhalo) when they are self-bound. Therefore, FOF groups that contain zero subhalos are not gravitationally bound and are subsequently dropped from the analysis. Publicly available subhalo merger trees¹ were constructed by finding a single descendant for each subhalo, a procedure in which the FOF groups themselves played no role. However, if the halo merger rate is to be studied, then different types of merger trees need to be built, in which each node is a halo rather than a subhalo. Such a well-defined halo merger tree can be constructed if each FOF group is given exactly one descendant. In practice, however, choosing the correct descendant is not trivial because FOF groups not only merge, but may also fragment back into several groups.

In most fragmentation events, the subhalo (or group of subhalos) that left its original FOF group becomes a new distinct FOF group. Regardless of whether the two merge back together (as is usually the case) or not, a sequence of a merger followed by a fragmentation introduces artificial effects to the statistics of the merger rate and mass accretion. First, such a sequence of events is recorded as a merger even though the two progenitors end up as two distinct halos at the end of the merger-fragmentation sequence. Thus, the merger rate is overestimated. Second, a mass accretion rate of $M_{\text{small}}/\Delta t$ is attributed to the false merger (M_{small} being the mass of the smaller companion and Δt the time difference between snapshots), thus the contribution of mergers to halo growth is overestimated too. Third, if no "fragmentation rate" is quantified in parallel with the merger rate, all mass changes not associated with mergers are considered "smooth", and so a *negative* contribution of $-M_{\text{small}}/\Delta t$ is added to the smooth accretion component at the time of the fragmentation. Thus, the contribution of smooth accretion to halo growth is underestimated. Additionally, in trees where each halo is allowed to have one descendent at most (the standard case in the literature), the smaller product of the fragmentation has no progenitor, and so its main progenitor track is 'snipped' and all the information of its past formation history is in practice erased.

Therefore, an algorithm that builds fragmentation-free merger trees is needed to quantify correctly both the merger rate and the relative contributions of mergers and smooth accretion to halo mass growth. In G09 we presented such an algorithm and built new trees for the MS. Here we implement this algorithm on the MS2 as well. We construct the trees by splitting certain FOF groups, those that will suffer a fragmentation in the future, into several fragments. All the new fragments that our algorithm creates, as well as untouched FOF groups, are considered hereafter simply as "halos". A unique descendant is found for every halo, so that the merger tree is well defined. More details and motivation for our "splitting" algorithm and comparisons to other algorithms ("snipping", "stitching" and variants, as well as combinations, thereof) are presented in G09 and in Fakhouri & Ma (2009). It is worth noting that already Maller et al. (2006) used a combination of "stitching" and "splitting" methods for their N-body/SPH simulation to obtain

¹Structure catalogues and merger trees were made public by the Virgo Consortium: <http://www.mpa-garching.mpg.de/millennium>.

a fragmentation-free merger tree of galaxies. The halo merger trees we built (for the MS) are available at <http://www.mpe.mpg.de/ir/MillenniumMergerTrees/>.

We derive the merger rate per descendant halo per mass ratio x per unit time $\omega \approx 1.69/D(z)$, which is the natural time variable in the EPS model. Here, $D(z)$ is the linear growth rate of density fluctuations, and ω is estimated using the Neistein & Dekel (2008a) approximation. In our bookkeeping a merger between two halos of masses M_1 and $M_2 \leq M_1$ is recorded as a merger at mass $M_1 + M_2$ with ratio $x = M_1/M_2$. We define the halo mass as the mass of all particles gravitationally bound to it, i.e. the sum of its subhalo masses (see G09 and Fakhouri & Ma, 2010).

3.3.2 Results from the merger trees

3.3.2.1 The merger rate

We find that the merger rates in the MS and MS2 agree very well in the range of overlap ($M \approx 10^{12} - 10^{14} M_\odot$). While the MS2, simulating a smaller volume, has worse statistics in that range, combining it with the MS provides a much larger dynamic range (see below). We fit the merger rate using the fitting formula introduced by Fakhouri & Ma (2008) (albeit with our mass ratio variable $x = 1/\xi$). The new best-fitting parameters we find are only slightly different from those we found for the MS alone in G09. The fitting formula is

$$\frac{1}{N_{\text{desc-halo}}} \frac{dN_{\text{merger}}}{d\omega dx}(x, z, M) = AM_{12}^\alpha x^b \exp((\tilde{x}/x)^\gamma) \quad (3.1)$$

where $M_{12} = M/10^{12} M_\odot$. Our best-fitting parameters for the combination of the two simulations are: $A = 0.065$, $\alpha = 0.15$, $b = -0.3$, $\tilde{x} = 2.5$ and $\gamma = 0.5$ ².

Figure 3.1 shows a few examples of the merger rate for different halo masses and redshifts and the corresponding fits. We find our fit to be appropriate for the whole mass range probed by the simulations at redshifts $0.5 \lesssim z \lesssim 5$. At $z \gtrsim 5$ the redshift and mass dependencies become stronger, and we do not attempt to fit that regime. At $z \lesssim 0.5$ the fit fails due to the proximity to the end of the simulations. That is, the subhalo disruption time at $z \lesssim 0.5$ becomes comparable to the lookback time corresponding to that redshift, thus we cannot identify all the artificially connected halos that would have fragmented had the simulations run past $z = 0$. Figure 3.1 shows that the power-law index b that describes the merger rate at large mass ratios is robustly constrained to be $b \lesssim -0.2$. The important consequences of this finding will be discussed in §3.3.2.2.

The only regime where there is a significant difference between results from the MS and the MS2 is where halos of < 100 particles in the MS are involved. In G09 we used a lower threshold of 40 particles, and found an upturn of the merger rate when the less massive halo had between 40 and ≈ 100 particles. Mergers involving the same halo masses in the MS2 are resolved with many more particles, and no such upturn appears there. This is qualitatively understandable given the finding of Warren et al. (2006) that FOF

²With the mass ratio definition used by Fakhouri & Ma (2008) our parameters correspond, in their notation, to: $A = 0.065$, $\alpha = 0.15$, $\beta = -b - 2 = -1.7$, $\tilde{\xi} = 1/\tilde{x} = 0.4$, $\gamma = 0.5$, $\eta = 1$ and $\bar{M} = 10^{12} M_\odot$.

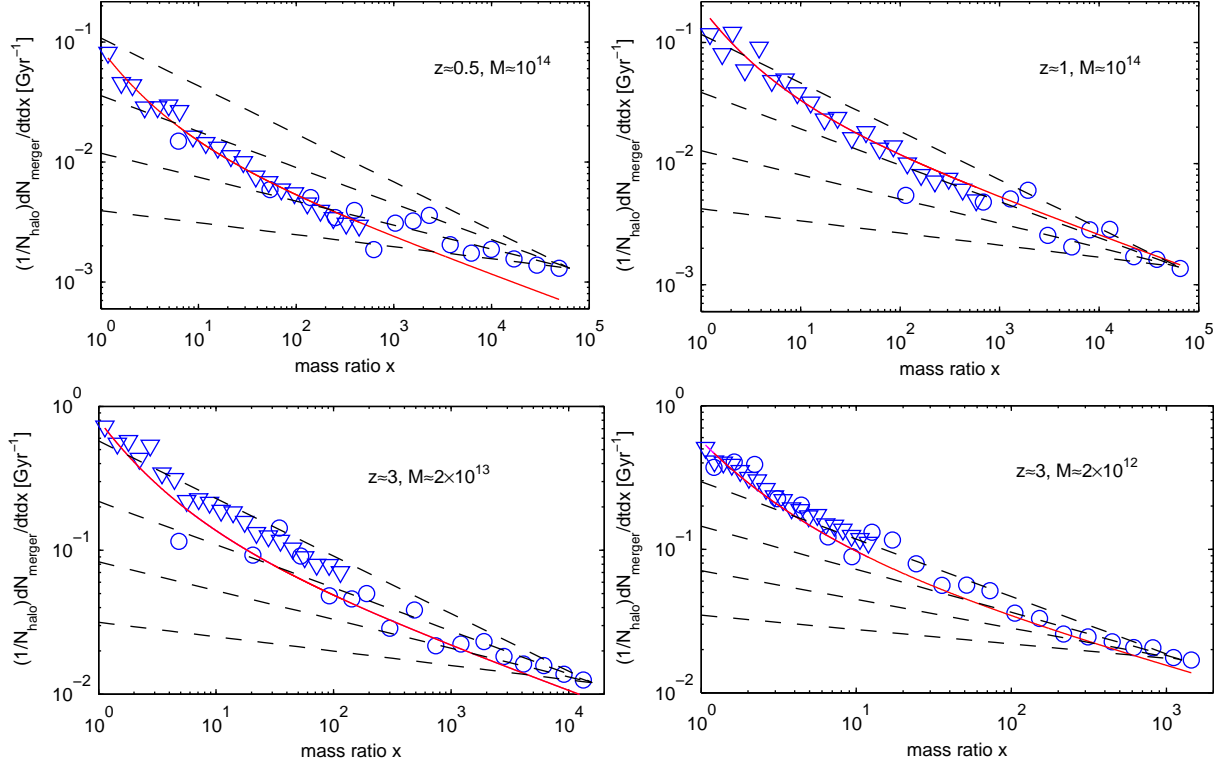


Figure 3.1: The merger rate per unit time from the MS (*triangles*) and the MS2 (*circles*). The different masses and redshifts are indicated in each panel. Our global fit (Equation 3.1), which has an asymptotic power-law index of $b = -0.3$ at high mass ratios, is shown by red solid lines. In each panel constant power-law indices of $\{-0.4, -0.3, -0.2, -0.1\}$ (from top to bottom) are shown by dashed black lines, and demonstrate that $b < -0.2$ is never a good fit to the data at $z \gtrsim 0.5$. At redshifts $z \lesssim 0.5$ our splitting algorithm cannot work properly due to the proximity to the end of the simulation: spurious mergers exist in the trees and the power-law index b increases towards zero. Therefore results for low redshift are not shown here, and were not considered for the global fit.

groups with low particle numbers are overestimated in mass. Hence, combining the two simulations shows that the lower threshold of 40 particles we used in G09 is too low, but that mergers involving two halos of > 100 particles are well resolved. Therefore, we have excluded mergers with halos that consist of less than 100 particles from our global fit. This places a limit for the halo mass of $M \approx 1.2 \times 10^{11} M_{\odot}$ for the MS and $M \approx 9.4 \times 10^8 M_{\odot}$ for the MS2. Given that there are enough statistics for halos of $M \approx 10^{15} M_{\odot}$ in the MS and of $M \approx 10^{14} M_{\odot}$ in the MS2, the largest merger mass ratios we can reliably probe are $\approx 10^4$ with the MS and $\approx 10^5$ with the MS2.

3.3.2.2 Halo growth modes

In the following we investigate the relation between the total mass growth of halos, the relative mass growth due to mergers and the halo merger rate. In Figure 3.2 the solid blue curves show $F(< x)$, the fractional cumulative contribution of mergers to the total instantaneous growth rate of halos. Those contributions are summed up directly from all mergers in our trees. There are six such curves, three from the MS and three from the MS2, for masses spanning the range $10^9 M_{\odot}$ to $10^{14} M_{\odot}$, and averaged over the redshift range $1 < z < 3$ (we find only a weak redshift dependence of $F(< x)$). Each solid curve breaks at some x and becomes horizontal - this is the mass ratio above which mergers cannot be resolved anymore, depending on the mass bin and simulation used³.

The solid blue curves in Figure 3.2 form together a common envelope in the range where mergers are resolved. This envelope shows that $\approx 20\%$ of the total growth rate comes from major mergers ($1 < x < 3$), mergers with $1 < x < 10$ contribute $\approx 30\%$ of the mass growth, all mergers with $1 < x < 100$ contribute only $\approx 45\%$, and the total relative mass contribution of mergers even in the best resolved case, up to a mass ratio of 10^5 , is no more than 60% .

Figure 3.2 also shows the integration of the merger rate obtained by implementing other algorithms for merger tree construction. The black pluses are for the merger rate fitting formula provided by Stewart et al. (2009). Their method results in a converging merger contribution that agrees well with ours⁴, because they pay attention not to double-count mergers. To do that, they use a combination of the "stitching- ∞ " and splitting algorithms (see G09 and Fakhouri & Ma, 2009 for a detailed comparison of the different algorithms). The green symbols are for methods where some fragmentations remain in the trees. These are "snipping" (which is equivalent to not treating fragmentations at all; *circles*) from Fakhouri & Ma (2008), "stitching-3" (*filled circles*) and "splitting-3" from Fakhouri & Ma (2010) (*triangles*), as well as "splitting-3" from Fakhouri et al. (2010) (*filled triangles*).

³Here, as opposed to the case of the merger rate, we do show the contribution of mergers with *all* halos, i.e. down to the resolution limit of 20 particles. While halos with less than 100 particles show an upturn in the merger rate, their influence on the mass contribution is very small, and so we include them in Figure 3.2 in order to show the full contribution of all mergers in the simulation. The very small upturn at the higher mass ratios in some of the blue curves in Figure 3.2 are evidence for this upturn.

⁴The merger rate quantified by Stewart et al. (2009) has some notable differences to ours in its mass ratio and redshift dependencies, but they become much less significant when the fractional cumulative contribution is considered, as in Figure 3.2.

The former two have an asymptotic power-law with $b > 0$, which means that the total merger mass contribution diverges as x increases. The latter two converge, but still show a very different shape from what is obtained from our trees. This does not mean that those methods do not conserve mass. Rather, as mergers with increasing x are resolved, their artificial contribution due to fragmentation, as described in §3.3.1, increases, while the compensation comes in the form of negative contributions from smooth accretion. When mergers with high enough x are resolved, those methods are expected to give negative smooth accretion rates.

The conclusion is that in merger trees that are built so that some fragmentations remain, halo mass assembly must be described by three components: the merger rate, the smooth accretion rate and the fragmentation rate. Otherwise, the interpretation of "anything but mergers" as "smooth" is false. In §3.4 we use a particle-based analysis that is independent of the merger tree construction algorithm to show that the contribution of mergers is consistent with our fragmentation-free "splitting" trees.

The finding that at most⁵ 60% of the growth rate of halos is achieved via mergers with $1 < x < 10^5$ is already remarkable. But what if we had a simulation with an even larger dynamic range? We estimate this by using an extrapolation of the merger rate. The mass growth due to mergers with $x_1 < x < x_2$ is

$$\int_{x_1}^{x_2} \frac{1}{N_{\text{desc-halo}}} \frac{dN_{\text{merger}}}{d\omega dx}(x, z, M) M_{\text{small}} dx, \quad (3.2)$$

where M is the descendant mass and M_{small} is the mass of the less massive progenitor of each merger. Evaluating the integral of the merger rate per descendant halo requires specifying M_{mp}/M , where M_{mp} is the main progenitor mass, since the merger mass ratio is defined such that $M_{\text{small}} = M_{mp}/x$. We approximate M_{mp}/M by $\frac{x}{1+x} \langle M_{mp}/M \rangle$, where $\langle M_{mp}/M \rangle$ is the mean M_{mp}/M computed separately for each M in each of the simulations and averaged over redshift. The dashed red curves in Figure 3.2 show equation (3.2) evaluated between $x_1 = 1$ and $x_2 = x$ and normalised to the total actual growth. There is a very good agreement with the directly extracted fractions. This integration demonstrates that $F(< x)$ converges at $x \gg 1$ to $\approx 60\%$. The convergence can be easily understood, since the merger rate behaves as a power-law with $b = -0.3$ at $x \gg 1$ (see equation (3.1)). Naturally, we cannot be certain that an extrapolation is valid. Yet, for $F(< x)$ to converge to 1, more minor mergers are needed below the resolution limit, such that the asymptotic power-law index would have to be $b \approx -0.01$ at $x \gtrsim 10^5$. Such an index, as we demonstrate in Figure 3.1, is excluded by the data at the currently available resolution ($x \lesssim 10^5$), thus for the fractional mergers contribution to converge to 100%, the power-law index of the merger rate must *change* below our resolution limit.

3.3.2.3 Comparison to the EPS model

Figure 3.3 shows the ratio of the merger rate predicted from the EPS model by Lacey & Cole (1993) (dashed) and Neistein & Dekel (2008a) (solid) to our global fit equation (1) for dif-

⁵Note that $F(< x)$ in Figure 3.2 is averaged over different halos. The *instantaneous* value for individual halos may be very different.

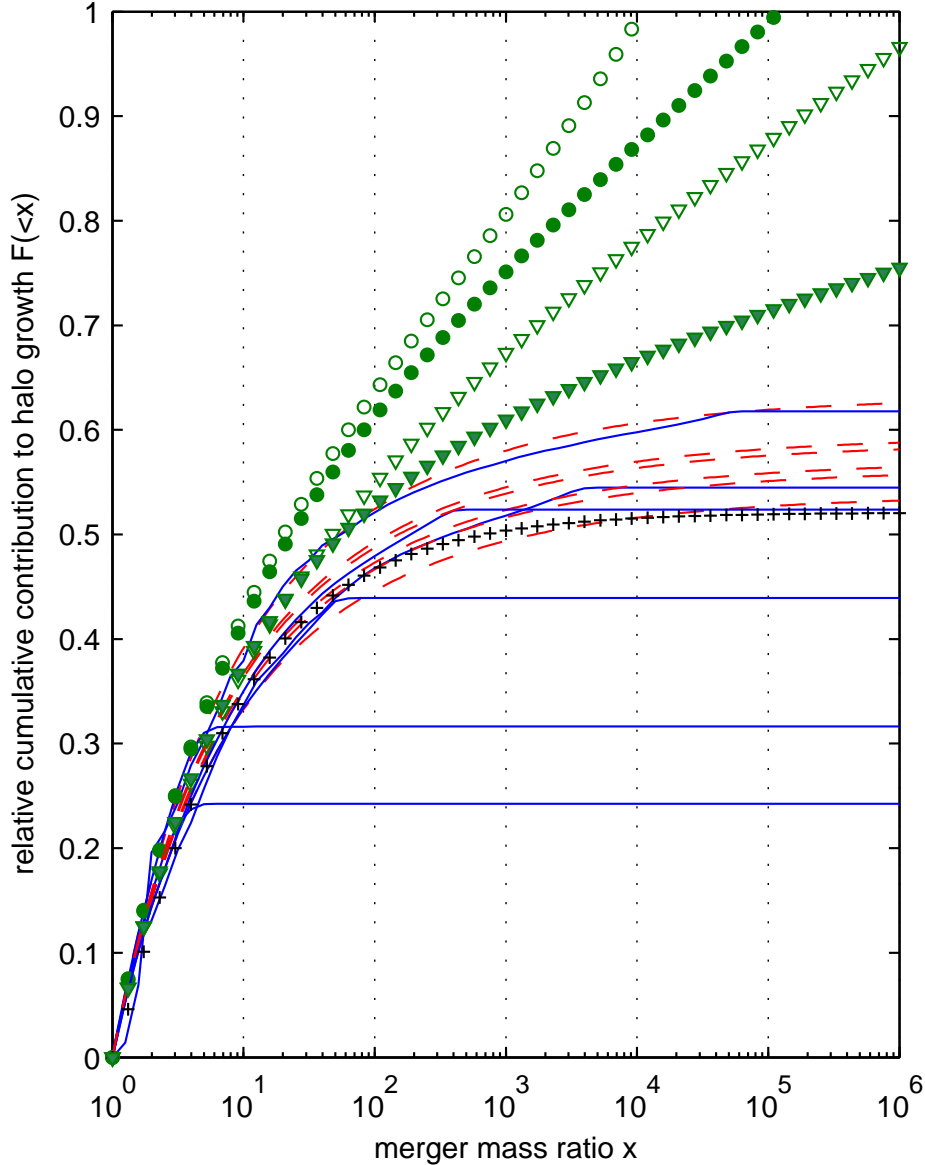


Figure 3.2: The relative contribution of mergers to halo mass growth $F(<x)$ as a cumulative function of mass ratio x . The solid blue curves describe $F(<x)$ for $M \approx 10^{11}, 10^{13}, 10^{14}$ from the MS (going up to mass ratios of 4, 400, 4000, respectively) and $M \approx 10^9, 10^{10}, 10^{13}$ from the MS2 (mass ratios of 5, 50, 50000, respectively). The total contribution of mergers is at most $\approx 60\%$ of the total growth rate of halos. The dashed red curves show the integral of the merger rate (equation (3.2)) using the "splitting" trees and normalising to the total actual growth. The green symbols show the same quantity, for $M \approx 10^{12}$ in the MS, for other merger tree construction algorithms: "snipping" from Fakhouri & Ma (2008) (*circles*), "stitching-3" (*filled circles*) and "splitting-3" from Fakhouri & Ma (2010) (*triangles*), "splitting-3" from Fakhouri et al. (2010) (*filled triangles*), and the combined method of Stewart et al. (2009) (*pluses*).

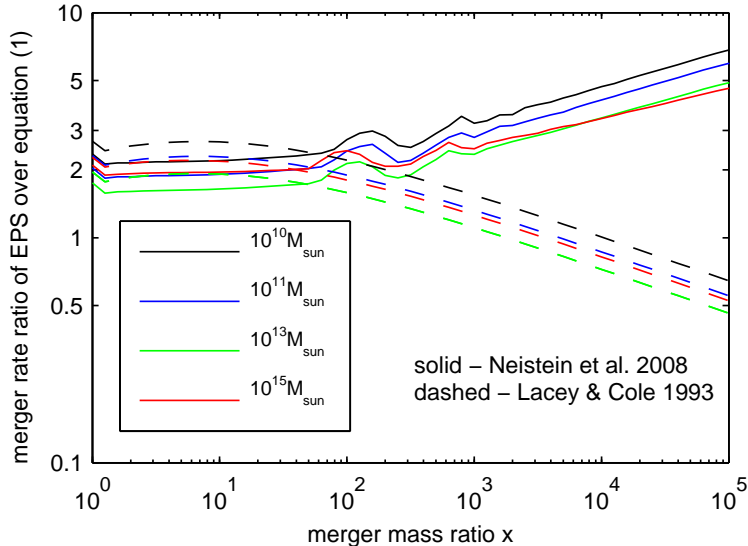


Figure 3.3: The ratio of the merger rate predicted from EPS to our global fit. This ratio is independent of redshift. The EPS merger rate is higher, which roughly compensates for the lack of smooth accretion in the EPS model to give a similar total accretion rate.

ferent masses (and independently of redshift). We identify two regions: at $x \lesssim 100$ the ratio is almost independent of x and ranges from ≈ 1.6 to ≈ 2.3 for different masses, while at $x \gtrsim 100$ the ratio is a power-law. This is because our fit has an asymptotic power-law index $b = -0.3$, while the Neistein & Dekel (2008a) merger rate has a shallower index of -0.16 ± 0.01 and that of Lacey & Cole (1993) a steeper index of -0.5 .

Since most of the merger-contributed accretion rate comes from $x < 100$ (Figure 3.2), and EPS has a $\approx 100\%$ higher merger rate in that regime, the total accretion rate of EPS from $x < 100$ equals almost the actual *total* accretion rate measured in the simulations. Since in the EPS model all the growth comes from mergers by construction (see however Angulo & White (2010)), it seems that the EPS prediction differs from the simulation results in two ways that roughly cancel each other: smooth accretion is lacking, but this is compensated by a boosted merger rate. The higher merger rate found by Neistein & Dekel (2008a) in the $x > 100$ regime boosts their self-consistent EPS total accretion rate further, so that it overestimates the total accretion rate in the simulations by $\approx 35\%$, with weak dependencies on mass and redshift.

3.4 Analysis of particle histories

3.4.1 Method

As much as arguments exist in favour of one or the other algorithm for merger tree construction, some freedom is still left due to the complexity of the hierarchical buildup of cosmic

structures. As the results we presented in §3.3 (specifically Figure 3.2) are algorithm-dependent, it is beneficial to perform an analysis that is independent of such algorithms. Comparing the results of such an analysis to the results from various merger trees can also serve as a tool for distinguishing between the algorithms. In this Section we present an analysis of particle histories that circumvents many of the details involved in building merger trees and just relies on the identification of structure and identification of a ‘main progenitor trunk’ for each halo. This direct particle analysis allows us to get a better handle on the nature of the smooth component.

We perform this analysis on two cosmological N-body simulations. One is the millennial Millennium Simulation that uses the same cosmology and has the same resolution as the MS but includes a factor of 512 less particles in a box of $62.5h^{-1}$ Mpc on a side. The second is the USM Simulation (first presented in Moster et al., 2010) that uses somewhat different cosmological parameters that are in better agreement with current observations ($\Omega_m = 0.26$, $\Omega_\Lambda = 0.74$, $\Omega_b = 0.044$, $h = 0.72$, $n = 0.95$ and $\sigma_8 = 0.77$) and follows particles of mass $2 \times 10^8 h^{-1} M_\odot$ (i.e. 4.3 times smaller than in the MS) in a box $72h^{-1}$ Mpc on a side.

We distinguish between three modes of accretion: ‘merger’, ‘smooth’ and ‘stripped’. In broad terms, we assign any particle accreted as part of a merger event as ‘merger accretion’, while ‘smooth accretion’ is the accretion of particles that never belonged to a bound structure earlier than the accretion event and ‘stripped accretion’ is the accretion of particles that do not arrive as part of a halo at the time of accretion but were part of an identified halo at some earlier time. More precisely, we follow each particle p that belongs to any halo h at any snapshot s_0 to the first snapshot s_{acc} at which it belonged to the main progenitor trunk of halo h . The halo on the main progenitor trunk of halo h at snapshot s_{acc} is termed h_{acc} . Note that, as we discuss below, particles may ‘cycle’ in and out of their halos, i.e. particle p does not necessarily belong to the main trunk of halo h at all snapshots $s_0 > s > s_{\text{acc}}$, but we are interested in the ‘accretion mode’ of p at the very first time it belonged to the main progenitor trunk of h . We then look for particle p in snapshot $s_{\text{acc}} - 1$, and tag it according to the following criteria. If p at $s_{\text{acc}} - 1$ belongs to a progenitor halo of h_{acc} , it is tagged as ‘merger accretion’. If it belongs to a halo that is not a progenitor of h_{acc} , it is tagged as ‘stripped accretion’. If p belongs to no halo at $s_{\text{acc}} - 1$, we follow it back through every snapshot to the initial conditions. If we find some earlier snapshot $s < s_{\text{acc}} - 1$ where p belonged to a halo, we also tag it as ‘stripped accretion’, otherwise it is tagged ‘smooth accretion’.

Further on we tag some particles as ‘leaving’ or ‘joining’ their halo. ‘Leaving’ particles are those that are not part of the halo’s direct descendant (at snapshot $s = s_0 + 1$). ‘Joining’ particles are those that did not belong to the halo’s direct main progenitor (at $s = s_0 - 1$). The net growth rate of each halo is then given by $N_{\text{join}} - N_{\text{leave}}$. Since we also know the original accretion mode of each particle onto the halo, we can quantify the contribution of each mode to the total net growth rate.

It is important to discuss to what extent the results from this analysis are expected to be independent of the merger tree on which the analysis is based. Let us examine the consequences of a fragmentation in the merger tree. The more massive halo of the pair, the

one for which the main progenitor trunk remains intact, will be insensitive to whether the fragmentation is cured by splitting the spuriously-connected halo or not. This is because a fragmentation event of a subhalo (that previously arrived in a merger) will appear as 'leaving' particles tagged as 'merger mode' and therefore on average will cancel out the same particles when they were 'joining'. On the other hand, implications do exist for the other halo of the pair, i.e. the smaller 'fragment', if the fragmentation is left in the tree. The small fragment has no progenitor and so its main progenitor trunk is cut and therefore the memory of its particles as for their true origin is erased. After the fragmentation they will all be classified as 'stripped', because they belong to a halo that is not the fragment's progenitor just prior to its 'appearance' as an independent halo. Therefore, we expect an artificial overestimate of 'stripped' particles if fragmentations are left in the tree, at the expense of both other accretion modes. We show and discuss this effect further in Section 3.4.2.

3.4.2 Results from the analysis of particles

Figure 3.4 shows the fractional mass content of $z = 0$ halos in the milli-Millennium Simulation separated into the three modes by which each of their particles was accreted onto them, as indicated in the legend. The dots are for different halos and demonstrate the distribution around the mean values, which are shown by curves with open circles. We see (*green*) that almost all halos are made mostly of particles that never belonged earlier to other halos. Plotted on top (*bottom black*) are results from the analysis of the merger trees, which are obtained by summing up all the mass accreted via mergers along a halo's main progenitor trunk. An important point to take from Figure 3.4 is the agreement between the two analysis methods, shown by the red and bottom black curves. The small difference between the two is expected because some particles that arrive via mergers later leave the halo and do not contribute to its mass at $z = 0$ (see also below).

The trend seen in Figure 3.4 is clearly an effect of resolution: halos closer to the resolution limit have gained most of their mass by unresolved accretion, which cannot be distinguished between the different components and this mass is identified as 'smooth'. Nevertheless, the beginning of a saturation of the mass fraction arriving from mergers is apparent as halos are better resolved. We suggest that the 'true' value for all halos is the saturated value that is seen for high-mass halos. Additional evidence for the trend being an effect of resolution is the fact that for the same halo mass, the MS2 halos, which are better resolved, show a weaker trend (*top black*) than the results from the MS (*bottom black*). We do not have enough statistics to quantitatively constrain the saturation of this quantity due to low halo numbers at high masses, but these results are consistent with our results on the accretion rate (see below), where the saturation is statistically robust (§3.3.2.2).

In Figure 3.5 we show the main result of the particle analysis, the fraction of the net instantaneous accretion that is associated with the three different modes, as a function of halo mass and redshift. We observe no dependence on redshift, even down to $z = 0$, despite the inflated merger rate that is due to the proximity to the end of the simulation.

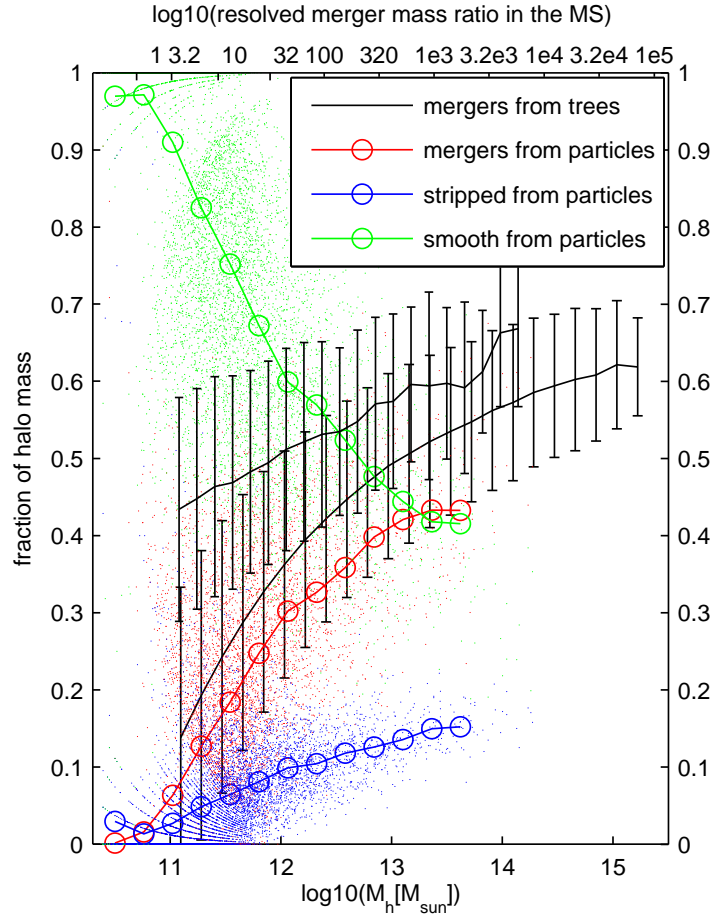


Figure 3.4: The fraction of the particles in $z = 0$ halos originating from the three accretion modes: 'merger' (*red*), 'stripped' (*blue*) and 'smooth' (*green*), versus halo mass. The dots are for different halos and demonstrate the distribution around the mean values, which are shown by curves with open circles. Overplotted are corresponding curves from the analysis of the merger trees of the MS (*lower black curve*) and MS2 (*upper black curve*), which indicate the total mass accreted via mergers onto the main progenitor trunk normalised to the $z = 0$ halo mass. The error bars include 68% of the halos around the mean (see McBride et al., 2009 for a more detailed description of the distribution around the mean for major mergers). The MS curve from the merger trees is similar, yet slightly higher, than the 'merger' component from the particle analysis. This is expected since some particles that arrive via mergers leave (smoothly) and never come back, which is information that is not included in the merger trees alone. The MS2 curve is significantly higher where MS halos are barely resolved and MS2 halos are well resolved, but the difference between the two curves decreases towards higher halo masses, as expected. Note that the mass content of halos is only slightly affected by the proximity to the end of the simulation and the inability to split some subhalos out. This is because the mass ratio regime that is mostly affected by this effect is subdominant in mass contribution.

This means that even if some of the increase of the minor merger rate at $z \lesssim 0.5$ is *real*, it is not high enough to make a significant contribution to the total mass accretion (see also Figure 3.9 below). The mass dependence is again a resolution effect. As halos are better resolved, the mergers they undergo are better resolved and so the contribution of the ‘merger’ component increases. Although we again cannot make a robust fit and extrapolation from these results, we find it reassuring that the particle analysis gives a consistent result with that of the “splitting” merger trees (*dashed black curves*, which cover the range of the dashed curves in Figure 3.2).

It is worth noting that the curves in Figure 3.4 are shifted from those in Figure 3.5 by $\approx 0.5 - 1$ dex toward higher masses. This is expected, as halos accrete most of their final mass $M_{z=0}$, by definition, when $M_z \gtrsim 0.1M_{z=0}$. This means that the fractions of the different accretion modes in the final halo mass $M_{z=0}$ (Figure 3.4) correspond to their fractions in the accretion at $M \gtrsim 0.1M_{z=0}$ (Figure 3.5).

3.4.3 The cycle of particles in and out of halos

From Figures 3.4 and 3.5 we can also learn that the fraction of the accretion in the ‘stripped’ mode is subdominant to that in the ‘smooth’ mode. That is, what we could only interpret as ‘non-mergers’ from the analysis of the merger trees, can now be shown to consist of particles that never belonged to another halo prior to their accretion. In fact, the ‘stripped’ mass is consistently $\approx 1/3$ of the mass in the ‘merger’ mode. Conservatively, the ‘stripped’ component is our uncertainty, because our analysis does not indicate how long it has been stripped and what part of it comes from the vicinity of approaching subhalos. Indeed, some of these ‘stripped’ particles arrive as mergers into low-mass halos and after being stripped from them, are re-accreted into more massive halos and tagged there as ‘stripped’. Thus, some of the mass appearing in the merger trees as ‘merger mode’ is transferred into ‘stripped mode’ of more massive halos in the particle analysis. This is the reason the red curves are somewhat lower than the black dashed ones.

We can learn more about this ‘cycle’ of particles through different halos from Figure 3.6. There it is shown that the rate at which particles join and leave their halo is similar to, or even higher than, the *net* growth rate, for each of the different modes. As a quantitative example, shown in Figure 3.6, the rate of ‘smooth’ particles joining their halos at $z \approx 0$ is ≈ 4 times higher than the net growth rate due to smooth accretion, i.e. only $\approx 33\%$ higher than the ‘leaving’ rate of particles that previously arrived smoothly. These numbers drop toward higher redshift, where the ‘cycle’ is less significant, e.g. at $z \approx 2$ the values are lower roughly by a factor of 2 compared to those shown in Figure 3.6. Note that all ‘leaving’ particles leave their halos smoothly, i.e. not as part of a bound subhalo, as such events have already been cleaned at the time of merger tree construction. Thus the red curve in Figure 3.6 shows that there are many particles that arrive via mergers and then stripped off of their subhalos inside the main halos and later leave the main halo ‘smoothly’. It seems reasonable to suggest that this cycle is driven, at least partly, by fluctuations of particles that reside close to the halo boundary in and out of the region defined as the halo by the FOF algorithm. This is the reason we focus throughout the chapter on the net growth

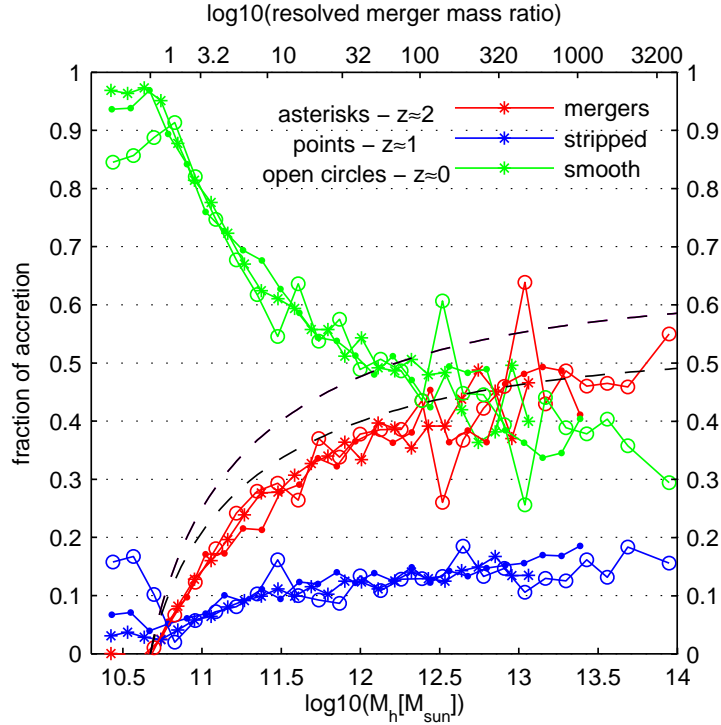


Figure 3.5: The fraction of net accretion (i.e. ‘joining’ particles minus ‘leaving’ particles), as a function of halo mass, that belongs to each of the three modes ‘merger’ (*red*), ‘stripped’ (*blue*) and ‘smooth’ (*green*). The results are shown for three different redshifts and are independent of it. As higher mass ratios are resolved, more of the accretion is in the ‘merger’ and ‘stripped’ modes, but the merger mode contribution is consistent with the saturation inferred from the merger trees (shown by the dashed black curves that cover the range of the dashed curves in Figure 3.2). This indicates that the contribution of mergers may not increase further.

rate. We leave a more detailed study of this cycle to future work.

3.4.4 Alternative trees and halo definitions

In Figure 3.7 we compare the merger contribution to the accretion rate from our “splitting” and “snipping” (Fakhouri & Ma, 2008) trees. The “snipping” algorithm is the most extreme case of leaving all fragmentations in the trees so that in the merger tree analysis the merger contribution does not converge (*pluses*, same as in Figure 3.2). In contrast, the “snipping” merger contribution does not exceed 60% when the *particle histories* are used (*dashed*). In fact, it is somewhat lower than in the “splitting” case (*solid, asterisks*) because, as we describe in §3.4.1, the role of ‘stripped’ particles is overestimated at the expense of the other accretion modes. This is because the particles of ‘snipped’ halos, which

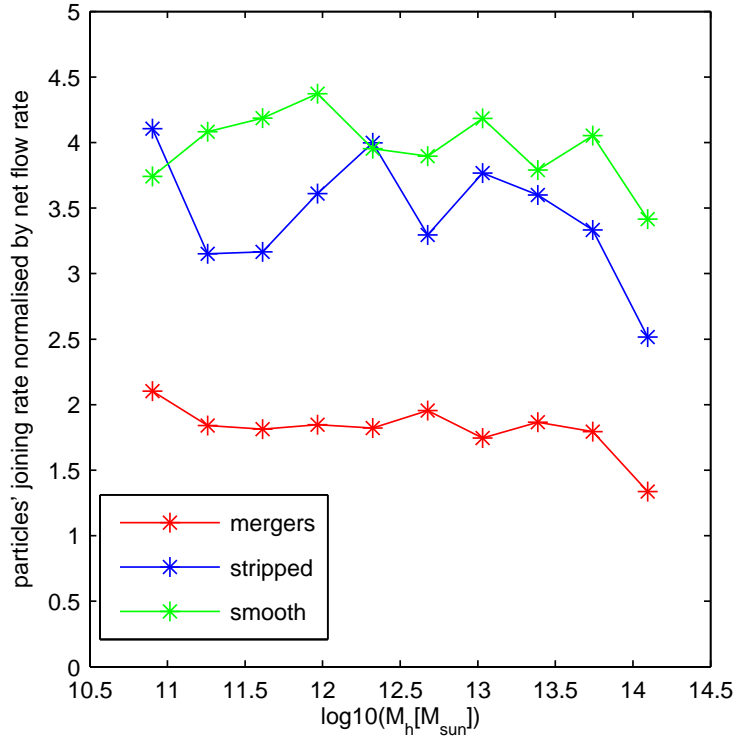


Figure 3.6: The $z = 0$ cycle of ‘joining’ and ‘leaving’ particles, shown by the ratio of the gross inflow rate (‘joining’ particles) to the net growth rate (‘joining’ minus ‘leaving’). Both the gross and net rates are calculated separately for each accretion mode, which are shown by the different curves in indicated in the legend. The most striking result here is that both the gross mass gain and the gross mass loss are comparable to, or even larger than, the *net* halo growth rate.

lose their main progenitor trunks, are tagged ‘stripped’ instead of their original accretion modes. To verify this we divide the ‘stripped’ particles into two categories: ‘just stripped’ and ‘stripped in the past’. The former category includes particles that at $s_{\text{acc}} - 1$ belong to a halo that is not a progenitor of h_{acc} , and the latter category includes particles that were found to belong to a halo at an earlier time in the past. We find that ‘just stripped’ particles are negligible in the “splitting” trees but they become very significant, especially for low mass halos, in the “snipping” trees, because the particles of a ‘snipped’ halo h_{acc} are identified at $s_{\text{acc}} - 1$ in the artificially-connected FOF group, which is not a progenitor of h_{acc} . Hence, we see that the results of the analysis we present in this Section are not entirely merger tree-independent. The results for trees with remaining fragmentations are different depending on the analysis method (merger tree only or particle history analysis) and both suffer from artificial effects because the trees are not self-consistent. On the other hand, the analyses based on the “splitting” trees are consistent with each other (as already shown in Figure 3.5).

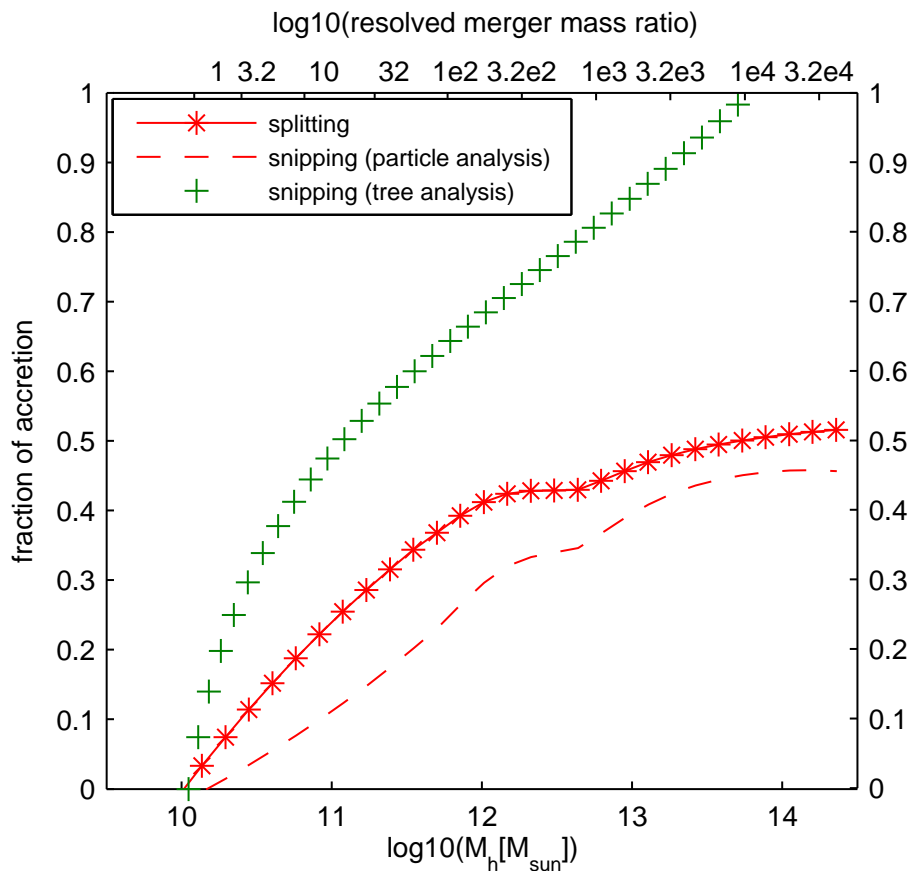


Figure 3.7: Comparison of the contribution of the different accretion modes at $z = 0.3$ in the "splitting" and "snipping" trees from the USM simulation. In the "snipping" trees (*dashed*) the contribution of mergers is *not* higher than in the "splitting" trees (*solid, asterisks*), unlike the results of the merger tree analysis (*pluses*, same as in Figure 3.2). This demonstrates that merger trees with fragmentation events are not appropriate for studying halo growth modes, as they are not self-consistent. In fact, in the particle analysis the "snipping" merger contribution is somewhat lower than the "splitting" merger contribution due to an artificial effect caused by the snipping of the main progenitor trunk, see details in the text. For the "splitting" trees, there is very good agreement between the USM simulation (*solid, asterisks*) and the milli-Millennium Simulation (Figure 3.5).

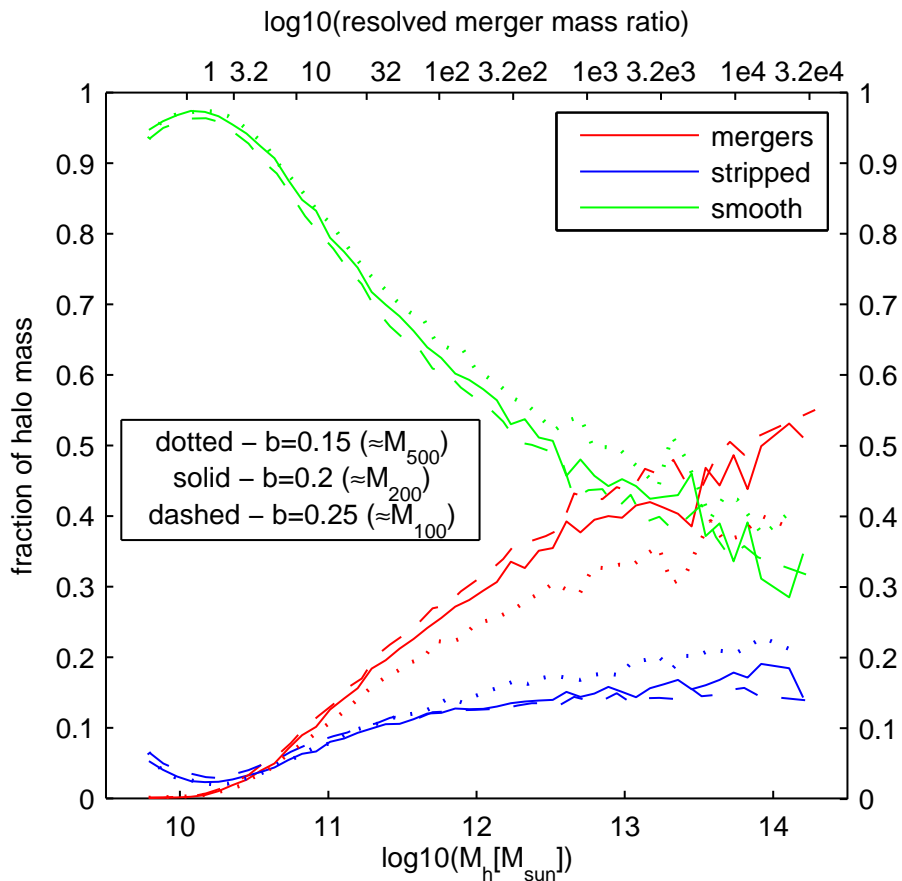


Figure 3.8: The contribution of the different halo growth modes to the $z = 0.3$ halo mass from the USM simulation. The results with the standard FOF group finder (*solid*) agree very well with the results from the milli-Millennium Simulation (Figure 3.4). The results based on different halo definitions (FOF groups with $b = 0.25$, *dashed* and with $b = 0.15$, *dotted*) are also virtually unchanged.

Finally we explore the sensitivity of our results to the halo definition by repeating our analysis with a different definition for a halo. The first step of structure identification, the FOF group finder, is run with different linking lengths of $b = 0.25$ ($b = 0.15$), corresponding approximately to structures with overdensities of 100 (500) rather than 200. This results in FOF groups that are on average $\approx 15\%$ more ($\approx 25\%$ less) massive. We then run SUBFIND and our splitting algorithm as before. The halos in our final catalogues are also more (less) massive compared with our original catalogues by similar factors. This is because SUBFIND is run on each FOF group separately and is restricted to working on particles within FOF groups only⁶. Figure 3.8 shows the contribution of the different accretion modes to the halo mass at $z \approx 0.3$ from the USM simulation for the three different FOF group definitions. The results agree very well with each other and with the results presented above from the Millennium Simulations. This agreement reflects the fact that the change of halo definition is roughly mass independent (Jenkins et al., 2001; White, 2002), and so both the merger mass contribution and the total halo mass change in a similar way. It then follows that the smooth accretion mass contribution increases by the same factor and the relative contributions do not change. Note, however, that using a mass definition that changes the mass of halos as a function of mass (e.g. Cuesta et al., 2008) could lead to different results. For example, Warren et al. (2006) suggested a correction to FOF group masses that reduces the mass of poorly resolved (low mass) FOF groups, an effect that would work in the direction of an even higher contribution from smooth accretion.

There exist a few alternatives to the FOF algorithm for identifying dark matter halos. In this chapter we use only the FOF algorithm (with different linking lengths, as described above), but we believe that other halo definitions will not change the main results. One supporting evidence for that is the work of Stewart et al. (2008), who used the 'bound density maxima' algorithm (Klypin et al., 1999) for halo identification, and found results that agree well with ours. Another alternative would be to use 'spherical overdensity' halos, i.e. defining the spherical region inside the virial radius as the halo. Unless FOF groups are organised in a way that the smoothly accreted mass is outside the virial radius and the merger accreted mass is inside, significant deviations from our results should not arise. The case is probably the opposite, because when FOF groups have very aspherical shapes it is mainly because a few substructures are connected together, i.e. it is not that the outskirts of FOF groups constitute mainly of smoothly accreted material.

3.5 Implications for galaxy formation

Many theoretical models focus on the role of major mergers in galaxy evolution. In this chapter we have shown that it is actually minor mergers ($x > 10$) and smooth accretion that dominate halo growth by accounting for $\approx 70\%$ of the accretion rate onto halos. Therefore, halos grow mainly continuously rather than in bursts with short duty cycles. This mode of

⁶In the $b = 0.25$ case, where particles have been *added* to the FOF groups compared with the $b = 0.2$ case, they are typically infalling onto their halos, i.e. they have negative energies relative to the halo centers and are therefore considered bound by SUBFIND and included in the new halo catalogues.

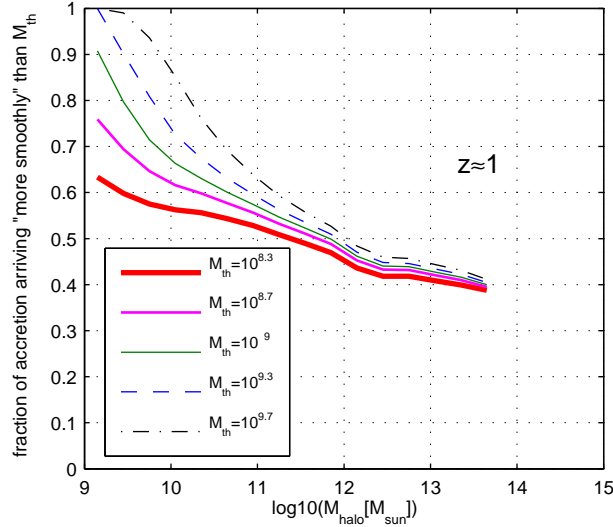
accretion is more favourable for disk formation at all redshifts, and may in particular help in understanding galaxies at high redshift that show extreme star-formation rates but no signs of major mergers (e.g. Genzel et al., 2008; Genel et al., 2008; Förster Schreiber et al., 2009).

If there is a truly smooth accretion component, simulations from cosmological initial conditions naturally include it. Indeed, our result is consistent with hydrodynamical simulations that show that most baryonic accretion onto galaxies does not arrive in the form of mergers (Murali et al., 2002; Semelin & Combes, 2005; Maller et al., 2006; Dekel et al., 2009a). Our findings suggest that as the resolution of future simulations increases, the mass contribution of small halos to the formation of galaxy-size halos will hardly increase further. This implies that $\approx 40\%$ is a strong lower-limit on the mean fraction of pristine intergalactic medium (IGM) gas in the baryons accreted onto halos of any given mass or redshift, since this smooth gas was never bound to any subhalos and is therefore not expected to have formed stars or to have become significantly enriched with metals, regardless of the star-formation efficiency and history of the baryons in the merging halos. It may also be expected that this $\approx 40\%$ did not experience feedback from star-formation in smaller halos, and is likely "cold" when finally accreted onto a halo, with $T \gtrsim 10^4\text{K}$ set by photoheating of IGM gas.

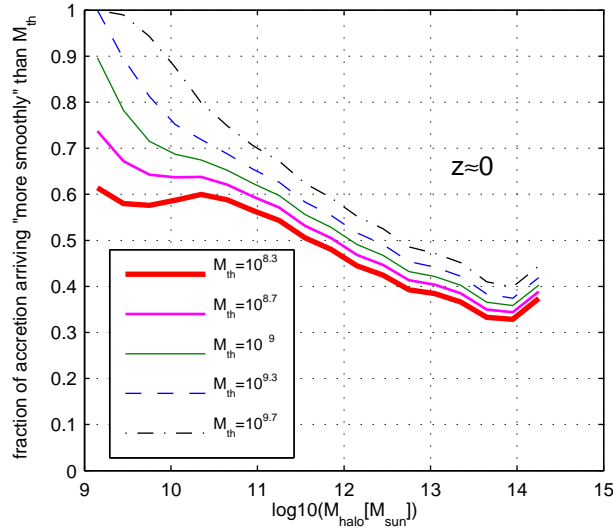
In the context of the "cold flow" mode of gas accretion onto galaxies (Birnboim & Dekel, 2003; Dekel & Birnboim, 2006; Kereš et al., 2005), our results suggest that roughly half of the incoming gas is not clumpy, thus processes like tidal stripping and dynamical friction are irrelevant for it⁷. Theoretical or semi-analytical galaxy formation models, for example EPS-based models, may benefit from taking the smooth accretion component into account, as many properties of galaxies, such as size and morphology, depend on the way they accrete their baryons.

Even if an extrapolation of the power-law index of the merger rate beyond $x = 10^5$ is not valid and mergers of higher mass ratios do make up for the "missing" $\approx 40\%$, our results are still significant. Since the MS2 resolves all halos with $T_{vir} > 10^4\text{K}$ at $z \lesssim 3$ ($M \gtrsim 1.9 \times 10^8 M_\odot$), we do resolve most of the accretion of halos that have experienced star-formation, that is if star-formation is prohibited in halos with $T_{vir} < 10^4\text{K}$ (e.g. Rees, 1986; Efstathiou, 1992; Okamoto & Frenk, 2009; Hoeft & Gottloeber, 2010). Current models of galaxy formation derive, assume or require strong suppression of cooling and/or star-formation below a virial temperature threshold that is even higher than 10^4K (e.g. Bouché et al., 2010; Kravtsov, 2010, and references therein). The fraction of the mass that arrives either smoothly or by accretion of small halos can be read off Figure 3.2 as the complement of the merger contribution. However, for the convenience of the reader we explicitly show in Figure 3.9 the fraction of accretion that arrives smoothly, for different values of a threshold mass below which accretion of *baryons* is assumed smooth. The results shown in Figure 3.9 do not depend on any extrapolation but are based directly

⁷Although it is possible that the gas becomes clumpy inside the halo on its way to the galaxy due to different instabilities (e.g. Field, 1965; Burkert & Lin, 2000; Maller & Bullock, 2004; Kereš & Hernquist, 2009; Birnboim, 2009).



(a)



(b)

Figure 3.9: The fraction of mass accretion that arrives "more smoothly than" M_{th} , i.e. by accretion of halos with $M < M_{th}$ plus smooth accretion. This fraction is shown as a function of halo mass, and for different values of M_{th} . These results are from the MS2 and are based directly on the merger trees, without using the fitting formula Equation 3.1 or any extrapolation below the simulation's resolution limit. The results are plotted for accretion at $z \approx 1$ (top) and $z \approx 0$ (bottom). The resemblance of the $z \approx 0$ results to those at $z \approx 1$ highlights the fact that despite of an overestimation of the minor merger rate at $z \lesssim 0.5$ in the "splitting" trees, the contribution of minor mergers to the total mass growth is still very small.

on the MS2 (since all M_{th} we use are resolved by the MS2). For example, by assuming that pre-heating from the cosmic UV background evaporates halos below $M_{th} \approx 10^9 M_\odot$ (*green*), we infer that $10^{11} M_\odot$ halos at $z \approx 1$ ($z \approx 0$) accrete $\approx 55\%$ ($\approx 65\%$) of their baryonic mass in smooth $T \gtrsim 10^4 \text{K}$ gas. Since $10^{11} M_\odot$ halos do not form a stable virial shock and the cooling times are short, over-efficient galaxy formation in such halos is probably prevented by strong baryonic feedback processes.

3.6 Comparison to previous work

Merger trees are regularly treated in the literature such that each node (whether a halo or a subhalo) never has more than one descendant. This constraint is motivated by the idea of hierarchical buildup of structure, but in practice, when standard halo definitions are used, fragmentation events are common too. To treat the formation of dark matter halos self-consistently, there are two alternatives. First is to allow for more than one descendant and consequently quantify both the merger rate and the fragmentation rate. Alternatively, the trees may be rearranged so that fragmentations do not exist. In this chapter we use a variant of the second possibility, namely our "splitting" algorithm⁸. Our result agrees with that of Stewart et al. (2008) and Stewart et al. (2009), as described in §3.3.2.2, since they use fragmentation-free merger trees, but disagrees with the results of Fakhouri & Ma (2008) and Fakhouri & Ma (2009), who do not.

Recently Fakhouri & Ma (2010) found that the relative importance of mergers to the growth of halos in the MS correlates with large-scale environment. This, as they suggest, is further compelling evidence for the true diffuse nature of non-merger halo growth, even if the quantitative proportions they find from their trees differ from ours.

Guo & White (2008) investigated the relative growth of FOF groups in the MS via major mergers, minor mergers and 'diffused particles'. Their main findings that are different from our results are: (i) at large enough masses ($M \gtrsim 3 \times 10^{12} M_\odot$) merger accretion dominates over smooth accretion, (ii) the relative role of merger accretion, for a given mass, is larger at lower redshifts. Both differences occur because Guo & White (2008) consider "unprocessed" FOF groups, i.e. implicitly use 'snipping' trees. They consider only instantaneous mass gain due to mergers but not instantaneous mass loss due to fragmentations, which becomes more important at low redshift and for high mass (better resolved) halos.

Angulo & White (2010) studied halo formation histories in the framework of EPS assuming a finite dark matter particle mass. They found that if the dark matter particle is assumed to be a 100 GeV neutralino then Milky Way type halos are expected to have $\approx 10\%$ smooth accretion, which is due to a minimum halo mass imposed by the free streaming of the dark matter particles. They compare their results to an N-body simulation, and find that up to a mass ratio $x = 500$ the contribution of mergers is $\approx 45\%$, in good agreement with our results. For the same mass ratio, they find the spherical collapse EPS model to give $\approx 70\%$ accretion from mergers, in rough agreement with our results as well. The

⁸In G09 we found that there is a good physical basis for our specific choice of a "splitting" algorithm, since fragmentations usually occur before the halos have had significant dynamical interaction.

significant contribution they find for mergers with $x > 500$ ($\approx 25\%$ in the spherical collapse model) is due to the higher power-law index of the merger rate in EPS, as shown here in Figure 3.3. If instead the power-law index appropriate for very large x is the one we find from the resolved regime in the Millennium Simulations, the contribution of mergers to halo growth practically vanishes even before reaching the free streaming mass.

Madau et al. (2008) report that less than 3% of the final mass of the Via Lactea halo, which is a Milky Way-type halo simulated at high resolution, was accreted smoothly. This appears to stand in sharp contrast with our results, and there are a few possible explanations for this disagreement.

- We do find Milky Way-type halos that have $< 3\%$ of smooth accretion, but they are only approximately one in a thousand halos. It could then be that the Via Lactea halo is an untypical halo ($\approx 3\sigma$) in this respect. This is a possible but undesired ‘last resort’ explanation, which we do not need to invoke, given the more likely explanation below.
- It could be that the higher resolution available for the Via Lactea halo is responsible for the difference. We suggest that this is *not* the dominant reason for the difference based on the following argument. It can be read from Figure 4 in Madau et al. (2008) that halos of peak velocity ratio < 45 have contributed to the Via Lactea halo 97% of its final mass, which is all of the accretion that is associated with mergers. Such velocity ratios correspond approximately to mass ratios $x < 45^3 \approx 10^5$, which can also be resolved for the most massive halos in the MS2. In other words, it seems that these are not the higher resolution mergers in the Via Lactea halo that contribute the “additional” (when compared with our results) $\approx 37\%$ mass, but rather mergers that we *are* able to resolve. Moreover, we can consider just the *total* fraction reported by Madau et al. (2008). The maximal mass ratio resolved by the Via Lactea simulation is $x \approx 5 \times 10^6$, and our best resolved mass ratio is $x \approx 10^5$. For this range $10^5 < x < 5 \times 10^6$ to account for $\approx 97\% - 60\% = 37\%$ of the mass accretion, the power-law index of the merger rate would have to be $b \approx 1.5$ at $10^5 < x < 5 \times 10^6$. Compared with the value $b \approx -0.3$ we find at $x < 10^5$, this is an unlikely abrupt change.
- We believe the most probable explanation is that differences in analysis methods cause the results to be so different. Madau et al. (2008) sum up all the *peak* masses (over their full formation histories) of all halos that have merged into the main progenitor trunk and compare it to the mass inside r_{200} at $z = 0$. They do not account for the fact that some fraction of the mass of the merged subhalos ends up outside of r_{200} at $z = 0$, and so they overestimate the mass contribution of mergers.

To understand this issue with greater certainty, other high resolution simulations of individual halos should be further examined. To this end, Wang et al. (2010) analyse the high resolution Aquarius halos (Springel et al., 2008) with a method close to the one we use in §3.4 and find results that are more consistent with ours than with those of Madau et al. (2008).

3.7 Summary

In this chapter we calculate the merger rates of dark matter halos and we investigate the role of smooth accretion versus mergers to their growth. We extract the merger rates and accretion histories from the Millennium and Millennium-II Simulations, combined with two additional, smaller, cosmological simulations. We use the "splitting" merger tree construction algorithm described in §3.3.1 and in G09, and verify its reliability by reproducing our results by following individual particle histories alone, independent of merger tree construction algorithms.

We find that the contributions of all resolved mergers (up to mass ratios $\approx 10^5$) to the total growth rate of halos do not exceed 60%, regardless of halo mass and redshift. Most of the *merger* contribution comes from small mass ratio ("major") mergers (e.g. $1 < x < 10$ contribute $\approx 30\%$ of the total growth), while "very minor" mergers add very little mass (e.g. $10^3 < x < 10^5$ contribute just a few percent to the total halo growth). We find that the power-law index of the merger rate is such that if the merger rate is extrapolated beyond the maximum resolved mass ratio $\approx 10^5$, the total contribution of *all* mergers saturates at $\approx 60\%$. This suggests that a significant mass fraction of halos may be accreted in a genuinely smooth way.

Our results have important implications for galaxy formation models and the modes of baryonic accretion. If $\approx 40\%$ of the dark matter that is accreted onto a halo was never previously bound in any merging smaller halos, then at least $\approx 40\%$ of the baryons must also be accreted smoothly - as gas that was never previously heated by feedback processes or converted to stars. For the baryons, this $\approx 40\%$ is a strong lower limit since halos with $T_{vir} < 10^4\text{K}$ likely cannot retain their gas. The common assumption that halos with $T_{vir} < 10^4\text{K}$ cannot retain their gas also makes our results insensitive to the limited resolution of the simulations we use, because we resolve all halos above this limit (at $z \lesssim 3$). The implication is that a very large fraction of the baryonic matter falling into a halo must be pristine "cold" IGM gas, with $T \gtrsim 10^4\text{K}$ set by IGM photoheating. This gas is not expected to have formed stars or to have become significantly enriched with metals, no matter what the star-formation efficiency and history of the baryons in any of the merging halos.

Chapter 4

The Millennium Simulation Compared to $z \approx 2$ Galaxies

Note: This chapter has been published in Genel et al. (2008).

4.1 Abstract

Recent observations of UV-/optically selected, massive star forming galaxies at $z \approx 2$ indicate that the baryonic mass assembly and star formation history is dominated by continuous rapid accretion of gas and internal secular evolution, rather than by major mergers. We use the Millennium Simulation to build new halo merger trees, and extract halo merger fractions and mass accretion rates. We find that even for halos not undergoing major mergers the mass accretion rates are plausibly sufficient to account for the high star formation rates observed in $z \approx 2$ disks. On the other hand, the fraction of major mergers in the Millennium Simulation is sufficient to account for the number counts of submillimeter galaxies (SMGs), in support of observational evidence that these are major mergers. When following the fate of these two populations in the Millennium Simulation to $z = 0$, we find that subsequent mergers are not frequent enough to convert all $z \approx 2$ turbulent disks into elliptical galaxies at $z = 0$. Similarly, mergers cannot transform the compact SMGs/red sequence galaxies at $z \approx 2$ into observed massive cluster ellipticals at $z = 0$. We argue therefore, that secular and internal evolution must play an important role in the evolution of a significant fraction of $z \approx 2$ UV-/optically and submillimeter selected galaxy populations.

4.2 Introduction

In the cold dark matter model of hierarchical structure formation (Blumenthal et al., 1984; Davis et al., 1985; Springel et al., 2006) mergers are believed to play an important role in galaxy formation and evolution (Steinmetz & Navarro, 2002). Mergers induce starbursts (Hernquist & Mihos, 1995) and transform galactic morphology (Naab & Burkert, 2003).

Major mergers may drive the buildup of the red sequence (Toomre, 1977; Hopkins et al., 2008a). Dark matter models and many observations show that mergers are more frequent at high redshift (Fakhouri & Ma, 2008; Conselice, 2003).

However, there is growing evidence that a smoother growth mode may be important for the baryonic mass assembly and star formation history at high redshift. For example, the tight correlation between star formation rate (SFR) and stellar mass in UV-/optically selected star forming galaxies is indicative of buildup by continuous gas inflow (Daddi et al., 2007; Noeske et al., 2007). As part of the SINS survey (Förster Schreiber et al., 2006, 2009), integral field spectroscopy of more than 50 UV-/optically selected $z \approx 2$ star forming galaxies show a preponderance of thick gas-rich rotating disks and only a minority of major mergers (Förster Schreiber et al., 2006; Genzel et al., 2006, 2008; Shapiro et al., 2008). In contrast, SMGs are probably short-lived maximum-starburst galaxies undergoing dissipative major mergers (Tacconi et al., 2006; Bouché et al., 2007; Tacconi et al., 2008). Table 4.2 summarises key properties of these $z \approx 2$ galaxy samples.

How do these observations fit into the concordance cosmological model? Modern simulations of dark matter structure formation are robust and fixed by the cosmological parameters. However, complicated baryonic physics makes it difficult to model the evolution of galaxies and reproduce, for example, the high SFRs of these $z \approx 2$ galaxies (Daddi et al., 2007).

Galaxies at $z \approx 2$ differ significantly from local galaxies. The central mass densities of SMGs and of massive quiescent galaxies at the same redshift (van Dokkum et al., 2008 and references therein) are an order of magnitude greater than those of local spheroids and disks (Tacconi et al., 2008). Also, the $z \approx 2$ rotating disks are thick and turbulent, unlike local disk galaxies. These differences raise the question: what are the local Universe descendants of these $z \approx 2$ galaxies?

In this chapter we use the cosmological dark matter Millennium Simulation (Springel et al., 2005b; §4.3) to investigate the possible role of major mergers in galaxy formation at $z \approx 2$ (§4.4), and to consider the evolution of the $z \approx 2$ galaxies to $z = 0$ (§4.5).

Galaxy sample	SFR [$M_{\odot} \text{ yr}^{-1}$]	Halo mass [M_{\odot}]	Comoving number density [$h_{0.7}^3 \text{ Mpc}^{-3}$]	Major merger fraction
SINS	$\approx 30 - 300^1$	$10^{11.84} v_{200}^3 \times (\frac{1+z}{3.2})^{-1.5} h_{0.7}^{-12}$	$1 - 2.2 \times 10^{-434}$	$\approx 0.3^5$
SMGs ⁶	$\approx 750 \pm 300^7$	-	$1 - 2 \times 10^{-53}$	$\approx 1^3$

Table 4.1: Properties of galaxy samples at $z \approx 2$. (1) Förster Schreiber et al., 2009 ; (2) Förster Schreiber et al., 2006 ; (3) Tacconi et al., 2008 and references therein ; (4) BX/BM & sBzK galaxies with $K \leq 20$; (5) Shapiro et al., 2008 ; (6) $S(850\mu\text{m}) \geq 5\text{mJy}$; (7) Genzel, priv. comm.

4.3 Analysis of the Millennium Simulation

4.3.1 The Millennium Simulation and its merger trees

The Millennium Simulation is a cosmological N-body simulation. It follows 2160^3 dark matter particles of mass $8.6 \times 10^8 h^{-1} M_\odot$ in a box of $500h^{-1}$ Mpc on a side from $z = 127$ to $z = 0$. There are 64 output times (snapshots), at ≈ 300 Myr intervals at $z \lesssim 3$. The cosmology is Λ CDM, with $\Omega_m = 0.25$, $\Omega_\Lambda = 0.75$, $\Omega_b = 0.045$, $h = 0.73$, $n = 1$ and $\sigma_8 = 0.9$.

In the Millennium Simulation, structures are identified in two steps. First, the friends-of-friends (FOF) algorithm (Davis et al., 1985) creates a catalogue of FOF groups at each snapshot. The FOF groups represent dark matter halos. Second, bound substructures are identified inside the FOF groups (SUBFIND; Springel et al., 2001), so that each halo contains at least one subhalo. The Millennium merger trees are constructed by finding a single descendant for each *subhalo* in the following snapshot, while the FOF groups themselves play no role in constructing the merger trees.

In traditional merger trees, mergers are instantaneous, i.e. there is no information on their durations. Therefore, the Millennium public merger trees¹ can be used to determine the merger rate, which is merely a count of the number of mergers per unit time (Fakhouri & Ma, 2008; Genel et al., 2009). However, they cannot be used to determine important quantities such as the major merger fraction, defined as the fraction of halos undergoing major mergers at a given time, or the mass growth rate of each halo.

4.3.2 Constructing new merger trees

To derive merger fractions and mass growth rates, we must consider the finite physical durations of mergers. Therefore, start and end points must be defined. Also, to derive these quantities for entire dark matter halos rather than for subhalos, new trees have to be constructed based on FOF groups. In our procedure, the main subhalo in each FOF group is identified and is then followed to its subhalo descendant, using the original subhalo-based trees. The FOF group to which the subhalo descendant belongs is defined as the FOF group descendant of the original FOF group. Thus, in our new trees each node is an entire FOF group, rather than a subhalo. If two subhalos merge while within a single FOF group we do not count this as a merger event.

We identify a merger whenever two or more FOF groups at snapshot s have a common descendant at snapshot $s + 1$. However, at this time the halos are not necessarily already physically merging, since they may still be well separated. To account for that, we track the distances between the subhalo descendants of the main subhalos of the original FOF groups. These subhalos represent, approximately, the centers of the entire halos. We then define the start point of the merger as the last snapshot at which this distance is still larger than the sum of the virial radii of the original halos (FOF groups). In some mergers the

¹The Structure catalogues and derived merger trees have been made public by the Virgo Consortium: <http://www.mpa-garching.mpg.de/millennium>.

subhalos disappear before the distances become smaller than the sum of the original virial radii. When this happens the start point is defined as just one snapshot prior to the point where the subhalos merge and/or disappear.

After a merger begins, one of the halos becomes a substructure within the other. This substructure typically dissolves too quickly to be followed until the merger is physically complete. To overcome this problem we first estimate the duration of mergers T_{merger} , and define their end point as T_{merger} after the start point. To estimate the durations, we considered the fitting functions of Boylan-Kolchin et al. (2008) and Jiang et al. (2008), which are based on simulations of mergers. Our results are qualitatively robust with respect to this choice. We present quantitative results based on the orbit-averaged Boylan-Kolchin et al. (2008) fitting function for the dynamical friction merger time: $T_{\text{merger}} = 0.05 \frac{r^{1.3}}{\ln(1+r)} \frac{1}{H(z)}$, where r is the mass ratio and $H(z)$ is the Hubble constant at redshift z .

The accretion rate we associate with each merger equals the amount of accreted mass divided by the merger duration T_{merger} .

To summarise, we construct new FOF group-based merger trees, in which each FOF group also contains information about internal on-going mergers. The accretion rates associated with those mergers are summed up to obtain the total accretion rate onto the FOF group in question. The merger mass ratio is determined by the masses of the FOF groups at snapshot s , just prior to the appearance of a common FOF group descendant at snapshot $s + 1$. We define major mergers as those with mass ratios between 3 : 1 and 1 : 1 (with 1 : 1 being the most "intense" type of merger). If the most intense merger associated with a halo lies between 3 : 1 and 1 : 1, the halo is labelled as undergoing a major merger.

4.4 Galaxies at $z \approx 2$

Figure 4.1 shows halo number densities (*shaded contours*) and major merger fractions (*red contours*) as functions of halo mass and dark matter accretion rate for $z \approx 2.2$. It shows that the major merger fraction is an increasing function of *specific* dark matter accretion rate ($\frac{\dot{M}_{\text{DM}}}{M_{\text{halo}}}$), as both quantities increase towards the upper-left direction of the plane. This trend holds at all redshifts.

The mean accretion rate scales with halo mass and redshift as

$$\langle \dot{M}_{\text{DM}} \rangle \approx 35 M_{\odot} \text{yr}^{-1} (1+z)^{2.2} M_{12}^{1.07} \quad (4.1)$$

where $M_{12} \equiv \frac{M}{10^{12} M_{\odot}}$. The 1σ scatter equals $\approx \langle \dot{M}_{\text{DM}} \rangle \times (\frac{2.5}{1+z})^{0.2}$, which reflects more the upwards scatter, although negative accretion rates do exist for some halos (because of tidal stripping or fluctuations related to the FOF algorithm). Our numerical results are in good agreement with the analytic approximation for the accretion rate presented by Neistein et al. (2006), which is based on the extended Press-Schechter (EPS) model (Press & Schechter, 1974; Bond et al., 1991; Bower, 1991). The Neistein et al. (2006) approximation has a somewhat stronger mass and redshift dependence compared to our

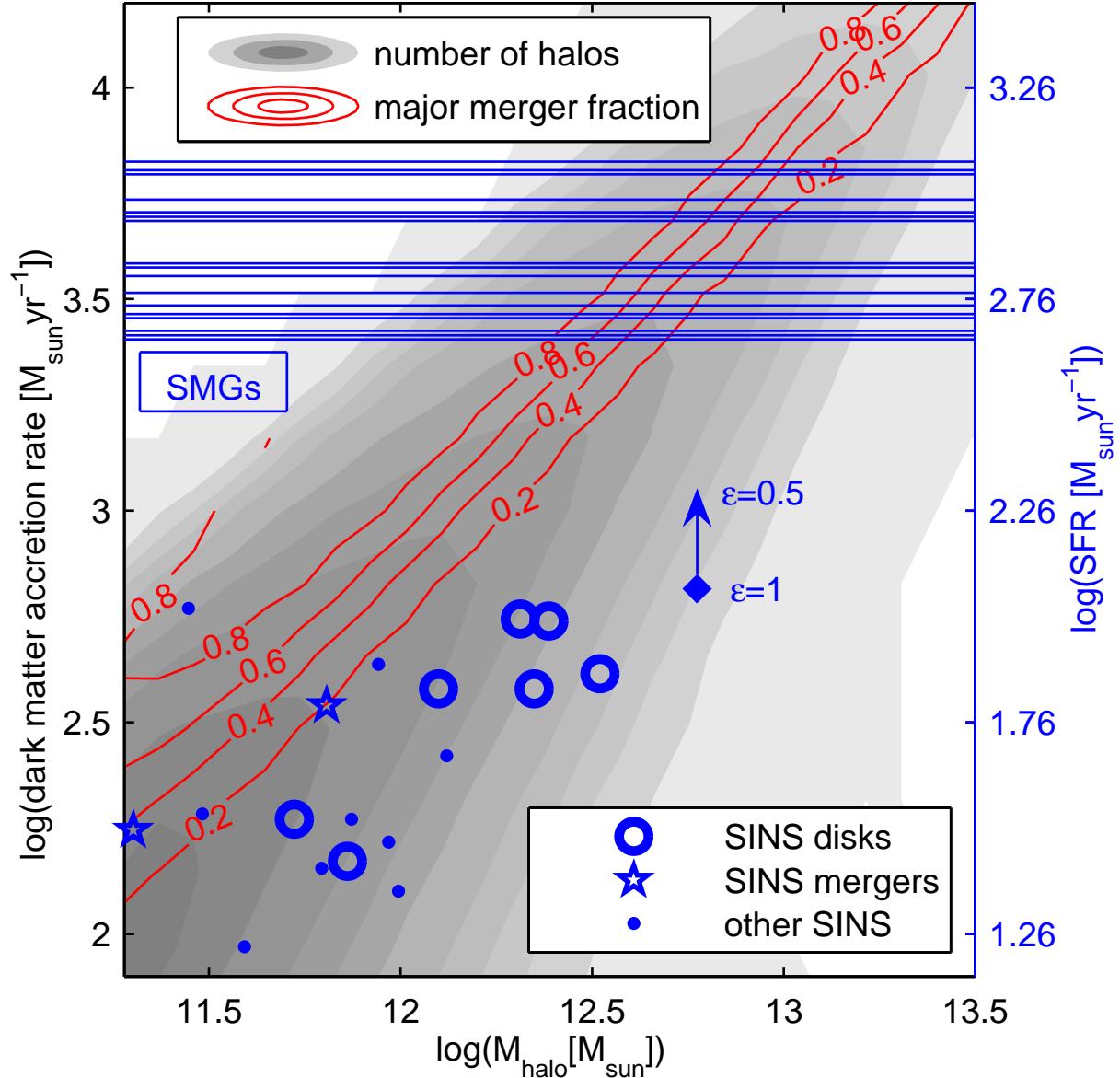


Figure 4.1: The distribution (*shaded contours*) of $z \approx 2.2$ halos in the dark matter accretion rate (left y-axis) versus halo mass plane. Also major merger fractions are displayed (*red contours*). Associated SFRs are indicated (right y-axis) assuming an effective star formation efficiency $\epsilon = 1$ in equation 4.2. SINS galaxies at $2 < z < 2.5$ are indicated as disks (*circles*) or mergers (*stars*) based on the Shapiro et al. (2008) classification, and others (*points*) not investigated by Shapiro et al. (2008). Their SFRs are based on their $H\alpha$ fluxes corrected for extinction using $A_{H\alpha} = 0.8$. Their halo masses were determined by assuming that the observed disk maximum rotation velocity is equal to the circular velocity of the halo (Förster Schreiber et al., 2006), and only galaxies with $M_{\text{halo}} > 10^{11.25} M_{\odot}$ are included. The SFRs for the SMGs are shown as the horizontal lines in the upper part of the figure (because the SMGs are compact, their halo masses cannot be reliably inferred from the observed gas motions). The *left* y-axis indicates what dark matter accretion rates are needed to account for the observed SFRs when assuming $\epsilon = 1$. The arrow indicates the shift in the galaxy positions if $\epsilon = 0.5$.

results. For example, at $z = 0$ and $M = 10^{12} M_{\odot}$, their accretion rate is $\approx 10\%$ higher, and at $z \approx 3$ and $M = 10^{14} M_{\odot}$ it is a factor of ≈ 2 higher. For halos of particular interest for this chapter, i.e. of $M \approx 10^{12} M_{\odot}$ at $z \approx 2$, the Neistein et al. (2006) approximation exceeds our equation 4.1 by $\approx 30\%$.

To compare our results to observed galaxies, we assume that the galaxies are the central galaxies of their halos. We convert dark matter accretion rate (\dot{M}_{DM}) into SFR (\dot{M}_{*}) using the baryonic fraction $\eta_B = 0.18$ and an effective star formation efficiency ϵ , which is a free parameter used to interpret the results:

$$\dot{M}_{*} = \eta_B \times \epsilon \times \dot{M}_{DM}. \quad (4.2)$$

In the "cold flow" regime ($M_{\text{halo}} \lesssim 10^{12} M_{\odot}$; Birnboim & Dekel, 2003; Kereš et al., 2005; Ocvirk et al., 2008) equation 4.2 is a plausible measure of the baryonic accretion rate. At larger masses the accretion rate is lower and is controlled by the cooling time in the hot virialised baryonic halo gas. At much smaller masses it is strongly reduced by outflows generated by supernovae feedback. In the cold flow regime, the cold gas (which may be clumpy) is fed at approximately virial velocity via filaments directly into the halo center, where it accumulates onto the galaxy. Moreover, considering the case in which gas is stripped off incoming galaxies, our estimated merger duration is related to the dynamical time of the halo, on which the gas will fall to the central galaxy when the cooling time is short. For major mergers ϵ may even exceed 1, because the star formation burst they trigger can be shorter than the dark matter halo merger time scale (e.g. Springel & Hernquist, 2005; Tacconi et al., 2008).

4.4.1 SINS galaxies

On Figure 4.1 we overplot the SINS galaxies. Their SFRs are based on their $H\alpha$ fluxes corrected for extinction using $A_{H\alpha} = 0.8$, and their halo masses were estimated by assuming that the observed disk maximum rotation velocity is equal to the circular velocity of the halo (Förster Schreiber et al., 2006). Figure 4.1 shows that if $\epsilon \gtrsim 0.5$ is assumed, the host halos of SINS galaxies with $M_{\text{halo}} > 10^{11.25} M_{\odot}$ lie in the region where most halos of their mass are expected to be concentrated. Furthermore, for $\epsilon \gtrsim 0.5$ the expected mass accretion rates are sufficient to account for the observed SFRs. Also, the predicted major merger fraction is small ($\lesssim 0.5$), consistent with observations. Although the statistics are still small, we note that the confirmed SINS mergers (Shapiro et al., 2008; *stars*) have higher specific dark matter accretion rates than the confirmed disks (*open circles*), and therefore come from a region where the halo major merger fraction is higher.

The computed number density of halos with $M \approx 10^{11.5} - 10^{12} M_{\odot}$ is a few times higher than the observed number density of the galaxies the SINS sample is drawn from (Table 4.2). Possibly, the observed galaxies have typically high $M_{\text{gal}}/M_{\text{halo}}$, with other halos of comparable mass hosting fainter undetected galaxies. Also, some of the halos in this mass range may have already developed virial shocks that quench star formation.

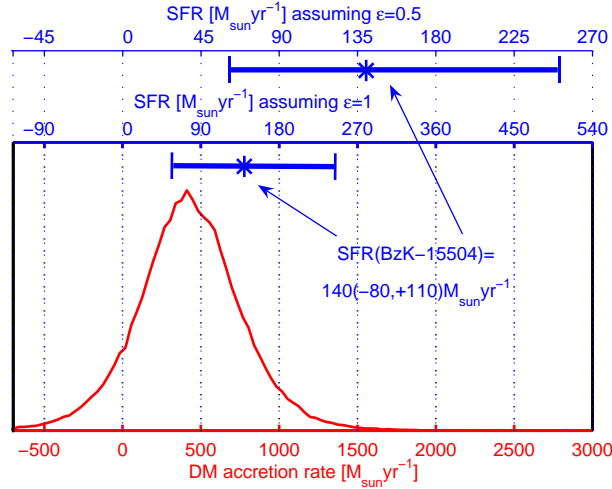


Figure 4.2: The distribution of dark matter accretion rates for halos with masses $(1.2 \pm 0.3) \times 10^{12} M_{\odot}$ at $z \approx 2.4$ (corresponding to the halo mass and redshift of BzK-15504), which are not undergoing a major merger. The SFRs on the upper axes are given assuming effective star formation efficiencies $\epsilon = 1$ and $\epsilon = 0.5$. The measured SFR of $140(-80, +110) M_{\odot} \text{yr}^{-1}$ in BzK-15504 is indicated by the asterisks and error bars.

It should be noted that our estimated major merger duration T_{merger} equals $\approx 350 - 1000$ Myr at $z \approx 2.2$, depending on the mass ratio. This is very similar to the "observable" galaxy merger timescale often found in the literature (e.g. Conselice, 2006; Lotz et al., 2008b). Therefore, the approximation taken here, i.e. considering the halo merger fraction directly and inferring the galaxy merger fraction from it, is probably a reasonable one with respect to the deduced merger fraction of the SINS galaxies.

Genzel et al. (2006) studied BzK-15504 with high resolution using adaptive optics, and concluded that it was a large proto-disk with no sign of a recent/ongoing major merger, and a SFR of $140(-80, +110) M_{\odot} \text{yr}^{-1}$. Förster Schreiber et al. (2006), Law et al. (2007), Genzel et al. (2008), Cresci et al. (2009), Bournaud et al. (2008) and van Starckenburg et al. (2008) have found similar systems. Figure 4.2 shows that for halos not undergoing major mergers, and with masses equal to the halo mass of BzK-15504, the typical dark matter accretion rate is $\approx 450 M_{\odot} \text{yr}^{-1}$, i.e. the typical SFR assuming $\epsilon = 1$ is $\approx 80 M_{\odot} \text{yr}^{-1}$. About 15% of such halos have SFRs exceeding the $140 M_{\odot} \text{yr}^{-1}$ observed in BzK-15504 (again assuming $\epsilon = 1$). Thus, the implied dark matter accretion rate in BzK-15504 may be quite typical. Considering the uncertainty in the measured SFR, the implied dark matter accretion rate is consistent with theoretical expectations for ϵ as low as ≈ 0.5 .

We conclude that high star formation rates and large abundances of non-major merger, massive disks at $z \approx 2$ are consistent with expectations from Λ CDM simulations if accretion is in the "cold flow" regime and the star formation efficiency is high.

4.4.2 SMGs

For $\epsilon \approx 1$, the observed SFRs of the SMGs imply dark matter accretion rates of $\approx 2500 - 6000 M_{\odot} \text{ yr}^{-1}$ (Figure 4.1). When examining halos with accretion rates in this range that are undergoing major mergers, we find that their masses lie mostly in the range $(2 - 6) \times 10^{12} M_{\odot}$ and obey a log-normal distribution with a mean $\approx 3 \times 10^{12} M_{\odot}$ and $\sigma \approx 0.25 \text{ dex}$. We also find that their number density is $\approx 5 \times 10^{-5} \text{ Mpc}^{-3}$. This is only slightly larger than the observed SMG density (Table 4.2), and supports the conclusions of Tacconi et al. (2006, 2008) that the SMGs represent major mergers. If the SMG phase is shorter than the halo merger duration, such that $\epsilon > 1$, the implied number density is not much altered, but lower halo masses are found. E.g., if the SMG phase lasts only 100 Myr, the mean halo mass is $\approx 10^{12} M_{\odot}$, in which case SMGs could be members of the UV-/optically selected galaxy populations that have recently experienced a dissipative major merger. The observed rotation velocities of SMGs are larger than the expected circular velocities of halos with these inferred masses. This is consistent with the SMGs being concentrated major mergers in which the rotation velocities peak close to the center.

4.5 Fate at $z = 0$

4.5.1 Fate of SINS galaxies

Figure 4.3 summarizes the major merger history of halos from $z \approx 2.2$ to $z = 0$. For halos with initial masses typical of the SINS galaxies' halos, $\approx 40\%$ will be accreted via minor mergers by more massive halos (representing groups or clusters) with final masses $10^{13} M_{\odot} \lesssim M \lesssim 10^{15} M_{\odot}$ at $z = 0$. Around one half of those halos will merge fully with the central subhalo of the group/cluster, and the other half will remain satellite subhalos. The other $\approx 60\%$ remain "main branch" halos to $z = 0$. Of these, $\approx 2/3$ undergo at least one major merger during their evolution to $z = 0$. Their final halo masses are $10^{12.3} M_{\odot} \lesssim M \lesssim 10^{13.3} M_{\odot}$, so their associated galaxies may become massive elliptical galaxies (cf. Conroy et al., 2008). The other $\approx 1/3$ do not undergo any future major mergers, and grow to a mass $10^{11.8} M_{\odot} \lesssim M \lesssim 10^{12.5} M_{\odot}$ at $z = 0$. Thus, these may evolve via secular evolution into bulges and later possibly grow a new disk.

4.5.2 Fate of SMGs

A popular scenario is that the large central mass densities of SMGs and of $z \approx 2$ compact red sequence galaxies are reduced by $z = 0$ via dry dissipationless mergers (van Dokkum, 2005; Bell et al., 2006a; Naab et al., 2006b). Tacconi et al. (2008) show (in their Figure 5) that this requires that the SMG masses grow by about an order of magnitude by $z = 0$, assuming dry mergers with structurally similar systems, following Nipoti et al. (2003). We find that of the halos we have identified with the SMGs in §4.4.2, $\approx 70\%$ remain "main branch" halos to $z = 0$ (Figure 4.3), and that their masses grow by factors of $\approx 3 - 30$. This mass growth appears consistent with the requirement of the dry merger hypothesis.

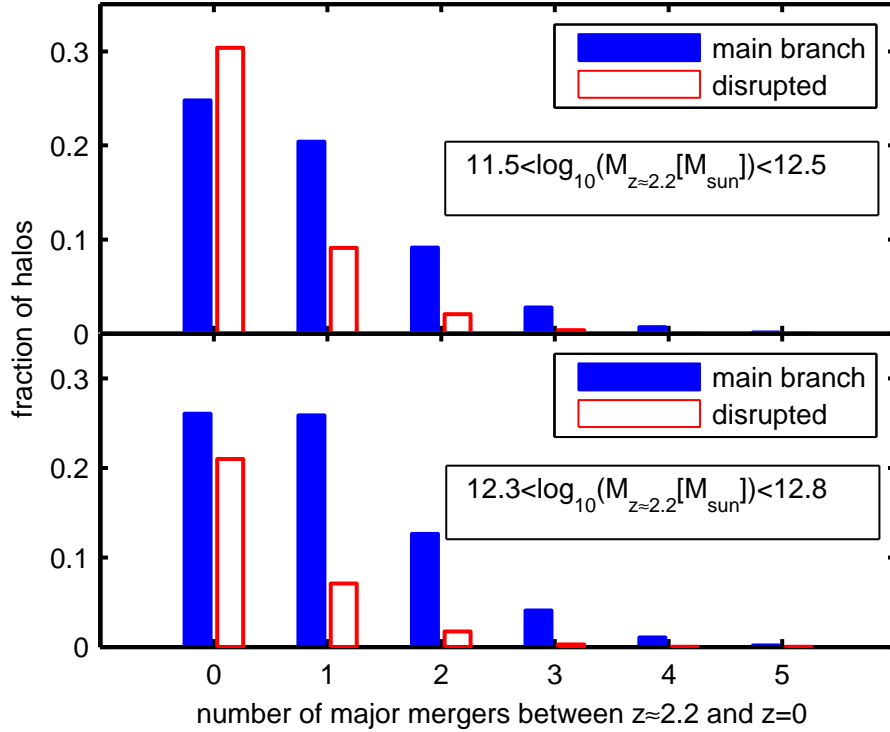


Figure 4.3: The number of *future* major mergers that halos with initial ($z \approx 2.2$) masses $10^{11.5} M_{\odot} < M < 10^{12.5} M_{\odot}$ (*top*) and $10^{12.3} M_{\odot} < M < 10^{12.8} M_{\odot}$ (*bottom*) undergo from $z \approx 2.2$ to $z = 0$. We distinguish between (a) "main branch" halos that undergo only minor mergers to $z = 0$ (*filled blue column at 0*), (b) "main branch" halos that undergo at least one major merger (*filled blue columns at > 0*) and (c) "disrupted" halos (*red*). These are halos that at some stage are accreted onto a more massive halo in a minor merger event. For category (c), major mergers are counted only prior to merging with the larger halo. Around 60% ($\approx 70\%$) of the halos in the lower (higher) mass bin remain "main branch" halos. For both mass bins the mean number of future major mergers is ≈ 1 , while fewer than 10% undergo more than 2 major mergers. These results do not depend on whether the initial halo at $z \approx 2.2$ is identified as a major merger or on its dark matter accretion rate. We find that the mean number of major mergers a halo with mass M undergoes between z_i and $z_f < z_i$ is well approximated by: $\bar{N}_{\text{mm}}(z_i, z_f, M) \approx 0.13 \times (\log(\frac{M}{10^{10} M_{\odot}}) + 1)(z_i - z_f)$.

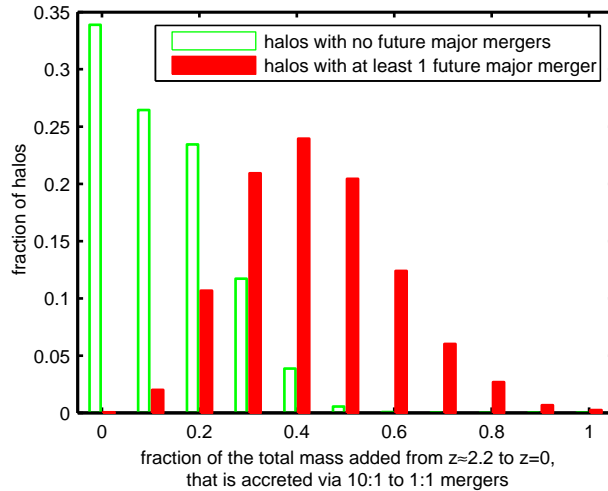


Figure 4.4: Mass growth to $z = 0$ of halos with initial ($z \approx 2.2$) masses $10^{12.3} M_{\odot} < M < 10^{12.8} M_{\odot}$ that remain "main branch" halos (*filled blue columns in the bottom Panel of Figure 4.3*). The plot displays the relative number of halos versus the fraction of the total mass added from $z \approx 2.2$ to $z = 0$ that is accreted via mergers more intense than 10 : 1. Results are shown for halos that undergo no major mergers to $z = 0$ (*green*) and halos that undergo at least one major merger to $z = 0$ (*filled red*). The results do not depend on whether the halo at $z \approx 2.2$ is undergoing a major merger or on its accretion rate.

However, most of the mass growth does not occur via major mergers, since typically only ≈ 1 major merger occurs per halo to $z = 0$, as shown by Figure 4.3.

Moreover, we show in Figure 4.4 that most of the mass growth is achieved via mergers less intense than 10 : 1, which is qualitatively consistent with the idea that the growth of massive galaxies is not dominated by major mergers (e.g. Hausman & Ostriker, 1978; Maller et al., 2006; Masjedi et al., 2008). This is especially true for the halos that do not undergo further major mergers until $z = 0$. Such halos tend to grow in mass only by a factor of ≈ 3 , and gain $\gtrsim 0.7$ of their new mass via mergers less intense than 10 : 1. Also, the galaxies themselves probably grow even less than their dark matter halos. It seems unlikely that the mass accreted via such small halos can be sufficiently gas poor for minor dry mergers (e.g. Burkert et al., 2008) to be an important growth mechanism (unless the galaxies are effectively stripped of their gas before merging with the descendant of the SMG; Naab et al., 2007).

A simpler and more likely explanation (Tacconi et al., 2008) is that the high SMG densities trace only the central starburst region, and exclude more extended fainter envelopes of pre-merger stars. At lower redshifts these stars would become visible and be of greater relative importance as the starburst fades, giving rise to larger half-light radii and smaller inferred densities (cf. simulations by Hopkins et al., 2008b).

4.6 Summary

We have constructed new halo merger trees from the Λ CDM Millennium Simulation. Our trees account for merger durations, and we use them to identify halos that are undergoing mergers and to extract dark matter accretion rates. We show that the high star formation rates observed in rotating disks at $z \approx 2$ are plausibly consistent with the dark matter accretion rates expected for halos not undergoing major mergers. Given the measured star formation rates of SMGs, and the observationally supported assumption that they are undergoing major mergers, we infer their likely halo masses. Major mergers can lead neither to the complete transformation of the $z \approx 2$ disks to $z = 0$ elliptical galaxies or to the disappearance of the very high density SMGs from $z \approx 2$ to $z = 0$. Therefore, secular/internal processes are likely important in the evolution of these high-redshift populations to present time.

Chapter 5

Short-lived giant clumps in $z \approx 2$ disks

Note: This chapter is an extended version of Genel et al. (2010b).

5.1 Abstract

Many observed massive star-forming $z \approx 2$ galaxies are large disks that exhibit irregular morphologies, with ≈ 1 kpc, $\approx 10^{8-10} M_{\odot}$ clumps. We present high-resolution cosmological SPH simulations that zoom-in on the formation of individual $M_{*} \approx 10^{10.5} M_{\odot}$ galaxies in $\approx 10^{12} M_{\odot}$ halos at $z \approx 2$. Our code includes strong stellar feedback parameterized as momentum-driven galactic winds. This model reproduces many characteristic features of this observed class of galaxies, such as their clumpy morphologies, high gas fractions ($f_g \approx 30\%$) and high specific star-formation rates ($\approx 1 \text{ Gyr}^{-1}$). In accord with recent models, giant clumps ($M_{\text{clump}} \gtrsim 5 \times 10^8 M_{\odot}$) form in-situ via gravitational instability. However, the galactic winds are critical for their subsequent evolution. In the cases we have studied, the clumps are short-lived and are disrupted by wind-driven mass loss. They do not virialise or migrate to the galaxy centers as suggested in recent work neglecting strong winds. Our simulations agree well with new observational constraints on clump kinematics and with the detection of winds from high-redshift galaxies and in particular from individual clumps.

5.2 Introduction

Star-forming disk galaxies at $z \approx 2$ differ from their local counterparts in several aspects: they are more gas-rich and rapidly star-forming, and have irregular morphologies and high gas velocity dispersions. Spatially resolved observations of their rest-frame UV and optical continuum light often reveal large (≈ 1 kpc) clumps (Elmegreen et al., 2005). Clumpy morphologies are also observed with star-formation tracers such as $\text{H}\alpha$ (e.g. the SINS survey;

Förster Schreiber et al., 2009). The spectrally resolved line emissions reveal ordered rotation and high velocity dispersions, arguably tracing gas-phase turbulence (Genzel et al., 2006, 2008; Förster Schreiber et al., 2006; Shapiro et al., 2008; Cresci et al., 2009).

Theoretically, the large $z \approx 2$ star-forming galaxies have been considered as marginally-unstable thick disks, where the large random motions set the large masses and sizes for unstable regions collapsing into giant clumps (Bournaud et al., 2007, 2008; Genzel et al., 2008; Elmegreen et al., 2008a; Burkert et al., 2010; Agertz et al., 2009; Dekel et al., 2009b; Ceverino et al., 2010). In this picture, the high star-formation rates result from the high growth rates of cosmic structures at $z \approx 2$ (Genel et al., 2008), as gas funnels directly from the cosmic web to the vicinity of galaxies in a 'cold-mode' accretion (Kereš et al., 2005; Dekel et al., 2009a). However, several observational hints have not yet been addressed in this framework. First, vigorous outflows are observed from a variety of star-forming galaxies at high redshift, both globally (e.g. Pettini et al., 2000; Steidel et al., 2010) and also from individual giant clumps (Genzel et al., 2010). Second, high signal-to-noise observations of individual giant clumps reveal only minor kinematical signatures, sometimes indicating dynamical masses lower than alternative independent clump mass estimates (Genzel et al., 2010). Third, abundance matching of galaxies and dark matter halos suggests that at $z \approx 2$, much like at $z = 0$, typically not more than $\approx 20\%$ of the baryons associated with halos of any mass have turned into stars (Moster et al., 2010), causing some tension with the high efficiency of 'cold-mode' accretion.

A crucial issue is whether giant clumps survive long enough to become stellar-dominated and/or sink to their galaxies' centers, contributing to the buildup of bulges (Immeli et al., 2004b; Genzel et al., 2008; Dekel et al., 2009b; Shapiro et al., 2010; Murray et al., 2010b; Krumholz & Dekel, 2010). Conflicting theoretical claims have been made, while observations are not yet conclusive. However, none of the cosmological or isolated simulations reported so far (but see Sales et al., 2010), which find long-lived migrating clumps, included strong feedback from star-formation. As the 'clumpy phase' appears to be ubiquitous at $z \approx 1 - 3$, it is of fundamental importance for our understanding of galaxy formation to know what role giant clumps play in building bulges/spheroids.

In this chapter, we demonstrate as a proof of principle, that incorporating galactic superwinds resulting from stellar feedback into the existing theoretical picture, can have important implications for our understanding of $z \approx 2$ disks and their evolution. We use hydrodynamical cosmological simulations to investigate the formation and properties of a small sample of star-forming disks. Comparing to observed galaxies, we conclude that the giant clumps may be short-lived transient features, due to the strong feedback (which is observed at high redshift). In an upcoming paper, we will present a comprehensive study of parameter space and resolution, study the relationship between halo formation histories and the characteristics of their central galaxies, and perform a broader comparison with observations.

5.3 The Simulations: Code and Setup

We run 'zoom-in' cosmological simulations focused on individual halos taken from the $72h^{-1}$ Mpc cosmological dark matter simulation presented in Oser et al. (2010) that uses the following cosmological parameters: $\Omega_m = 0.26$, $\Omega_\Lambda = 0.74$, $\Omega_b = 0.044$, $h = 0.72$, $n = 0.95$ and $\sigma_8 = 0.77$. As we focus on massive disks with high star-formation rates (SFR), we select $\approx 10^{12} M_\odot$ halos at $z = 2$ with no major merger (mass ratio $< 3 : 1$) since $z = 3$ and instantaneous dark matter growth rates exceeding $500 M_\odot \text{ yr}^{-1}$ (see Genel et al., 2008). These criteria are met by $\approx 15\%$ of the halos in the relevant mass bin, i.e. our galaxies form in halos that are neither the most 'typical' nor very 'special' or rare. From this sample, we randomly selected six halos and generated 'zoom-in' initial conditions (as in Oser et al., 2010) for re-simulations including baryons, with mass resolution of $8 \times 10^5 M_\odot$ and $5 \times 10^6 M_\odot$ for baryonic and high-resolution dark matter particles, respectively. The gravitational softening lengths of baryonic particles are $200h^{-1}$ pc, constant in comoving units, resulting in physical softening lengths of ≈ 90 pc at $z = 2$.

The cosmological box is evolved to $z = 2$ with the extended N-body/SPH code *Gadget-2* (Springel, 2005) version of Oppenheimer & Davé (2006, 2008). This version includes ionisation and heating by a uniform background radiation (Haardt & Madau, 2001) in the optically thin limit, atomic cooling down to $T = 10^4 K$ from hydrogen and metals, star-formation and feedback, as well as mass loss and metal enrichment from AGB stars and supernovae of types II and Ia.

The Springel & Hernquist (2003a) star-formation model used in Oppenheimer & Davé (2008), which has a stiff effective equation of state, is replaced by the Schaye & Dalla Vecchia (2008) approach. There, the usual cooling and heating operate at $\rho < \rho_{EOS}$, while for $\rho > \rho_{EOS}$ a polytropic equation of state with $\gamma = 4/3$ is implemented. This ensures that the (thermal) Jeans mass M_J remains constant with varying density and does not become unresolved. Here $\rho_{EOS} = 0.1 \text{ cm}^{-3}$ is defined such that $M_J \approx 1.4 \times 10^7 M_\odot$ at $\rho = \rho_{EOS}$ and $T = 10^4 K$. Star-formation is parameterised as

$$\frac{d\rho_*}{dt} = \frac{\rho}{1 \text{ Gyr}} \left(\frac{\rho}{\rho_{th}} \right)^{1.26}, \quad (5.1)$$

with the star-formation density threshold $\rho_{th} = \rho_{EOS} = 0.1 \text{ cm}^{-3}$, which reproduces the Kennicutt (1998) 2D star-formation relation (Schaye & Dalla Vecchia, 2008). In addition, we calculate the local minimum (of all directions) gas surface density $\rho^2/|\nabla\rho|$ (Gnedin et al., 2009), and suppress star-formation if $\rho^2/|\nabla\rho| < 10^{21} \text{ cm}^{-2}$.

The feedback scheme developed by Oppenheimer & Davé (2006, 2008) builds on the kinetic feedback scheme of Springel & Hernquist (2003a), where star-forming gas particles are stochastically kicked with velocities in the $\mathbf{v} \times \mathbf{a}$ direction, where \mathbf{v} is the particle's velocity prior to the kick and \mathbf{a} its acceleration. Subsequently, they are decoupled from hydrodynamics for a short time to allow them to propagate out of their star-formation sites and eventually leave their galaxies. Oppenheimer & Davé (2006) used this mechanism with a significant change to the two parameters that control the wind. In their model, the

magnitude of the kick is $v_{wind} = \sigma(2 + 3\sqrt{f_L - 1})$ and the mass-loading factor

$$\frac{\dot{M}_W}{SFR} \equiv \eta = \frac{\sigma_0}{\sigma}, \quad (5.2)$$

where $f_L \approx 1 - 2$ is the luminosity factor, σ is the ‘velocity dispersion’ of the galaxy that is calculated from its mass based on an on-the-fly group finder¹, and σ_0 is a constant (here $\sigma_0 = 300 \text{ km s}^{-1}$). Introducing σ -dependencies, these two parameters scale with the mass of the galaxy, following the theory of momentum-driven winds induced by the radiation pressure from young stars (Murray et al., 2005; Zhang & Thompson, 2010), and in accordance with observational evidence (e.g. Martin, 2005; Rupke et al., 2005). The Oppenheimer & Davé (2006) model reproduces the observed metal enrichment of the intergalactic medium at $2 < z < 5$ and the galaxy mass-metallicity relation (Finlator & Davé, 2008).

We use $v_{wind} = \sigma(4 + 4.29\sqrt{f_L - 1})$, which ensures that wind particles can escape their galaxy, and gives typical velocities of $\approx 350 - 750 \text{ km s}^{-1}$ for the central galaxies considered. We also ensure that the velocity kicks are perpendicular to the disk by calculating $\mathbf{v} \times \mathbf{a}$ in the inertial frame of the galaxy.

5.4 Results

In this section we focus on a central galaxy of one of our halos, named *s224*, that is typical of our sample. We will discuss our full sample in detail elsewhere, but we briefly describe some global properties here. In Figure 5.1, panel (a) shows the SFR- M_* plane for galaxies in the high-resolution region. Stellar masses and SFRs are measured by the on-the-fly group finder. The simulated galaxies populate the same region as observed $z \approx 2$ galaxies, according to the Daddi et al. (2007) relation (*solid*) re-normalised by 0.3 dex downwards following Herschel measurements (Nordon et al., 2010). Figure 5.1(b) shows ‘baryon conversion efficiencies’ ($\frac{M_*}{M_{200}\Omega_b/\Omega_m}$) versus halo mass, where stellar masses are measured inside $0.1R_{200}$. Our simulated halos are presented (*symbols*) alongside the Moster et al. (2010) fit to observed mass functions (*black*). The baryon conversion efficiency is a strong function of mass in our simulations, though not as strong as observations suggest. Regardless, the global correlations in Figure 5.1 are a result of our wind model, without which they would compare much worse to the observations (Davé, 2008, 2009). We consider these observed correlations important constraints that simulated galaxies should match in order to be realistic. A third global property of our simulations is high gas fractions, $\sim 30\%$ for the central galaxies, in agreement with observations (Tacconi et al., 2010). The SFR history in the central galaxies is rather constant, as demonstrated in Table 5.1 by comparing the current SFR to its past average. Most central galaxies are clumpy (see below), as indicated in Table 5.1. Table 5.1 also gives halo masses, peak circular velocities, sizes, gas and stellar masses, gas fractions and SFRs.

¹For calculation efficiency, a friends-of-friends (FOF) algorithm is used, with a linking length $b = 0.025(\frac{H(z)}{H(0)})^{1/3}$ that is calibrated to the SKID group finder at various redshifts.

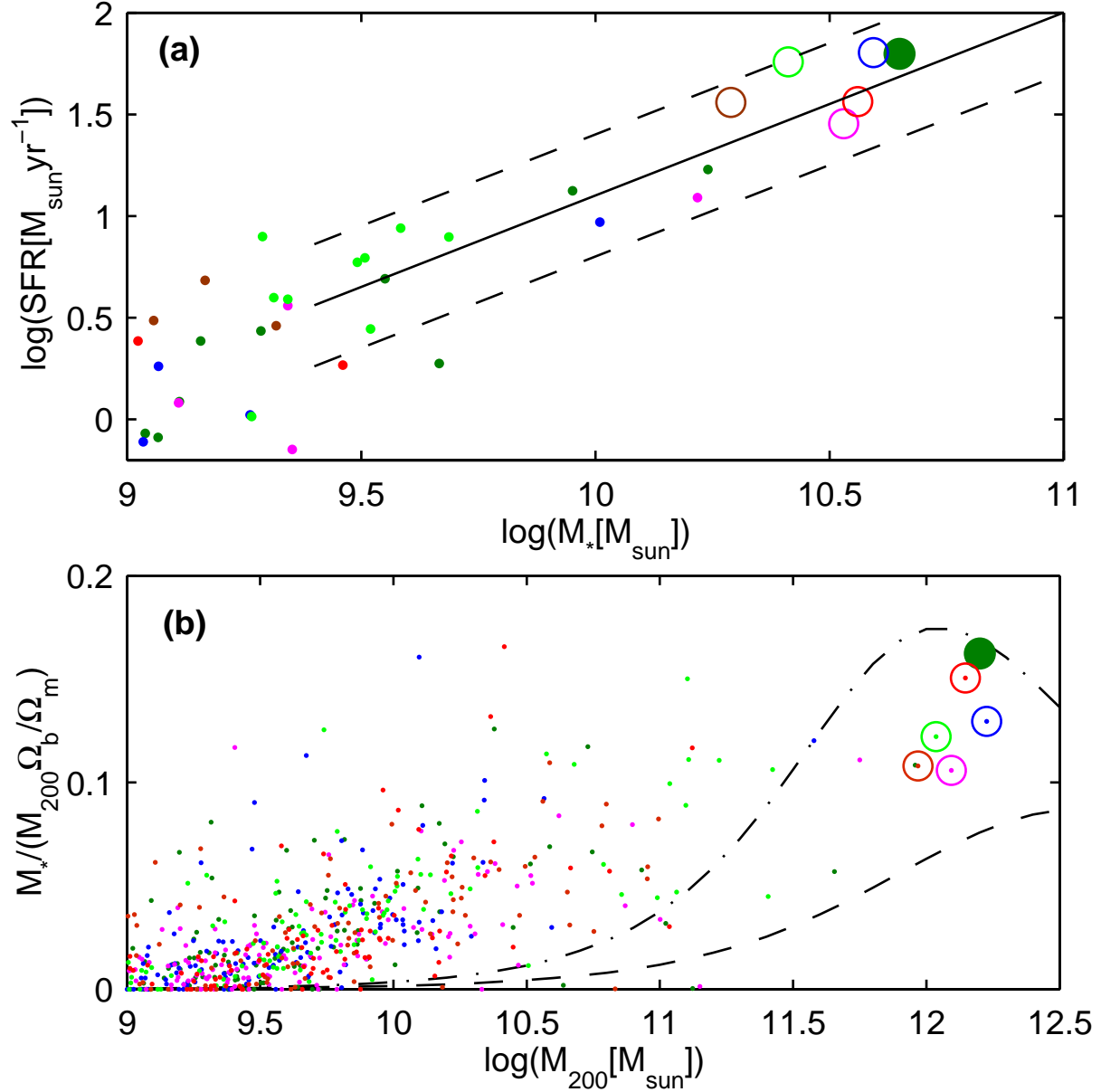


Figure 5.1: Global properties of six ‘zoom-in’ simulations at $z = 2$. *Top*: SFR versus stellar mass. Each color represents one simulation, with its central galaxy (*circles*) and the smaller galaxies in its vicinity (*dots*). The observed Daddi et al. (2007) relation (*solid*; standard deviation is *dashed*) is re-normalised by 0.3 dex downwards (see text). *Bottom*: ‘Baryon conversion efficiency’ as a function of halo mass. The highest efficiency of $\approx 15\%$ is obtained at $M_{\text{halo}} \gtrsim 10^{12} \text{M}_{\odot}$, in rough agreement with observations (Moster et al., 2010; $z = 2.5$ in *dashed black* and $z = 0$ in *dashed-dotted black*). The most massive high-resolution halo in each simulation is marked with a circle. The colors are as in the top panel. In both panels *s224* is marked with a filled circle.

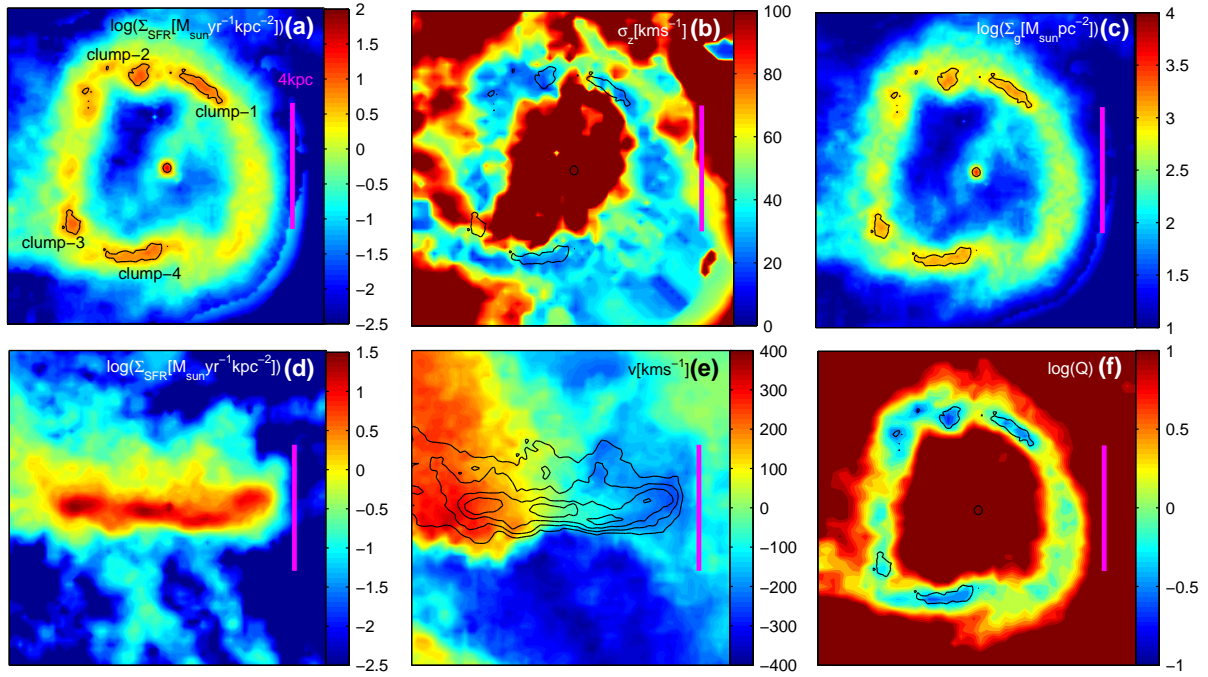


Figure 5.2: Gas properties of the central galaxy *s224* at $z = 2$. (a): face-on SFR surface density, (b): face-on line-of-sight (vertical) velocity dispersion, (c): face-on gas surface density, (d): edge-on SFR surface density, (e): edge-on line-of-sight velocity field overplotted with contours of SFR surface density and (f): $\log Q$. Each panel is 10 kpc on a side. All face-on panels are overplotted with $\Sigma_g = 1000 \text{ M}_\odot \text{ pc}^{-2}$ contours.

	M_{200} [$10^{12} M_{\odot}$]	peak $V_c \equiv \sqrt{\frac{GM}{R}}$ [kms^{-1}]	Half-mass radius $R_{1/2}^1$ [kpc]	Stellar mass ² [$10^{10} M_{\odot}$]	Gas mass ² [$10^{10} M_{\odot}$]	Gas fraction ²	SFR ² [$M_{\odot} \text{yr}^{-1}$]	Number of clumps ³	$\frac{\text{SFR}}{\langle \text{SFR} \rangle}$ ⁴
<i>s224</i>	1.48	278	3.3	3.82	2.04	35%	58.4	5	1.45
<i>s263</i>	1.75	289	3.3	3.43	2.06	37%	54	3	1.51
<i>s361</i>	1.02	238	4.6	2.12	0.78 ⁵	27%	9.8 ⁵	-	0.75 ⁵
<i>s377</i>	1.38	252	4.5	2.75	1.19	30%	18.9	6	1
<i>s383</i>	1.38	253	3.5	2.96	0.96	25%	15	6	0.86
<i>s447</i>	0.95	229	3.8	1.74	1.29	43%	20.9	4	1.6
<i>clump-1</i>	-	-	0.45	0.022	0.044	67%	2.7	-	-
<i>clump-2</i>	-	-	0.27	0.02	0.04	67%	2.3	-	-
<i>clump-3</i>	-	-	0.22	0.022	0.025	53%	1.5	-	-
<i>clump-4</i>	-	-	0.42	0.027	0.07	72%	3.7	-	-

Table 5.1: Galaxy and clump properties. (1) For galaxies: stellar (3D) half-mass radius within $0.2R_{vir}$, for clumps: gas half-mass radius inside the region with $\Sigma_g > 1000 M_{\odot} \text{pc}^{-2}$; (2) For galaxies: inside $2R_{1/2}$, for clumps: inside the region with $\Sigma_g > 1000 \text{cm}^{-3}$; (3) Identified as local overdensities in the gas surface density, excluding the galaxy center; (4) $\langle \text{SFR} \rangle$ is the mean SFR between $z = 3$ and $z = 2$; (5) The gas is mostly in an extended ($> 2R_{1/2}$) massive ring, induced by a $\approx 8 : 1$ merger, so the values here are underestimates.

We now discuss *s224*. The gas is mainly distributed in a ring at ≈ 3 kpc (Figure 5.2(c)). The ring, which is transient, formed from spiral features in the disk rather than by an interaction (there are no interactions with stellar mass ratios $< 20 : 1$ since $z \approx 3$). Several SFR overdensities are embedded in the ring (Figures 5.2(a) and 5.2(d)). Observationally, such regions are named giant clumps. Here for *s224* we use a threshold of face-on gas surface density $\Sigma_g > 1000 M_\odot \text{pc}^{-2}$ to identify four clumps (Figure 5.2(a)). With this definition, their masses are $\gtrsim 5 \times 10^8 M_\odot$ (Table 5.1). The gas vertical velocity dispersion σ_z is $\approx 20 - 100 \text{kms}^{-1}$ (Figure 5.2(b)), in agreement with observed values at $z \approx 2$. The high density regions and clumps are minima of σ_z (Aumer et al., 2010), as denser gas dissipates the random motions more quickly and is less prone to stirring effects such as external accretion. The disk shows regular rotation (Figure 5.2(e)), indicative of the quiet merger history (Shapiro et al., 2008). The clumps themselves have low ($\approx 50 \text{kms}^{-1} \text{kpc}^{-1}$) velocity gradients, not much larger than the galaxy-wide average velocity gradient, which is typically $\approx 30 \text{kms}^{-1} \text{kpc}^{-1}$ at a few kiloparsecs from the center.

Assuming a Q parameter (Toomre, 1964) of

$$Q \equiv \frac{\kappa \sqrt{\sigma_g^2 + c_s^2}}{\pi G \Sigma_g} \quad (5.3)$$

where σ_g is the local gas velocity dispersion, c_s the gas sound speed, and

$$\kappa = \sqrt{3} \sqrt{\frac{GM_{tot}(< R)}{R}} / R \quad (5.4)$$

(Dekel et al., 2009b), the clumps are local minima with $Q \ll 1$ (Figure 5.2(f)). The clumps' masses are 1 – 2 orders of magnitude larger than the thermal Jeans mass, but match the turbulent Jeans mass of the disk

$$M_{J,\sigma} \approx \left(\frac{\sigma_g}{v_{rot}}\right)^2 M_{disk} \gtrsim \left(\frac{20}{250}\right)^2 \times 6 \times 10^{10} M_\odot \approx 4 \times 10^8 M_\odot \quad (5.5)$$

(Genzel et al., 2008; Dekel et al., 2009b), which is driven to high values by the large random motions in the disk. The clumps tend to form inside spiral features, i.e. elongated overdensities in the disk, sometimes in transient rings, and reach a contrast ratio of $\gtrsim 3$ compared to their surroundings or to the mean disk surface density. The total SFR in all clumps is $\lesssim 20\%$ of the total disk SFR, in broad agreement with observations (Genzel et al., 2010; Förster Schreiber et al., 2010). The clumps are very gas rich ($f_g \sim 60\%$), and are comprised of two stellar populations. 'Background stars', whose age distribution is similar to that of the stellar disk as a whole, are generally not bound to the clump. 'Clump stars', which form over the lifetime of the clump, are mostly bound to it, and constitute typically up to $\approx 20\%$ of its *stellar* mass. Table 5.1 gives sizes, masses, gas fractions and SFRs for the clumps annotated in Figure 5.2(a).

A notable characteristic of the clumps is their short lifetimes, which are about half a disk orbital time, or ≈ 50 Myr. The top row in Figure 5.3 demonstrates the disruption of

a clump in *s224* by showing a time series of gas surface density maps. In the upper right-most panel of Figure 5.3, the gas masses of three clumps are shown as a function of time (*solid*), demonstrating their rapid formation and disruption. In contrast, the bottom row of Figure 5.3 shows the evolution of the same clump in an experiment where we temporarily turn the wind off. The clump does not disrupt, instead it collapses further and virialises, and subsequently migrates to the galaxy center. This demonstrates that the clumps are destroyed by the wind feedback, and would survive (our equation-of-state is sufficiently soft to allow for this) similarly to previous simulations (Section 5.2) if this feedback was absent.

The reason for the disruption of clumps by the wind is the following. In our model, the wind mass-loading factor (i.e. the outflow rate over the SFR) for $10^{10.5} M_{\odot}$ galaxies at $z = 2$ is $\eta \approx 3$ (Oppenheimer & Davé, 2008), and the velocity ranges between $\approx 350 - 750 \text{ km s}^{-1}$. These wind parameters agree well with recent observational detections of gas outflowing from $z \approx 2$ galaxies (Steidel et al., 2010) and clumps (Genzel et al., 2010). Star-formation in the clumps proceeds on a timescale $T_{SF} \approx 300 \text{ Myr}$ (according to the Kennicutt (1998) relation), thus winds drive gas out of the clumps on a timescale $\approx T_{SF}/\eta \approx 100 \text{ Myr}$, which is comparable to the disk orbital time. The consequence is that the gas surface density in the clumps decreases faster than the rate at which it is replenished by the instability inside the disk, and so clump regions move from $Q \lesssim 1$ to $Q \gtrsim 1$ (and thus stop collapsing) within a time that is shorter than the disk orbital time. The clumps typically convert just about 10% of their peak gas mass into stars, hence the low fractions of ‘clump stars’ and high gas fractions inside the clumps. The short lifetimes we find are consistent with the *upper limits* of $\approx 300 - 500 \text{ Myr}$ based on stellar population modelling (Elmegreen et al., 2009; Förster Schreiber et al., 2010).

Given the masses and sizes of clumps (Table 5.1), their circular velocities are $\sqrt{GM/R} \approx 80 - 100 \text{ km s}^{-1}$. This is significantly larger than the velocity dispersion of the gas within them or their rotational velocities (in particular if the galaxy-wide average velocity gradient is subtracted as ‘background’). Typically the clumps have $v_{rot}^2 + 2\sigma_g^2 \approx 0.6(GM/R)$, or $|U/K| \gtrsim 3$, where U is their gravitational potential energy and K the internal kinetic energy. Thus, they are neither supported by pressure nor by rotation, and in fact they are not virialised. This is due to continuous feedback on a timescale shorter than the dynamical time, that prevents virialisation before disruption.

5.5 Comparison to observations

Figure 5.4 shows mock maps of $H\alpha$ intensity, velocity and velocity dispersion, obtained by converting $L_{H\alpha}[\text{ergs}^{-1}] = 1.26 \times 10^{41} \times \text{SFR}[M_{\odot} \text{ yr}^{-1}]$ (Kennicutt, 1998), ‘placing’ *s224* at $z = 2$, convolving it with a $\text{FWHM} = 0.17''$ resolution, and pasting it into a real SINFONI datacube with pixel scale $0.05''$. This results in realistic resolution and noise properties that correspond to a representative total integration time ($\approx 6 \text{ hours}$) for our high-resolution SINFONI data sets (Förster Schreiber et al., 2009; Genzel et al., 2010).

The clumpiness, smooth velocity field and relatively flat velocity dispersion map (out-

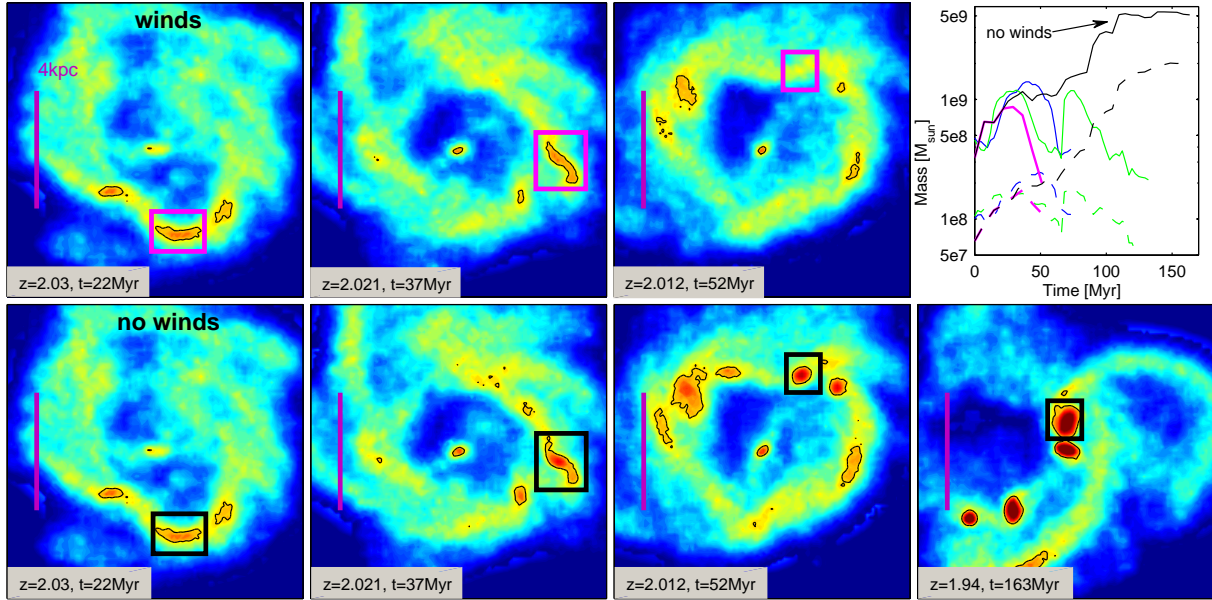


Figure 5.3: A time sequence of gas surface density maps showing the *disruption* of a clump in our model (*Top*), where $t = 0$ (not shown) is the *formation* time of the clump. To demonstrate the role of the wind, we turn it off at $z = 2.03$ and show the alternative evolution of non-disruption, virialisation and migration (*Bottom*). The color coding is as in Figure 5.2(c). The upper right-most panel shows the mass of gas (*solid*) and young (< 50 Myr) stars (*dashed*) for four clumps as a function of time since their formation. The magenta lines are for the clump highlighted on the *Top* and the black for the clump highlighted on the *Bottom*. The jump in mass of the green lines at $t \approx 60$ Myr is a result of a merger between two clumps (not shown in other panels). The typical clump lifetime in the presence of winds is ≈ 50 Myr, and the mass of new-formed stars is approximately 10% of the maximum clump gas mass. The mass of new-formed stars internal to the clump decreases following the decrease of the gas mass, as these stars are dispersed out of the clump when the collapse is halted by the return to $Q > 1$.

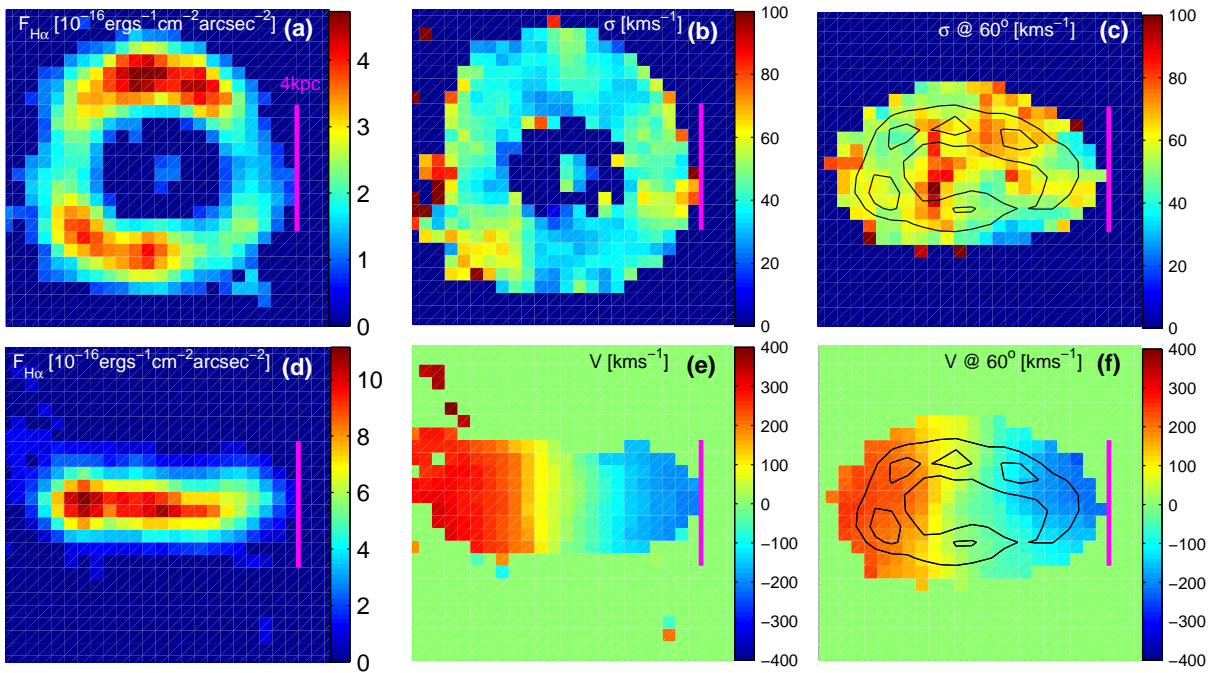


Figure 5.4: Mock $H\alpha$ line observations of the snapshot shown in Figure 5.2, as would be obtained with SINFONI. Face-on (*a*) and edge-on (*d*) line intensity, velocity field shown edge-on (*e*) and at 60° inclination (*f*), and velocity dispersion shown face-on (*b*) and at 60° inclination (*c*). Contours of surface density are overplotted in panels (*c*) and (*f*). See Section 5.5 for discussion.

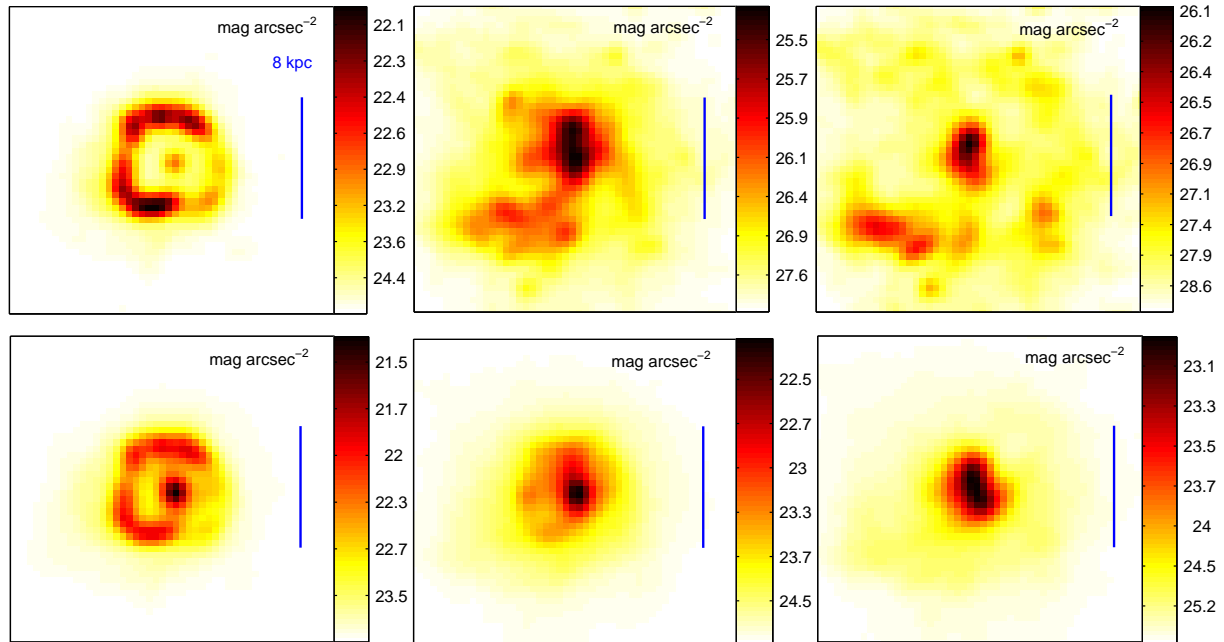


Figure 5.5: Mock continuum observations as would be obtained with the ACS I_{775} filter (*Top*) and with the NICMOS F160W filter (*Bottom*). *Left*: no dust attenuation. *Right*: a probable upper limit on the dust attenuation. *Middle*: an intermediate case. Each panel is 20 kpc on a side. The color axes are linear, and the indicated units are mag arcsec^{-2} (AB).

side the center), which are the characteristics of real SINS clumpy disks, are all well reproduced when ‘observing’ our simulations. The most significant difference to the non-degraded images in Figure 5.2 (the left and middle columns can be directly compared in Figures 5.4 and 5.2) is in the velocity dispersion map. The ‘beam smearing’ increases the apparent velocity dispersion where there are velocity gradients (this is the reason for the diagonal feature of high dispersion in the inclined image in Figure 5.4(c)), and the clumps are no longer seen as clear minima. As a result, the small but present velocity gradients across the clumps get smoothed out. Thus, because of the non-virialised state of the clumps, and their being minima in velocity dispersion, they do not show strong features in observations at the currently available resolution of $\approx 1 - 2$ kpc, even if their masses are dynamically significant. This prediction is consistent with the observations of Genzel et al. (2010).

In Figure 5.5 we show mock continuum images produced using the radiative transfer code SUNRISE (Jonsson, 2006; Jonsson et al., 2010). Shown on the top are rest-frame UV images as would be observed with ACS aboard *Hubble Space Telescope*, and on the bottom mock NICMOS rest-frame optical images (both with a gaussian PSF with FWHM = 1.15 kpc and pixel size of 0.4 kpc, appropriate for NIC2). The different columns bracket possible dust models: on the left there is no dust obscuration, in the middle column most

of the star-forming gas is assumed to be distributed in sub-resolution clumps of negligible cross-section that do not contribute to the absorption (taking the 'cold phase' fraction in the Springel & Hernquist (2003a) model, see Jonsson et al., 2010), and the right column shows images with 'maximal' attenuation, assuming the dust is not clumped at all. In all cases the obtained integrated galaxy colors correspond to the *sBzK* selection criterion for $z \approx 2$ star-forming galaxies (Daddi et al., 2004). Also, the contribution of single clumps to the total light does not exceed $\approx 10\%$ in any of the cases, in agreement with observations (Elmegreen et al., 2009; Förster Schreiber et al., 2010).

However, it is evident that as long as the dust distribution is not well constrained there is very large uncertainty in the appearance of the obtained images (see also Conroy et al., 2010). In the rest-frame UV the absorption can be so strong, due to the large gas column densities ($\gtrsim 10^{23} \text{ cm}^{-2}$), that the star-forming regions where most young stars are distributed become hidden by the dust. The UV emission becomes peaked in regions with low gas surface density and intermediate surface density of young stars, and therefore is predicted not to necessarily correlate with $\text{H}\alpha$ emission.

Rest-frame optical light-to-mass peaks are less pronounced, both due to the smoother distribution of the older stars that are probed by these wavelengths and the lower optical depth compared with the UV. This means that, except from the central region and short phases of 'dying out' clumps that still peak in rest-frame UV emission but no longer pronouncly in $\text{H}\alpha$, the rest-frame optical light is expected to be well aligned with the $\text{H}\alpha$ emission.

The unobscured rest-frame optical emission has a central peak due to the concentration of (older) stars. Observations often show indeed that rest-frame optical light is more concentrated than UV (but see Bond et al., 2010). After considering dust obscuration, the rest-frame optical light becomes even more concentrated due to the stronger absorption in the gas-rich ring. We do not find, in the current sample we have, a case where the rest-frame optical emission does *not* have a local peak at the galaxy center. This is true for all dust models, but stands in disagreement with several observed galaxies (Förster Schreiber et al., 2010).

5.6 Summary and discussion

In this chapter we use 'zoom-in' cosmological hydrodynamical simulations that include a model for fast momentum-driven winds with high mass-loading factors to investigate the formation of star-forming disk galaxies at $z \approx 2$. Our wind model reproduces observed low baryon conversion efficiencies and high gas fractions, and we also find a good kinematical and morphological agreement with observations. In addition, we present an important numerical result, namely that the giant clumps in $z \approx 2$ disks are short-lived and not virialised. This is because they are disrupted by feedback in less than a disk orbital time after they form and before they can reach virial equilibrium. We show that this scenario is plausibly consistent with the available observations.

Our results are in contrast to previous models that did not include fast winds with high

mass-loading factors. Such winds are observed to be ubiquitous in high-redshift galaxies, and in particular they have been recently observed from individual giant clumps. We demonstrate that if we temporarily turn off the winds, we reproduce previous results where clumps are long-lived and migrate to the galaxy centers. However, if the wind is drastically reduced in a self-consistent way, i.e. starting from the initial conditions at high redshift, a gas-rich unstable disk does not develop in the first place and the galaxies have very peaked rotation curves (e.g. Joung et al., 2009). An extensive exploration of parameter space will be described in Genel et al. (in prep.).

Our feedback recipe assumes that gas can be blown out of the clumps and subsequently out of the galaxy at high rates, as observed. It also assumes that star-formation always follows the Kennicutt (1998) relation, resulting in significant star-formation and wind expulsion even before the clump virialises. In the future it will have to be understood how this occurs on sub-clump scales based on improved physical models.

Chapter 6

Summary and prospects

The research presented in this thesis deals with the formation and growth of dark matter halos as well as with the formation and evolution of star-forming galaxies at redshift $z \approx 2$. We have investigated the merger rate of dark matter halos in the Λ CDM cosmological model, and also found and characterized an additional significant component of smooth accretion onto dark matter halos. We have studied theoretical aspects of the processes taking place in massive star-forming disks at $z \approx 2$ by means of cosmological hydrodynamical simulations.

In the Λ CDM model, the process of galaxy formation is deeply connected to the formation of the large-scale structure in the Universe. Since dark matter dominates the mass budget of the Universe, being ≈ 5 times more abundant than "normal" baryonic matter, it is largely collisionless gravitational processes that shape the "cosmic web" of voids, sheets, filaments and halos. This is the "backbone" of galaxy formation. Specifically, galaxies form in the centers of dark matter halos because these are the deepest gravitational potential wells. Gas can either cool and fall from the halo to the galaxy, or be funneled directly to the center of the halo. Stars accumulate both by forming in-situ and by being accreted from smaller galaxies in galaxy mergers. Those processes, the ways baryons make it to galaxies, are deeply connected to the way dark matter halos form. This is the context in which understanding the way dark matter halos gain their mass is important for studying galaxy formation. Therefore, in §2 and §3 we have investigated the two growth modes of dark matter halos: mergers and smooth accretion of mass.

In order to quantify the merger rate of dark matter halos, we first analysed the Millennium Simulation, which is a large N-body cosmological simulation of $\approx 10^{10}$ dark matter particles. We realised that in order to achieve a reliable and self-consistent measure, complicated dynamical effects occurring during mergers have to be taken into account. Specifically, the merging of dark matter halos is not a one-way process if it is not carefully defined: small halos may enter (and then escape) the virial radius of larger halos several times before the final coalescence. This is also related to the well-known tendency of the Friends-of-friends (FOF) halo finder to sometimes bridge between different halos and spuriously, temporarily, connect them into one group. Both effects mean that FOF catalogues cannot simply be used as halo catalogues for studying the merger rate. Therefore, we

constructed a novel algorithm to build merger trees, where temporarily-connected halos are split and a merger is only a one-way process. Such merger trees are termed "splitting" trees. This algorithm is to be compared with alternatives such as "snipping" or "stitching", where repeated mergers may be counted more than once. While the dynamical effects of the repeating mergers (or fly-bys) are interesting, as far as the question of mass growth is concerned, it is important not to count a merger between the same two objects more than once; otherwise one may overestimate of the abundance and mass contribution of such events.

Using the "splitting" trees, we quantified the merger rate of dark matter halos as a function of their mass, the redshift of the merger, and the merger mass ratio. We found that over large ranges of these variables, the merger rate can be fit by a simple form that is separable in those variables. The redshift dependence of the merger rate (per halo, rather than per unit volume) is strong and goes approximately like $(1+z)^2$. This means, for example, that the merger rate at $z=2$ is a scaled-up version of that at $z=1$, with the same relative abundances of mergers of different mass ratios, such as major and minor mergers. This redshift evolution is faster than that of the Hubble time, which means that the number of mergers per Hubble time is higher at higher redshift. In fact, at $z \approx 1$, the mean time elapsed between major mergers (mass ratio $< 3:1$) becomes shorter than the Hubble time. The mass dependence, on the other hand, is relatively weak, but still significant over many orders of magnitude. The merger rate scales approximately as $M^{0.1}$, such that a halo of $10^{14} M_{\odot}$ undergoes mergers ≈ 4 times more frequently than a $10^9 M_{\odot}$ halo. The mass ratio dependence of the merger rate is such that major mergers are relatively rare compared to minor mergers.

When rare halos are investigated, those halos above the "knee" of the mass function, it becomes important to distinguish between two different quantities: the probability that such a halo has just experienced (in other words, formed by) a merger and its probability to undergo a merger in some small time interval in the future. This distinction is analogous to the two observational methods for detecting mergers: by disturbed morphologies (past mergers) and by pair counting (future mergers). We have, for the first time, shown that the merger rate per progenitor halo (that is related to future mergers) is smaller than that per descendant halo, and that their redshift and mass dependencies are different. We also provided an analytic formula that allows a conversion between the quantities, provided that the halo mass function is known (Appendix A).

Galaxy mergers are related to dark matter halo mergers, albeit not in a straight-forward way. When a pair of dark matter halos cross each other's virial radii on their way to mix and merge, the processes operating on the galaxies in their centers may be different from those operating on the halos themselves. For example, ram pressure stripping can cause small satellites falling into massive halos to lose their gas faster than collisionless material. On the other hand, the galaxies are more compact than the halos and so they may stay intact for a longer time before they eventually merge. Therefore, making the connection between halo mergers and galaxy mergers in SAM or HOD models requires care. In Appendix B we have shown that halo mergers can only be followed for a short time if the halos are not very well resolved. In other words, small halos are stripped and lose their identity

during mergers in a way that depends on how well they are resolved more than on the physical merger timescale. This may create biases (overestimate or underestimate) of the true merger time, depending on the model.

Future work will make steps forward in modeling the galaxy merger rate via direct modeling of galaxies in the cosmological context. This can be done nowadays either with full hydrodynamical cosmological simulations that model star-formation and additional baryonic processes, or by semi-analytical models based on dark matter halo merger trees. It will probably still take a while before full hydrodynamical simulations will give an accurate description of galaxy formation, due to the complexity of the physics that is involved. Thus, the role of SAM or HOD models, which rely on modeling of dark matter halos growth, will remain important in the foreseeable future.

The analysis of the "splitting" trees of the Millennium Simulation shows that only $\approx 50\%$ of the mass halos accrete during their growth arrives in resolved mergers. To understand better to what extent this result depends on resolution, we have applied our analysis to the Millennium-II Simulation, which has a 125 times better mass resolution. The result was striking: even for the best-resolved halos, where mergers of mass ratios $10^5 : 1$ can be resolved, the share of mergers in their mass growth does not exceed $\approx 60\%$. Moreover, the functional form of the fit to the merger rate, which is a simple power-law for minor mergers, suggests that the merger contribution saturates at that value, i.e. minor mergers are numerous but contribute negligible mass. To verify this result in a more robust way that is not dependent on merger tree construction algorithms, we turned to additional N-body simulations and analysed their full particle history. We found that indeed most halos are made mostly of particles that never previously belonged to other halos, i.e. particles are accreted "smoothly", rather than in bound units. When the best-resolved halos are considered, as well as the resolution-dependent trends, the conclusion from the merger trees analysis is confirmed.

The resolution of the simulations we considered is still limited (as is the case for any simulation), and so our findings should be continuously tested with future higher resolution simulations. Today, the higher resolution Aquarius Simulations already strengthened our conclusions (albeit with a small sample of 6 halos). With increasing dynamic range, resolution of more and more minor mergers will shed light on the role of true smooth accretion in dark matter halos growth. Nevertheless, it is interesting to consider that the Millennium-II Simulation is already able to resolve small halos of $10^8 M_\odot$. Those are arguably not able to hold their cosmic share of baryons under the cosmic ionising background radiation due to their low virial temperatures. If this is true, then the implications of our study on baryons are independent of possible future discoveries as for the smoothness of the dark matter accretion. Only gas associated with halos that *are* resolved in the Millennium-II Simulation is expected to be bound to its halo, and the rest should arrive smoothly.

Over the past decade there have been tremendous advances in the research of the high-redshift Universe, both observationally and theoretically. Star-forming galaxies at $z \approx 2$ are now regularly selected by broadband photometric methods and studied in a range of wavelengths from the rest-frame UV to FIR, as well as by spectrally resolved nebular line emission, and can be spatially resolved both by ground-based and space borne telescopes.

Fundamental properties of $z \approx 2$ star-forming galaxies are that their star-formation rates are very high and their morphologies irregular. Spatially resolved broadband imaging finds complex morphologies for $z \approx 2$ galaxies both in rest-frame UV and optical light. The SINS survey includes a sample of ≈ 100 star-forming $z \approx 2$ galaxies that are observed with SINFONI/VLT to trace the $H\alpha$ and other emission lines, resolving the galaxies both spatially and spectrally. That galaxy sample can be divided into three classes of similar proportions: mergers, disks, and dispersion-dominated systems. While the nature of the latter is not yet well established, the most ground-breaking results of the SINS survey are based on the observations of the disk class. It was found that star-formation rates of $\approx 100 M_{\odot} \text{ yr}^{-1}$ can take place at that cosmological epoch not only during mergers but rather in large disks that exhibit regular ordered rotation. Those disks, however, are different from local disk galaxies in several aspects. The gas fractions are very high ($\approx 40\%$), the random motions of the gas as traced by the velocity dispersion is also much higher compared with the local Universe ($\approx 30 - 100 \text{ km s}^{-1}$), and they contain "giant clumps" of $\approx 1 \text{ kpc}$ in size and up to $\approx 10^{10}$ in mass.

Much progress has been made in the past few years in the theoretical understanding of those systems. First, it was realized that the high star-formation rates are a natural consequence of the high growth rates of dark matter halos at that epoch. To show that (in §4), we used our analysis of the Millennium Simulation to quantify the instantaneous growth rate of dark matter halos, and found that even non-merging halos have growth rates that are high enough to explain the high star-formation rates. This is under the assumption of high-efficiency "cold mode" of accretion, where most of the gas that comes in along the cosmic filaments makes it to the central galaxy as fuel for star-formation. We also followed the merger trees to $z = 0$ and investigated the varied fates of the halos that probably host those galaxies. It was found that a significant fraction of them is not expected to undergo major mergers all the way to $z = 0$. Therefore, internal processes (as well as minor mergers and smoother accretion) probably play an important role in shaping the descendants of those galaxies in the local Universe.

While the high star-formation rates and high gas fractions in $z \approx 2$ disks are explained by the high external accretion rates, the clumpy morphologies are thought of nowadays as a result of internal processes. In particular, it has been suggested that the high gas fractions and high random motions work together to make the disks gravitationally (marginally) unstable with (turbulent) Jeans scales much larger than in the local Universe. The Jeans lengths and masses calculated for this class of galaxies match the giant clumps that are observed in them. An open question that is being given much attention in the literature nowadays is whether those giant clumps live long enough to transform a large fraction of their gas into stars and/or fall via dynamical friction to the galaxy center and contribute to bulge buildup.

In §5 we presented a large computational project of simulations with "zoom-in" initial conditions that focus with high resolution on the formation of individual $z \approx 2$ halos inside a cosmological box. We used a version of the N-body/SPH code GADGET-2 that includes a momentum-driven wind model. In these simulations, rapidly star-forming gas-rich disks indeed form. We have developed tools for comparing the simulated galaxies directly to

observations by using the radiative transfer public code SUNRISE, and by creating mock SINFONI/VLT datacubes with realistic "observing conditions". We find good agreement between the "observed" simulated galaxies and real observed galaxies, in terms of their luminosities, colors, morphologies and kinematics. With this comparison, we conclude that the galaxies formed in the simulations are plausibly realistic.

An important ingredient of our model is the strong galactic winds generated by star-formation, which have large mass loading factors, i.e. the mass outflow rate out of star-forming galaxies is typically larger than the star-formation rate inside the galaxies. Such winds are ubiquitously observed at all redshifts. In particular, new observations detect such winds from individual "giant clumps". We have investigated the impact of the winds on the giant clumps in the simulations, and found that the high mass loading factor winds do not allow the clumps to virialise, as mass is removed from them on timescales shorter than the dynamical time of the disk. Within roughly half a disk orbital time, the clumps lose a fraction of their mass such that they stop collapsing and disrupt. Thus, their lifetimes are short and they do not migrate to the galaxy centers.

In the future, we will expand our simulation project in order to achieve several further goals. First, to investigate halos with a variety of formation histories, so that the relation between the formation history of the halo and the properties of its central galaxy can be studied. Second, to broaden the comparison with observed galaxies to a statistically significant one. Third, to deepen the study of parameter space and resolution. An additional scientific question that will require further investigating, which is possible with our simulations, is the origin of the large random motions observed at high redshift. A few ideas have been proposed in the literature, such as feedback from star-formation, gravitational instabilities, or external accretion, but little work was done in the full cosmological context.

It appears, both from theoretical considerations and from observational evidence, that star-formation feedback, and in particular galactic winds, play an important role in galaxy formation, and in particular in the formation and evolution of $z \approx 2$ star-forming disks. Nevertheless, galactic winds are notoriously difficult to model, and our own implementation is based on simple prescriptions, which, from a critical point of view, may be viewed as unrealistic. Future progress is expected in understanding star-formation feedback and the generation of galactic winds, with the increasing sophistication of numerical simulations. Such progress will push forward our understanding of high-redshift galaxies and make it more complete than ever before.

Appendix A

The merger rate per halo equals, in general, the number of merger events divided by the number of halos undergoing those mergers. Let us denote by $r_d(z_d, M, x)dMdx$ the number of mergers¹ that occur between z_p and z_d , whose descendant mass is $M \pm dM/2$ and ratio is $x \pm dx/2$. Similarly the number of mergers whose more massive progenitor mass is $M \pm dM/2$ and ratio is $x \pm dx/2$ are denoted as $r_p(z_p, M, x)dMdx$, and accordingly for the less massive progenitor: $r_{p2}(z_p, M, x)dMdx$. We will define the halo mass function in the following way: if $n(z, > M)$ is the number of halos more massive than M at redshift z , then the number of halos in the interval $M \pm dM/2$ is $\frac{dn(z, > M)}{dM}dM \equiv N_h(z, M)dM$. For simplicity, in the following derivation we assume the binary merger approximation. As shown below, the analytic formula we derive reproduces well the numerical results, therefore we conclude that for this matter, this approximation is not significant.

Without loss of generality, we may assume $dM \gg Mdx$, therefore the progenitor masses of mergers whose descendant mass is $M \pm dM/2$ and ratio is $x \pm dx/2$ are $M_1 \pm dM_1/2 \equiv \frac{x}{x+1}(M \pm dM/2)$ and $M_2 \pm dM_2/2 \equiv \frac{1}{x+1}(M \pm dM/2)$. Therefore, $r_d(z_d, M, x)dMdx$ is also exactly the number of mergers whose more massive progenitor mass is $M_1 \pm dM_1/2$ and ratio is $x \pm dx/2$, as well as the number of mergers whose less massive progenitor mass is $M_2 \pm dM_2/2$ and ratio is $x \pm dx/2$. Therefore we can write the equalities

$$\begin{aligned} r_d(z_d, M, x)dMdx &= r_p(z_p, M_1, x)dM_1dx \\ r_d(z_d, M, x)dMdx &= r_{p2}(z_p, M_2, x)dM_2dx. \end{aligned} \quad (\text{A.1})$$

The number of mergers *per descendant halo*, whose descendant mass is $M \pm dM/2$ and ratio is $x \pm dx/2$, is simply

$$R_d(z_d, M, x)dx = r_d(z_d, M, x)dMdx/N_h(z_d, M)dM, \quad (\text{A.2})$$

and similarly the number of mergers *per progenitor halo*, whose more massive progenitor mass is M_1 and ratio is $x \pm dx/2$, is

$$\begin{aligned} R_p(z_p, M_1, x)dx &= r_p(z_p, M_1, x)dx/N_h(z_p, M_1) \\ &= r_d(z_d, M, x)\frac{dM}{dM_1}dx/N_h(z_p, M_1) \\ &= R_d(z_d, M, x)N_h(z_d, M)\frac{dM}{dM_1}dx/N_h(z_p, M_1), \end{aligned} \quad (\text{A.3})$$

¹Per unit time or redshift and possibly per unit volume. This has no significance for this derivation, as long as it is kept consistent throughout.

where equations (A.1) and (A.2) were used in the first and second equalities, respectively. Scaling the mass from M_1 to M , we finally arrive at

$$R_p(z_p, M, x) = R_d(z_d, \frac{x+1}{x}M, x) \frac{x+1}{x} N_h(z_d, \frac{x+1}{x}M) / N_h(z_p, M), \quad (\text{A.4})$$

which is the relation between the merger rate per more-massive-progenitor halo and the merger rate per descendant halo.

In an analogous way, the merger rate per less-massive-progenitor halo is

$$R_{p2}(z_p, M, x) = R_d(z_d, (x+1)M, x) (x+1) N_h(z_d, (x+1)M) / N_h(z_p, M), \quad (\text{A.5})$$

but in order to correspond to $x < 1$ ratios as defined in §2.3.3 we define $R_p(z_p, M, x < 1)dx = R_{p2}(z_p, M, \frac{1}{x})d\frac{1}{x}$, therefore

$$R_p(z_p, M, x < 1) = R_d(z_d, (\frac{1}{x} + 1)M, \frac{1}{x}) (\frac{1}{x} + 1) N_h(z_d, (\frac{1}{x} + 1)M) x^{-2} / N_h(z_p, M). \quad (\text{A.6})$$

Equations (A.4) & (A.6) construct the merger rate per progenitor halo as defined in §2.3.3 from the merger rate per descendant halo, and can be applied regardless of the source of the given merger rate per descendant halo.

In order to compare the two quantities, it is more convenient to examine equation (A.4), because both definitions of the merger rate are quantified in its validity range, i.e. $x > 1$. The largest source of difference is the term $N_h(z_d, \frac{x+1}{x}M) / N_h(z_p, M)$. For M smaller than the knee of the mass function, where it is roughly a power law with M , this term is constant with M for a given x , i.e. the trend of the merger rate with mass stays the same. As opposed to that, where the mass function begins to drop exponentially, this term decreases exponentially with M as well, and therefore so does R_p/R_d .

For completeness we show also how the merger rate per descendant halo can be derived from the merger rate per progenitor halo:

$$\begin{aligned} R_d(z_d, M, x) &= R_p(z_p, (\frac{x}{x+1})M, x) \frac{x}{x+1} N_h(z_p, (\frac{x}{x+1})M) / N_h(z_d, M) \\ &= R_p(z_p, \frac{M}{x+1}, \frac{1}{x}) \frac{x^{-2}}{x+1} N_h(z_p, (\frac{M}{x+1})) / N_h(z_d, M), \end{aligned} \quad (\text{A.7})$$

as well as how the two regimes of the merger rate per progenitor halo are related to one another:

$$R_p(z_p, M, x) = R_p(z_p, \frac{M}{x}, \frac{1}{x}) x^{-3} N_h(z_p, \frac{M}{x}) / N_h(z_p, M). \quad (\text{A.8})$$

Appendix B

In principle it would be desirable to identify the end point of mergers based on the simulation itself, rather than use a calibrated recipe based on other simulations, as we do in §4.3.2. In the following we show that a reliable identification of the end point of mergers cannot be achieved using the Millennium simulation merger trees.

Here we briefly review several results from the literature regarding merger time scales and substructure disruption. When a halo becomes a substructure in a bigger halo, it is subject to stripping of its mass and decay of its orbit, both under the influence of tidal forces. Substructures in major mergers are expected to sink on a dynamical time scale to the halo center, and violently merge and relax. Minor mergers are expected to last on a dynamical friction time scale, which is longer for ever more minor mergers (very roughly linearly proportional to the mass ratio), since the tidal interaction becomes less and less efficient. Such substructures are expected to experience an approximately exponential mass loss (Giocoli et al., 2008) and orbit the halo center several times (e.g. Boylan-Kolchin et al., 2008). There is no time scale dependence expected on absolute mass.

Now we turn to defining the end of mergers based on the Millennium simulation merger trees. Once two halos have started merging according to the definition in §4.3.2, they are identified as several (≥ 2) SUBFIND structures (subhalos) within the same FOF group, two of which are the descendants of the main subhalos of the original merging FOF groups. Therefore, a straight-forward approach towards determining the end point of the merger would be to consider the time when the two “main” subhalo descendants merge to become one subhalo and cannot be distinguished anymore. In the following we will refer to this time as the “end point” of the merger.

Defining the end point of the merger in this way introduces an artificial dependence on the mass of the smaller original component of the merger (M_{sec}): the higher M_{sec} , the longer it takes the descendant substructure to reach the lower threshold needed for identification of subhalos (20 bound particles), i.e. the longer it takes it to “disappear” inside the merged FOF group and merge with the other descendant subhalo. The left column in Figure B.1 demonstrates this phenomenon by comparing mergers with different M_{sec} while keeping the mass ratio fixed inside the narrow bin $8 < x < 12$. The top left panel shows the inferred merger durations as a function of redshift and its dependence on M_{sec} . The dependence

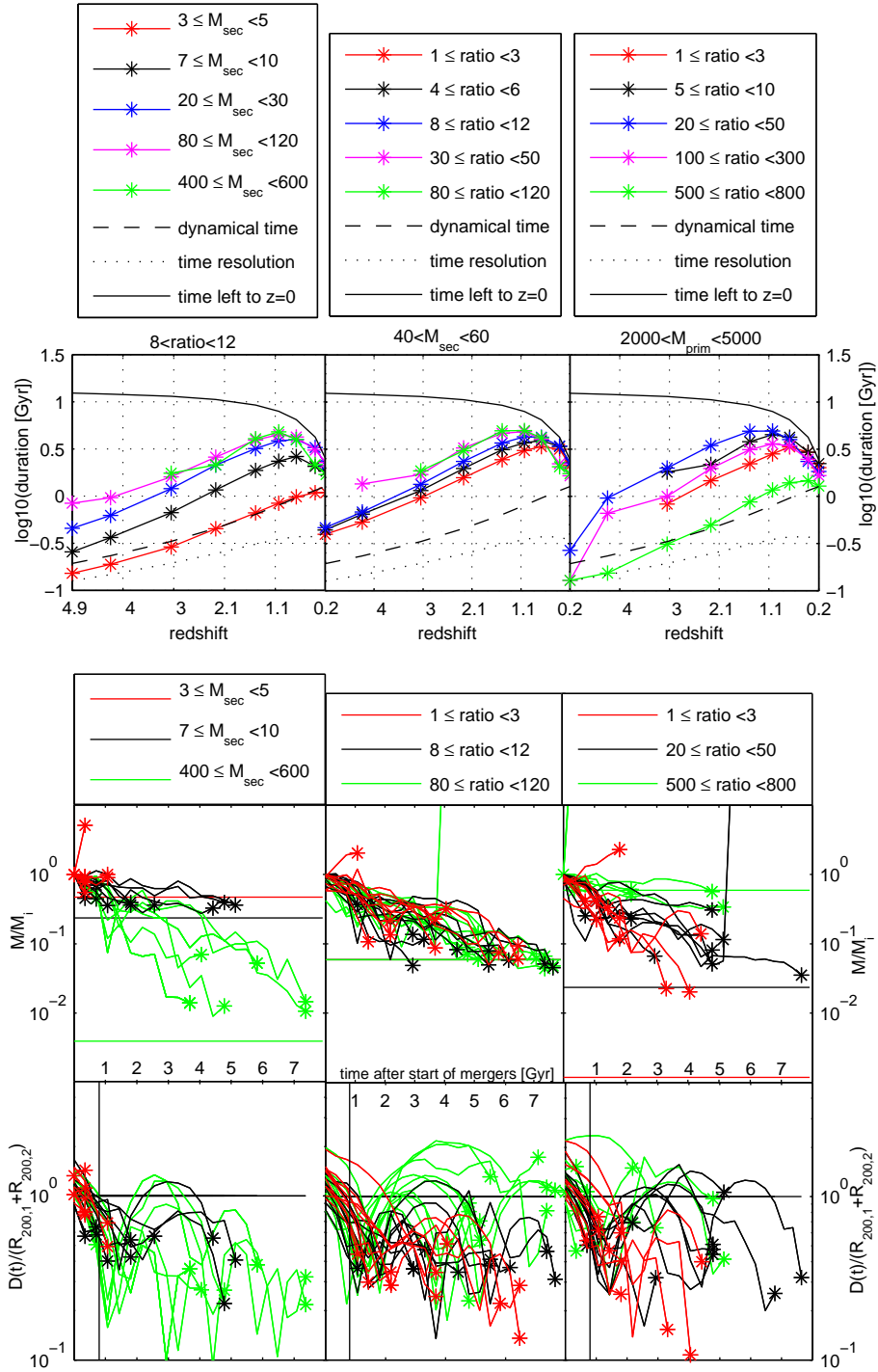


Figure B.1: Substructure mass and spatial evolution and merger durations based purely on the simulation. All masses are in units of $10^{10} M_{\odot}$.

on redshift follows the dynamical time ($\tau_{\text{dyn}} = 0.1H^{-1}$, *dashed*), as expected¹, while there is a strong undesired mass dependence - at $M_{\text{sec}} \lesssim 2 \times 10^{11} M_{\odot}$ mergers with smaller M_{sec} end more rapidly. For $M_{\text{sec}} \gtrsim 2 \times 10^{11} M_{\odot}$ the time scale converges with respect to M_{sec} .

The middle and bottom left panels may help clarifying this trend: they show the evolution with time of the descendant subhalo of the smaller component of 10 random mergers that started at $z \approx 1.1$, all in the same ratio bin as in the top panel, and similarly divided into M_{sec} bins. The curves in the middle left panel follow the mass of the subhalo, normalised by its original mass M_{sec} , until the end point of the merger, where each curve is marked with an asterisk at its end for emphasis. The horizontal lines show the minimum halo mass (20 particles) normalised by the largest M_{sec} possible in each bin, i.e. a mass evolution curve that reaches the corresponding horizontal line has been stripped down to the lowest possible detectable subhalo mass. The result is that the curves tend to end close to their mass limit, therefore the curves that describe higher M_{sec} are longer also in the time axis. The curves in the bottom left panel follow the time evolution of the normalised spatial separation presented in §4.3.2, assuming the virial radii don't change with time. Comparing the orbits of the different mass bins, no fundamental difference appears: it is not that mergers end when they are closer than some threshold to the halo center - they all show a similar behaviour, but are “abruptly” cut because they arrive to the mass threshold shown in the middle panel.

We now move to examine whether our end point definition is able to reproduce the expected, approximately linear, trend of merger durations with mass ratio. In order to avoid the resolution problem at low masses, we keep M_{sec} constant and well inside the convergent range in the top left panel, and change the mass ratio by increasing the mass of the other merger component (M_{prim}). We do find that higher mass ratio mergers take longer to end, as shown in the middle top panel in Figure B.1, but the dependence is roughly $\propto x^{0.15}$, which is much weaker than expected. Again, by examining the middle and bottom panels in the middle column the picture becomes clearer: there is almost no difference, in both the mass and spatial evolutions, between mergers in the different mass ratio bins. The distance between the subhalos decreases indeed somewhat faster for more intense mergers, but it is the common mass threshold that cuts the mergers after almost the same mean duration. We believe that the less intense mergers are cut too early because of stripping that brings them below the mass resolution.

Finally, the right column in Figure B.1 shows both dependencies combined by keeping a constant M_{prim} and examining different mass ratio bins (i.e. different M_{sec} bins). Starting from major mergers and increasing the mass ratio, the mergers become longer, because the subhalos are able to emerge back to the outskirts of the halo after sinking close to the center (bottom right panel). When increasing the mass ratio even more, and by that arriving at low enough M_{sec} , the mergers are cut very rapidly by the mass limit (middle right panel).

¹At $z \lesssim 1$ the lookback time, i.e. the time left until the end of the simulation (*black, solid*) becomes comparable to the mean duration, therefore the long durations tail of the distribution is significantly cut, and the mean is not meaningful anymore.

We have performed the same tests using another definition for the end of mergers: the total mass that belonged to the smaller FOF group at the start point (not only its main subhalo) is followed through time, and the end point is defined as the time when 50% of it was no longer bound to its original subhalos. Since this corresponds roughly to placing a constant threshold at 50% in the middle row panels in Figure B.1, it is clear why such a definition reduces significantly the M_{sec} dependence of the merger durations. Nevertheless, the mass ratio dependence becomes even weaker, because these are the processes that take place after a significant mass loss and near the center, which are even more missed out using this definition.

It can be seen in the bottom panels of Figure B.1 that the normalised separation between the subhalos at the end point of mergers is practically always > 0.1 . Figure B.2 shows the detailed distribution of the final normalised separations as a function of redshift and mass. Indeed, the typical final normalised separation is $0.5 - 1$, and only a very small fraction of the subhalos are identified at small distances compared to the virial radii before their track is lost. No dependence on mass ratio or on M_{prim} was found, but mergers in which M_{sec} is small (*dashed*) tend to end in significantly larger separations compared with mergers with a larger M_{sec} (*solid*). This shows that such mergers are biased towards too early an end point.

The discussion thus far was based on mergers whose end point occurs at $z \geq 0$, but there are also mergers whose descendant subhalos never merge but rather stay distinct subhalos inside the merged FOF group until the last snapshot of the simulation. Figure B.3 shows that the fraction of those so-called open-ended mergers depends on M_{prim} , M_{sec} and the ratio between them in the same way as the merger durations do - the longer the mean duration is, the higher is the fraction of open-ended mergers. This is another disadvantage of a cosmological simulation such as the Millennium compared to detailed simulations of isolated mergers in deriving merger durations or other properties - the simulation is cut at $z = 0$ and therefore a significant fraction of mergers are not complete within its time span.

So far our discussion about the merger durations focused on the trends with redshift, mass and mass ratio. When considering the absolute durations we find, two interesting cases arise. First, there are mergers whose duration is shorter than the dynamical time. Those are especially low M_{sec} major mergers. This is not surprising given the above discussion, but it is another evidence that such mergers are cut too early. Second, major mergers between high masses, as shown for example in red in the middle and right columns of Figure B.1, can last several dynamical times, much longer than expected from violent major mergers. It would be interesting to understand this finding using a more comprehensive work focused on different ways of defining merger end points.

We conclude that SUBFIND does not allow following the substructures within FOF groups, which are the tracers of on-going mergers, until their true merger with the background halo.

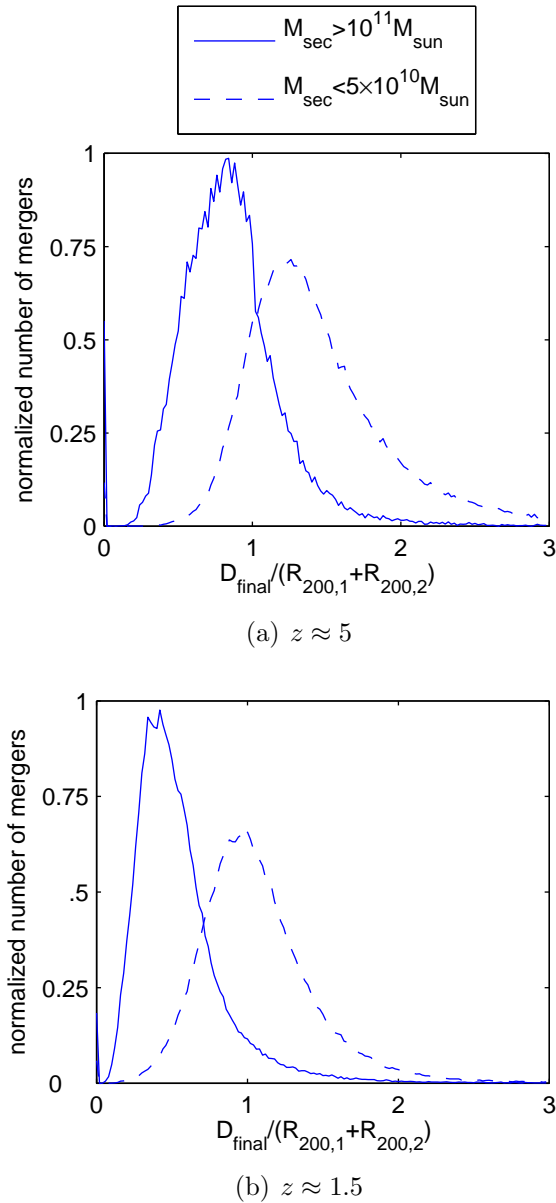


Figure B.2: Distributions of the spatial separations between halos at their end point (D_{final}) normalised for each merger by the sum of the virial radii of the pair ($R_{200,1} + R_{200,2}$), shown at high redshift (*Top*) and low redshift (*Bottom*). It is evident that even at the last point where two substructures are detected by SUBFIND, they are still significantly distant. Two mass bins are shown: in mergers where $M_{sec} < 5 \times 10^{10} M_{\odot}$ (*dashed*) the substructure tends to be lost at higher normalised separations than in mergers where $M_{sec} > 10^{11} M_{\odot}$ (*solid*). The difference between the two redshifts is due to the smaller contrast in the density field in the Universe at higher redshift, because of which structures are less distinguished from their environment.

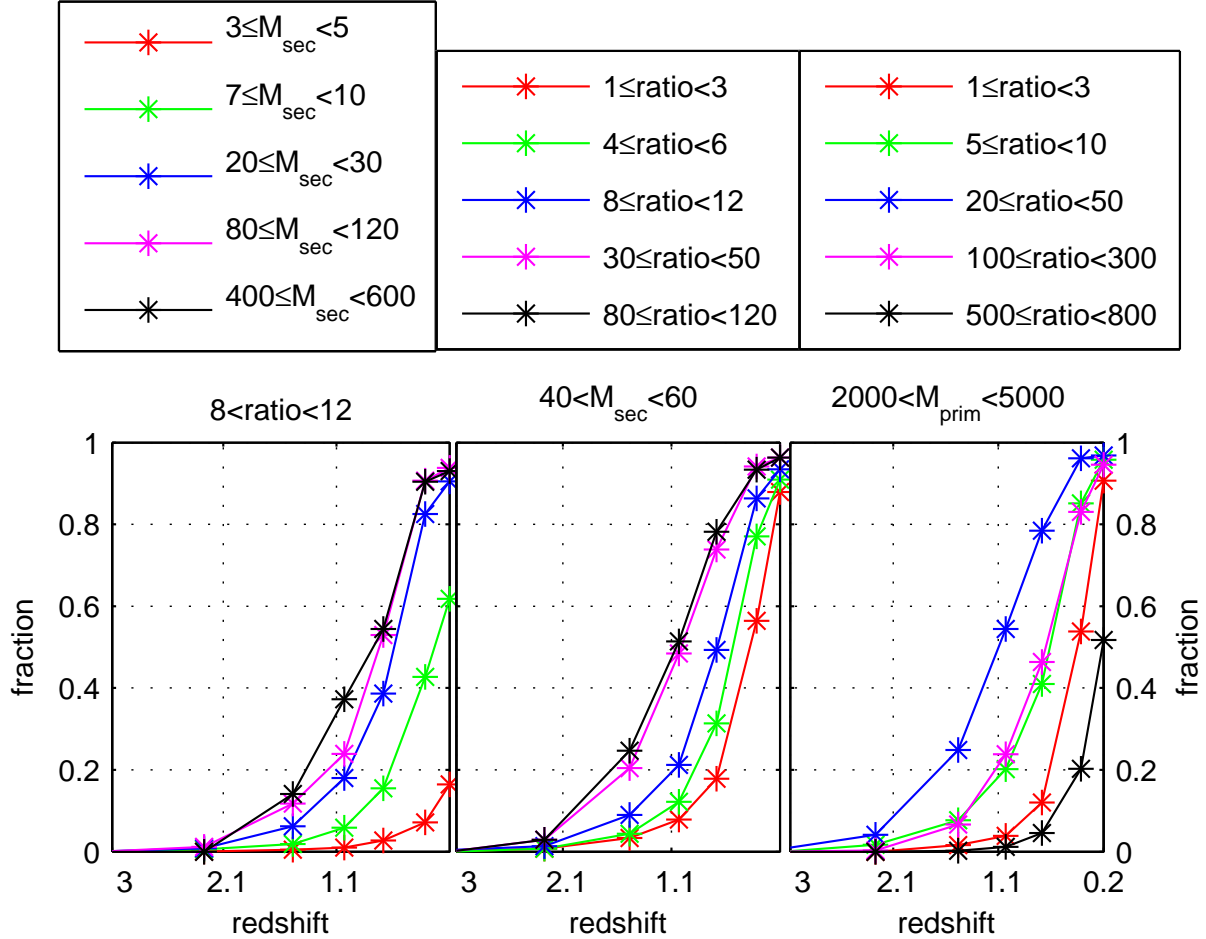


Figure B.3: The fraction of mergers which are 'open-ended', i.e. that start with the merger of two FOF groups at the redshift indicated on the x-axis but where the main subhalos descendants remain distinct inside the merged FOF group until $z = 0$. This fraction becomes significant roughly at $z \approx 1$, and is strongly dependant on M_{prim} , M_{sec} (all masses are in units of $10^{10} M_{\odot}$) and the ratio between them in the same way the mergers' durations do (Figure B.1, top panels). These open-ended mergers lie at the tail of long durations of the duration distribution, but the proximity to the end of the simulation does not allow to follow them to their end point, and therefore it is impossible to properly sample the duration distribution at low redshift.

Bibliography

- Abadi, M. G., Navarro, J. F., Steinmetz, M., & Eke, V. R. 2003, *ApJ*, 591, 499
- Abraham, R. G., Tanvir, N. R., Santiago, B. X., Ellis, R. S., Glazebrook, K., & van den Bergh, S. 1996, *MNRAS*, 279, L47
- Adelberger, K. L., Steidel, C. C., Shapley, A. E., Hunt, M. P., Erb, D. K., Reddy, N. A., & Pettini, M. 2004, *ApJ*, 607, 226
- Agertz, O., Teyssier, R., & Moore, B. 2009, *MNRAS*, L263+
- . 2010, *MNRAS*, 1527
- Angulo, R. E., Lacey, C. G., Baugh, C. M., & Frenk, C. S. 2009, *MNRAS*, 399, 983
- Angulo, R. E., & White, S. D. M. 2010, *MNRAS*, 401, 1796
- Aumer, M., Burkert, A., Johansson, P. H., & Genzel, R. 2010, *ApJ*, 719, 1230
- Bagla, J. S. 2005, *Current Science*, 88, 1088
- Barnes, J. E. 1988, *ApJ*, 331, 699
- Barnes, J. E., & Hernquist, L. 1992, *ARA&A*, 30, 705
- Barnes, J. E., & Hernquist, L. E. 1991, *ApJL*, 370, L65
- Baugh, C. M. 2006, *Reports on Progress in Physics*, 69, 3101
- Baugh, C. M., Cole, S., Frenk, C. S., & Lacey, C. G. 1998, *ApJ*, 498, 504
- Bell, E. F. et al. 2006a, *ApJ*, 640, 241
- Bell, E. F., Phleps, S., Somerville, R. S., Wolf, C., Borch, A., & Meisenheimer, K. 2006b, *ApJ*, 652, 270
- Benson, A. J. 2010, *Physics Reports*, 495, 33
- Benson, A. J., & Bower, R. 2010, *MNRAS*, 405, 1573
- Berger, M. J., & Olinger, J. 1984, *Journal of Computational Physics*, 53, 484
- Bertone, S., & Conselice, C. J. 2009, *MNRAS*, 396, 2345
- Bertschinger, E. 1998, *ARA&A*, 36, 599
- Binney, J., & Tremaine, S. 1987, *Galactic dynamics* (Princeton, NJ, Princeton University Press, 1987, 747 p.)
- Birnboim, Y. 2009, *ApJL*, 702, L101
- Birnboim, Y., & Dekel, A. 2003, *MNRAS*, 345, 349
- Blake, C., & Glazebrook, K. 2003, *ApJ*, 594, 665
- Blumenthal, G. R., Faber, S. M., Primack, J. R., & Rees, M. J. 1984, *Nature*, 311, 517

- Bond, J. R., Cole, S., Efstathiou, G., & Kaiser, N. 1991, *ApJ*, 379, 440
- Bond, J. R., & Efstathiou, G. 1984, *ApJL*, 285, L45
- Bond, N. A., Gawiser, E., & Koekemoer, A. M. 2010, *ApJ*, submitted (astro-ph/10101525)
- Bouché, N. et al. 2007, *ApJ*, 671, 303
- . 2010, *ApJ*, 718, 1001
- Bournaud, F. et al. 2008, *A&A*, 486, 741
- Bournaud, F., & Elmegreen, B. G. 2009, *ApJL*, 694, L158
- Bournaud, F., Elmegreen, B. G., & Elmegreen, D. M. 2007, *ApJ*, 670, 237
- Bournaud, F., Elmegreen, B. G., & Martig, M. 2009, *ApJL*, 707, L1
- Bournaud, F., Jog, C. J., & Combes, F. 2005, *A&A*, 437, 69
- Bower, R. G. 1991, *MNRAS*, 248, 332
- Boylan-Kolchin, M., Ma, C.-P., & Quataert, E. 2008, *MNRAS*, 383, 93
- Boylan-Kolchin, M., Springel, V., White, S. D. M., Jenkins, A., & Lemson, G. 2009, *MNRAS*, 398, 1150
- Brook, C. B. et al. 2010, *MNRAS*, submitted (astro-ph/10101004)
- Brooks, A. M., Governato, F., Booth, C. M., Willman, B., Gardner, J. P., Wadsley, J., Stinson, G., & Quinn, T. 2007, *ApJL*, 655, L17
- Bryan, G. L., & Norman, M. L. 1997, in *Astronomical Society of the Pacific Conference Series*, Vol. 123, *Computational Astrophysics; 12th Kingston Meeting on Theoretical Astrophysics*, ed. D. A. Clarke & M. J. West, 363–+
- Bundy, K., Fukugita, M., Ellis, R. S., Kodama, T., & Conselice, C. J. 2004, *ApJL*, 601, L123
- Burkert, A. et al. 2010, *ApJ*, in press (astro-ph/09074777)
- Burkert, A., & Lin, D. N. C. 2000, *ApJ*, 537, 270
- Burkert, A., Naab, T., Johansson, P. H., & Jesseit, R. 2008, *ApJ*, 685, 897
- Carswell, R. F., & Strittmatter, P. A. 1973, *Nature*, 242, 394
- Cen, R. 1992, *ApJS*, 78, 341
- Cen, R., & Ostriker, J. P. 1992, *ApJL*, 399, L113
- . 2006, *ApJ*, 650, 560
- Cen, R., Phelps, S., Miralda-Escude, J., & Ostriker, J. P. 1998, *ApJ*, 496, 577
- Ceverino, D., Dekel, A., & Bournaud, F. 2010, *MNRAS*, 404, 2151
- Chakrabarti, S., & Blitz, L. 2009, *MNRAS*, 399, L118
- Chandrasekhar, S. 1943, *ApJ*, 97, 255
- Choi, J., Weinberg, M. D., & Katz, N. 2009, *MNRAS*, 400, 1247
- Clowe, D., Gonzalez, A., & Markevitch, M. 2004, *ApJ*, 604, 596
- Cohn, J. D., Bagla, J. S., & White, M. 2001, *MNRAS*, 325, 1053
- Cohn, J. D., & White, M. 2008, *MNRAS*, 385, 2025
- Cole, S., Aragon-Salamanca, A., Frenk, C. S., Navarro, J. F., & Zepf, S. E. 1994, *MNRAS*, 271, 781

- Colless, M. et al. 2001, *MNRAS*, 328, 1039
- Conroy, C., Shapley, A. E., Tinker, J. L., Santos, M. R., & Lemson, G. 2008, *ApJ*, 679, 1192
- Conroy, C., White, M., & Gunn, J. E. 2010, *ApJ*, 708, 58
- Conselice, C. J. 2003, *ApJS*, 147, 1
- . 2006, *ApJ*, 638, 686
- Conselice, C. J., & Arnold, J. 2009, *MNRAS*, 397, 208
- Conselice, C. J., Bershad, M. A., Dickinson, M., & Papovich, C. 2003, *AJ*, 126, 1183
- Conselice, C. J., Rajgor, S., & Myers, R. 2008, *MNRAS*, 386, 909
- Cooke, J., Berrier, J. C., Barton, E. J., Bullock, J. S., & Wolfe, A. M. 2010, *MNRAS*, 403, 1020
- Cox, T. J., Dutta, S. N., Di Matteo, T., Hernquist, L., Hopkins, P. F., Robertson, B., & Springel, V. 2006a, *ApJ*, 650, 791
- Cox, T. J., Jonsson, P., Primack, J. R., & Somerville, R. S. 2006b, *MNRAS*, 373, 1013
- Cox, T. J., Jonsson, P., Somerville, R. S., Primack, J. R., & Dekel, A. 2008, *MNRAS*, 384, 386
- Cresci, G. et al. 2009, *ApJ*, 697, 115
- Croton, D. J. et al. 2006, *MNRAS*, 365, 11
- Cuesta, A. J., Prada, F., Klypin, A., & Moles, M. 2008, *MNRAS*, 389, 385
- Daddi, E., Cimatti, A., Renzini, A., Fontana, A., Mignoli, M., Pozzetti, L., Tozzi, P., & Zamorani, G. 2004, *ApJ*, 617, 746
- Daddi, E. et al. 2007, *ApJ*, 670, 156
- Dasyra, K. M. et al. 2006, *ApJ*, 651, 835
- Davé, R. 2008, *MNRAS*, 385, 147
- Davé, R. 2009, in *Astronomical Society of the Pacific Conference Series*, Vol. 419, *Astronomical Society of the Pacific Conference Series*, ed. S. Jogee, I. Marinova, L. Hao, & G. A. Blanc, 347–+
- Davies, R., Engel, H., Hicks, E., Förster Schreiber, N. M., Genzel, R., Tacconi, L. J., Eisenhauer, F., & Rabin, S. 2010, in *Society of Photo-Optical Instrumentation Engineers (SPIE) Conference Series*, Vol. 7736, *Society of Photo-Optical Instrumentation Engineers (SPIE) Conference Series*
- Davis, M., Efstathiou, G., Frenk, C. S., & White, S. D. M. 1985, *ApJ*, 292, 371
- De Lucia, G., & Blaizot, J. 2007, *MNRAS*, 375, 2
- De Propriis, R., Conselice, C. J., Liske, J., Driver, S. P., Patton, D. R., Graham, A. W., & Allen, P. D. 2007, *ApJ*, 666, 212
- de Ravel, L. et al. 2009, *A&A*, 498, 379
- Dekel, A., & Birnboim, Y. 2006, *MNRAS*, 368, 2
- Dekel, A. et al. 2009a, *Nature*, 457, 451
- Dekel, A., Sari, R., & Ceverino, D. 2009b, *ApJ*, 703, 785
- Dickinson, M. 2000, in *Royal Society of London Philosophical Transactions Series A*, Vol. 358, *Astronomy, physics and chemistry of H+3*, 2001–+
- Diemand, J., Kuhlen, M., & Madau, P. 2007a, *ApJ*, 657, 262

- . 2007b, *ApJ*, 667, 859
- D’Onghia, E., Mapelli, M., & Moore, B. 2008, *MNRAS*, 389, 1275
- Dubois, Y., & Teyssier, R. 2008, *A&A*, 477, 79
- Dunkley, J. et al. 2009, *ApJS*, 180, 306
- Efstathiou, G. 1992, *MNRAS*, 256, 43P
- Efstathiou, G., Davis, M., White, S. D. M., & Frenk, C. S. 1985, *ApJS*, 57, 241
- Eisenhauer, F. et al. 2003, in *Instrument Design and Performance for Optical/Infrared Ground-based Telescopes*. Edited by Iye, Masanori; Moorwood, Alan F. M. *Proceedings of the SPIE*, Volume 4841, pp. 1548-1561 (2003)., ed. M. Iye & A. F. M. Moorwood, 1548–1561
- Eliche-Moral, M. C. et al. 2010, *A&A*, 519, A55+
- Ellis, R. S. 2008, *Observations of the High Redshift Universe*, ed. Loeb, A., Ferrara, A., & Ellis, R. S., 259–364
- Elmegreen, B. G., Bournaud, F., & Elmegreen, D. M. 2008a, *ApJ*, 688, 67
- . 2008b, *ApJ*, 684, 829
- Elmegreen, B. G., & Elmegreen, D. M. 2005, *ApJ*, 627, 632
- . 2006, *ApJ*, 650, 644
- Elmegreen, B. G., Elmegreen, D. M., Fernandez, M. X., & Lemonias, J. J. 2009, *ApJ*, 692, 12
- Elmegreen, B. G., Elmegreen, D. M., Vollbach, D. R., Foster, E. R., & Ferguson, T. E. 2005, *ApJ*, 634, 101
- Elmegreen, D. M., Elmegreen, B. G., & Hirst, A. C. 2004, *ApJL*, 604, L21
- Elmegreen, D. M., Elmegreen, B. G., Ravindranath, S., & Coe, D. A. 2007, *ApJ*, 658, 763
- Engel, H. et al. 2010, *ApJ*, 724, 233
- Erb, D. K., Shapley, A. E., Pettini, M., Steidel, C. C., Reddy, N. A., & Adelberger, K. L. 2006, *ApJ*, 644, 813
- Erb, D. K., Steidel, C. C., Shapley, A. E., Pettini, M., & Adelberger, K. L. 2004, *ApJ*, 612, 122
- Faber, S. M., & Gallagher, J. S. 1979, *ARA&A*, 17, 135
- Fakhouri, O., & Ma, C. 2010, *MNRAS*, 401, 2245
- Fakhouri, O., Ma, C., & Boylan-Kolchin, M. 2010, *MNRAS*, 406, 2267
- Fakhouri, O., & Ma, C.-P. 2008, *MNRAS*, 386, 577
- . 2009, *MNRAS*, 394, 1825
- Fall, S. M., & Efstathiou, G. 1980, *MNRAS*, 193, 189
- Feng, J. L. 2010, *ARA&A*, 48, 495
- Ferguson, H. C., Dickinson, M., & Williams, R. 2000, *ARA&A*, 38, 667
- Field, G. B. 1965, *ApJ*, 142, 531
- Finlator, K., & Davé, R. 2008, *MNRAS*, 385, 2181
- Förster Schreiber, N. M. et al. 2009, *ApJ*, 706, 1364
- . 2006, *ApJ*, 645, 1062
- Förster Schreiber, N. M., Shapley, A. E., Erb, D. K., Genzel, R., Steidel, C. C., Bouché, N.,

- Cresci, G., & Davies, R. 2010, ApJ, submitted (astro-ph/10111507)
- Frenk, C. S., White, S. D. M., Davis, M., & Efstathiou, G. 1988, ApJ, 327, 507
- Frenk, C. S., White, S. D. M., Efstathiou, G., & Davis, M. 1985, Nature, 317, 595
- Fukugita, M., Hogan, C. J., & Peebles, P. J. E. 1998, ApJ, 503, 518
- Gan, J., Kang, X., van den Bosch, F. C., & Hou, J. 2010, MNRAS, 408, 2201
- Genel, S., Bouché, N., Naab, T., Sternberg, A., & Genzel, R. 2010a, ApJ, 719, 229
- Genel, S., Genzel, R., Bouché, N., Naab, T., & Sternberg, A. 2009, ApJ, 701, 2002
- Genel, S. et al. 2008, ApJ, 688, 789
- . 2010b, ApJL, submitted (astro-ph/10110433)
- Genzel, R. et al. 2008, ApJ, 687, 59
- . 2010, ApJ, submitted (astro-ph/10115360)
- . 2006, Nature, 442, 786
- Genzel, R., Tacconi, L. J., Rigopoulou, D., Lutz, D., & Tecza, M. 2001, ApJ, 563, 527
- Giavalisco, M. 2002, ARA&A, 40, 579
- Gingold, R. A., & Monaghan, J. J. 1977, MNRAS, 181, 375
- Giocoli, C., Tormen, G., & van den Bosch, F. C. 2008, MNRAS, 386, 2135
- Gnedin, N. Y., & Kravtsov, A. V. 2010, ApJ, 714, 287
- Gnedin, N. Y., Tassis, K., & Kravtsov, A. V. 2009, ApJ, 697, 55
- Goerdt, T., Dekel, A., Sternberg, A., Ceverino, D., Teyssier, R., & Primack, J. R. 2010, MNRAS, 407, 613
- Gott, III, J. R., Jurić, M., Schlegel, D., Hoyle, F., Vogeley, M., Tegmark, M., Bahcall, N., & Brinkmann, J. 2005, ApJ, 624, 463
- Gottlöber, S., Klypin, A., & Kravtsov, A. V. 2001, ApJ, 546, 223
- Governato, F., Baugh, C. M., Frenk, C. S., Cole, S., Lacey, C. G., Quinn, T., & Stadel, J. 1998, Nature, 392, 359
- Governato, F. et al. 2010, Nature, 463, 203
- . 2009, MNRAS, 398, 312
- Governato, F., Gardner, J. P., Stadel, J., Quinn, T., & Lake, G. 1999, AJ, 117, 1651
- Gunn, J. E., & Gott, III, J. R. 1972, ApJ, 176, 1
- Guo, Q., White, S., Li, C., & Boylan-Kolchin, M. 2010, MNRAS, 404, 1111
- Guo, Q., & White, S. D. M. 2008, MNRAS, 384, 2
- . 2009, MNRAS, 396, 39
- Guth, A. H. 1981, Phys. Rev. D, 23, 347
- Guth, A. H., & Pi, S. 1982, Physical Review Letters, 49, 1110
- . 1985, Phys. Rev. D, 32, 1899
- Haardt, F., & Madau, P. 2001, in Clusters of Galaxies and the High Redshift Universe Observed in X-rays, ed. D. M. Neumann & J. T. V. Tran
- Harker, G., Cole, S., Helly, J., Frenk, C., & Jenkins, A. 2006, MNRAS, 367, 1039

- Harrison, E. R. 1970, *Phys. Rev. D*, 1, 2726
- Hausman, M. A., & Ostriker, J. P. 1978, *ApJ*, 224, 320
- Hawking, S. W. 1982, *Physics Letters B*, 115, 295
- Hayashi, E., Navarro, J. F., Taylor, J. E., Stadel, J., & Quinn, T. 2003, *ApJ*, 584, 541
- Heckman, T. M. 2003, in *Revista Mexicana de Astronomia y Astrofisica*, vol. 27, Vol. 17, *Revista Mexicana de Astronomia y Astrofisica Conference Series*, ed. V. Avila-Reese, C. Firmani, C. S. Frenk, & C. Allen, 47–55
- Heckman, T. M., Armus, L., & Miley, G. K. 1990, *ApJS*, 74, 833
- Heckman, T. M., Lehnert, M. D., & Armus, L. 1993, in *Astrophysics and Space Science Library*, Vol. 188, *The Environment and Evolution of Galaxies*, ed. J. M. Shull & H. A. Thronson, 455–+
- Heckman, T. M., Lehnert, M. D., Strickland, D. K., & Armus, L. 2000, *ApJS*, 129, 493
- Heitmann, K. et al. 2008, *Computational Science and Discovery*, 1, 015003
- Helly, J. C., Cole, S., Frenk, C. S., Baugh, C. M., Benson, A., & Lacey, C. 2003, *MNRAS*, 338, 903
- Hernquist, L. 1989, *Nature*, 340, 687
- . 1992, *ApJ*, 400, 460
- Hernquist, L., & Mihos, J. C. 1995, *ApJ*, 448, 41
- Hoefl, M., & Gottloeber, S. 2010, *ArXiv e-prints*
- Hoekstra, H., Yee, H. K. C., & Gladders, M. D. 2002, *ApJ*, 577, 595
- Hopkins, A. M., & Beacom, J. F. 2006, *ApJ*, 651, 142
- Hopkins, P. F. et al. 2010a, *ApJ*, 715, 202
- Hopkins, P. F., Cox, T. J., Kereš, D., & Hernquist, L. 2008a, *ApJS*, 175, 390
- Hopkins, P. F., Cox, T. J., Younger, J. D., & Hernquist, L. 2009a, *ApJ*, 691, 1168
- Hopkins, P. F. et al. 2010b, *ApJ*, 724, 915
- Hopkins, P. F., Hernquist, L., Cox, T. J., Dutta, S. N., & Rothberg, B. 2008b, *ApJ*, 679, 156
- Hopkins, P. F., & Quataert, E. 2010, *MNRAS*, 407, 1529
- Hopkins, P. F. et al. 2009b, *MNRAS*, 397, 802
- Immeli, A., Samland, M., Gerhard, O., & Westera, P. 2004a, *A&A*, 413, 547
- Immeli, A., Samland, M., Westera, P., & Gerhard, O. 2004b, *ApJ*, 611, 20
- Iocco, F., Mangano, G., Miele, G., Pisanti, O., & Serpico, P. D. 2009, *Physics Reports*, 472, 1
- Jenkins, A., Frenk, C. S., White, S. D. M., Colberg, J. M., Cole, S., Evrard, A. E., Couchman, H. M. P., & Yoshida, N. 2001, *MNRAS*, 321, 372
- Jiang, C. Y., Jing, Y. P., Faltenbacher, A., Lin, W. P., & Li, C. 2008, *ApJ*, 675, 1095
- Johansson, P. H., Naab, T., & Burkert, A. 2009, *ApJ*, 690, 802
- Jonsson, P. 2006, *MNRAS*, 372, 2
- Jonsson, P., Groves, B. A., & Cox, T. J. 2010, *MNRAS*, 403, 17
- Joung, M. R., Cen, R., & Bryan, G. L. 2009, *ApJL*, 692, L1

- Katz, N., & Gunn, J. E. 1991, *ApJ*, 377, 365
- Katz, N., Hernquist, L., & Weinberg, D. H. 1992, *ApJL*, 399, L109
- . 1999, *ApJ*, 523, 463
- Katz, N., Weinberg, D. H., & Hernquist, L. 1996, *ApJS*, 105, 19
- Katz, N., & White, S. D. M. 1993, *ApJ*, 412, 455
- Kauffmann, G., Colberg, J. M., Diaferio, A., & White, S. D. M. 1999, *MNRAS*, 307, 529
- Kauffmann, G., Li, C., & Heckman, T. M. 2010, *MNRAS*, 1446
- Kauffmann, G., & White, S. D. M. 1993, *MNRAS*, 261, 921
- Kauffmann, G., White, S. D. M., & Guiderdoni, B. 1993, *MNRAS*, 264, 201
- Kazantzidis, S., Magorrian, J., & Moore, B. 2004, *ApJ*, 601, 37
- Kennicutt, R. C. 1998, *ARA&A*, 36, 189
- Kereš, D., & Hernquist, L. 2009, *ApJL*, 700, L1
- Kereš, D., Katz, N., Fardal, M., Davé, R., & Weinberg, D. H. 2009, *MNRAS*, 395, 160
- Kereš, D., Katz, N., Weinberg, D. H., & Davé, R. 2005, *MNRAS*, 363, 2
- Khochfar, S., & Silk, J. 2006, *MNRAS*, 370, 902
- Kitzbichler, M. G., & White, S. D. M. 2008, *MNRAS*, 391, 1489
- Klypin, A., Gottlöber, S., Kravtsov, A. V., & Khokhlov, A. M. 1999, *ApJ*, 516, 530
- Klypin, A., Trujillo-Gomez, S., & Primack, J. 2010, *ArXiv e-prints*
- Komatsu, E. et al. 2009, *ApJS*, 180, 330
- Kravtsov, A. 2010, *Advances in Astronomy*, 2010
- Krumholz, M. R., & Dekel, A. 2010, *MNRAS*, 406, 112
- Lacey, C., & Cole, S. 1993, *MNRAS*, 262, 627
- . 1994, *MNRAS*, 271, 676
- Law, D. R., Steidel, C. C., Erb, D. K., Larkin, J. E., Pettini, M., Shapley, A. E., & Wright, S. A. 2007, *ApJ*, 669, 929
- Le Fèvre, O. et al. 2000, *MNRAS*, 311, 565
- Li, Y., Mo, H. J., van den Bosch, F. C., & Lin, W. P. 2007, *MNRAS*, 379, 689
- Lilly, S. et al. 1998, *ApJ*, 500, 75
- Lin, L. et al. 2004, *ApJL*, 617, L9
- . 2008, *ApJ*, 681, 232
- Lo Faro, B., Monaco, P., Vanzella, E., Fontanot, F., Silva, L., & Cristiani, S. 2009, *MNRAS*, 399, 827
- Lotz, J. M. et al. 2008a, *ApJ*, 672, 177
- Lotz, J. M., Jonsson, P., Cox, T. J., & Primack, J. R. 2008b, *MNRAS*, 391, 1137
- . 2010a, *MNRAS*, 404, 590
- . 2010b, *MNRAS*, 404, 575
- Lucy, L. B. 1977, *AJ*, 82, 1013
- Ludlow, A. D., Navarro, J. F., Springel, V., Jenkins, A., Frenk, C. S., & Helmi, A. 2009, *ApJ*,

692, 931

- Lukić, Z., Heitmann, K., Habib, S., Bashinsky, S., & Ricker, P. M. 2007, *ApJ*, 671, 1160
- Lukić, Z., Reed, D., Habib, S., & Heitmann, K. 2009, *ApJ*, 692, 217
- Lynden-Bell, D. 1967, *MNRAS*, 136, 101
- Mac Low, M., & Ferrara, A. 1999, *ApJ*, 513, 142
- Maciejewski, M., Vogelsberger, M., White, S. D. M., & Springel, V. 2010, *MNRAS*, submitted (astro-ph/10102491)
- Madau, P., Diemand, J., & Kuhlen, M. 2008, *ApJ*, 679, 1260
- Madau, P., Ferguson, H. C., Dickinson, M. E., Giavalisco, M., Steidel, C. C., & Fruchter, A. 1996, *MNRAS*, 283, 1388
- Maller, A. H., & Bullock, J. S. 2004, *MNRAS*, 355, 694
- Maller, A. H., Katz, N., Kereš, D., Davé, R., & Weinberg, D. H. 2006, *ApJ*, 647, 763
- Marchesini, D., & van Dokkum, P. G. 2007, *ApJL*, 663, L89
- Martin, C. L. 1998, *ApJ*, 506, 222
- 1999, *ApJ*, 513, 156
- 2005, *ApJ*, 621, 227
- Masjedi, M., Hogg, D. W., & Blanton, M. R. 2008, *ApJ*, 679, 260
- McBride, J., Fakhouri, O., & Ma, C. 2009, *MNRAS*, 398, 1858
- Merritt, D. 1983, *ApJ*, 264, 24
- Mihos, J. C., & Hernquist, L. 1996, *ApJ*, 464, 641
- Milgrom, M. 1983a, *ApJ*, 270, 371
- 1983b, *ApJ*, 270, 365
- Mo, H. J., Mao, S., & White, S. D. M. 1998, *MNRAS*, 295, 319
- 1999, *MNRAS*, 304, 175
- Mo, H. J., & White, S. D. M. 2002, *MNRAS*, 336, 112
- Moore, B., Ghigna, S., Governato, F., Lake, G., Quinn, T., Stadel, J., & Tozzi, P. 1999, *ApJL*, 524, L19
- Moster, B. P., Somerville, R. S., Maulbetsch, C., van den Bosch, F. C., Macciò, A. V., Naab, T., & Oser, L. 2010, *ApJ*, 710, 903
- Murali, C., Katz, N., Hernquist, L., Weinberg, D. H., & Davé, R. 2002, *ApJ*, 571, 1
- Murray, N., Ménard, B., & Thompson, T. A. 2010a, ArXiv e-prints
- Murray, N., Quataert, E., & Thompson, T. A. 2005, *ApJ*, 618, 569
- 2010b, *ApJ*, 709, 191
- Naab, T., & Burkert, A. 2003, *ApJ*, 597, 893
- Naab, T., Jesseit, R., & Burkert, A. 2006a, *MNRAS*, 372, 839
- Naab, T., Johansson, P. H., & Ostriker, J. P. 2009, *ApJL*, 699, L178
- Naab, T., Johansson, P. H., Ostriker, J. P., & Efstathiou, G. 2007, *ApJ*, 658, 710
- Naab, T., Khochfar, S., & Burkert, A. 2006b, *ApJL*, 636, L81

- Navarro, J. F., Frenk, C. S., & White, S. D. M. 1997, *ApJ*, 490, 493
- Navarro, J. F., & Steinmetz, M. 1997, *ApJ*, 478, 13
- Navarro, J. F., & White, S. D. M. 1993, *MNRAS*, 265, 271
- . 1994, *MNRAS*, 267, 401
- Neistein, E., & Dekel, A. 2008a, *MNRAS*, 383, 615
- . 2008b, *MNRAS*, 388, 1792
- Neistein, E., Macciò, A. V., & Dekel, A. 2010, *MNRAS*, 403, 984
- Neistein, E., van den Bosch, F. C., & Dekel, A. 2006, *MNRAS*, 372, 933
- Neistein, E., & Weinmann, S. M. 2010, *MNRAS*, 405, 2717
- Nipoti, C., Londrillo, P., & Ciotti, L. 2003, *MNRAS*, 342, 501
- Noeske, K. G. et al. 2007, *ApJL*, 660, L43
- Noguchi, M. 1999, *ApJ*, 514, 77
- Nordon, R. et al. 2010, *A&A*, 518, L24+
- Ocvirk, P., Pichon, C., & Teyssier, R. 2008, *MNRAS*, 390, 1326
- Okamoto, T., & Frenk, C. S. 2009, *MNRAS*, 399, L174
- Oort, J. H. 1940, *ApJ*, 91, 273
- Oppenheimer, B. D., & Davé, R. 2006, *MNRAS*, 373, 1265
- . 2008, *MNRAS*, 387, 577
- Oser, L., Ostriker, J. P., Naab, T., Johansson, P. H., & Burkert, A. 2010, *ApJ*, submitted (astro-ph/10101381)
- Ostriker, J. P., Peebles, P. J. E., & Yahil, A. 1974, *ApJL*, 193, L1
- Patton, D. R., & Atfield, J. E. 2008, *ApJ*, 685, 235
- Patton, D. R., Carlberg, R. G., Marzke, R. O., Pritchet, C. J., da Costa, L. N., & Pellegrini, P. S. 2000, *ApJ*, 536, 153
- Patton, D. R., Pritchet, C. J., Yee, H. K. C., Ellingson, E., & Carlberg, R. G. 1997, *ApJ*, 475, 29
- Peebles, P. J. E. 1982, *ApJL*, 263, L1
- Perlmutter, S. et al. 1999, *ApJ*, 517, 565
- Pettini, M., Steidel, C. C., Adelberger, K. L., Dickinson, M., & Giavalisco, M. 2000, *ApJ*, 528, 96
- Press, W. H., & Schechter, P. 1974, *ApJ*, 187, 425
- Purcell, C. W., Bullock, J. S., & Zentner, A. R. 2007, *ApJ*, 666, 20
- Rees, M. J. 1986, *MNRAS*, 218, 25P
- Riess, A. G. et al. 1998, *AJ*, 116, 1009
- Robertson, B., Bullock, J. S., Cox, T. J., Di Matteo, T., Hernquist, L., Springel, V., & Yoshida, N. 2006, *ApJ*, 645, 986
- Robertson, B. E., & Bullock, J. S. 2008, *ApJL*, 685, L27
- Romano-Díaz, E., Shlosman, I., Heller, C., & Hoffman, Y. 2010, *ApJ*, 716, 1095
- Rubin, V. C., Ford, W. K. J., & Thonnard, N. 1980, *ApJ*, 238, 471

- Rupke, D. S., Veilleux, S., & Sanders, D. B. 2005, *ApJS*, 160, 115
- Ryan, Jr., R. E., Cohen, S. H., Windhorst, R. A., & Silk, J. 2008, *ApJ*, 678, 751
- Ryu, D., Ostriker, J. P., Kang, H., & Cen, R. 1993, *ApJ*, 414, 1
- Sales, L. V., Navarro, J. F., Schaye, J., Dalla Vecchia, C., Springel, V., Haas, M. R., & Helmi, A. 2009, *MNRAS*, 399, L64
- Sales, L. V., Navarro, J. F., Schaye, J., Vecchia, C. D., Springel, V., & Booth, C. M. 2010, *MNRAS*, 1326
- Sanders, D. B., & Mirabel, I. F. 1996, *ARA&A*, 34, 749
- Saro, A., Borgani, S., Tornatore, L., De Lucia, G., Dolag, K., & Murante, G. 2009, *MNRAS*, 392, 795
- Scannapieco, C., Tissera, P. B., White, S. D. M., & Springel, V. 2008, *MNRAS*, 389, 1137
- Scannapieco, E., & Brüggen, M. 2010, *MNRAS*, 405, 1634
- Schaye, J., & Dalla Vecchia, C. 2008, *MNRAS*, 383, 1210
- Semelin, B., & Combes, F. 2005, *A&A*, 441, 55
- Shapiro, K. L., Genzel, R., & Förster Schreiber, N. M. 2010, *MNRAS*, 403, L36
- Shapiro, K. L. et al. 2008, *ApJ*, 682, 231
- Shen, S., Wadsley, J., & Stinson, G. 2010, *MNRAS*, 407, 1581
- Sheth, R. K., & Tormen, G. 2002, *MNRAS*, 329, 61
- Silk, J., & Wilson, M. L. 1981, *ApJL*, 244, L37
- Skibba, R. A., & Sheth, R. K. 2009, *MNRAS*, 392, 1080
- Somerville, R. S., & Kolatt, T. S. 1999, *MNRAS*, 305, 1
- Somerville, R. S., Lemson, G., Kolatt, T. S., & Dekel, A. 2000, *MNRAS*, 316, 479
- Somerville, R. S., & Primack, J. R. 1999, *MNRAS*, 310, 1087
- Somerville, R. S., Primack, J. R., & Faber, S. M. 2001, *MNRAS*, 320, 504
- Sommer-Larsen, J., Götz, M., & Portinari, L. 2003, *ApJ*, 596, 47
- Spergel, D. N. et al. 2007, *ApJS*, 170, 377
- Spinrad, H., & Djorgovski, S. 1984, *ApJL*, 285, L49
- Springel, V. 2005, *MNRAS*, 364, 1105
- . 2010, *ARA&A*, 48, 391
- Springel, V., Di Matteo, T., & Hernquist, L. 2005a, *MNRAS*, 361, 776
- Springel, V., Frenk, C. S., & White, S. D. M. 2006, *Nature*, 440, 1137
- Springel, V., & Hernquist, L. 2002, *MNRAS*, 333, 649
- . 2003a, *MNRAS*, 339, 289
- . 2003b, *MNRAS*, 339, 312
- . 2005, *ApJL*, 622, L9
- Springel, V. et al. 2008, *MNRAS*, 391, 1685
- . 2005b, *Nature*, 435, 629
- Springel, V., White, S. D. M., Tormen, G., & Kauffmann, G. 2001, *MNRAS*, 328, 726

- Steidel, C. C., Erb, D. K., Shapley, A. E., Pettini, M., Reddy, N., Bogosavljević, M., Rudie, G. C., & Rakic, O. 2010, *ApJ*, 717, 289
- Steidel, C. C., Giavalisco, M., Pettini, M., Dickinson, M., & Adelberger, K. L. 1996, *ApJL*, 462, L17+
- Steidel, C. C., & Hamilton, D. 1992, *AJ*, 104, 941
- . 1993, *AJ*, 105, 2017
- Steidel, C. C., Shapley, A. E., Pettini, M., Adelberger, K. L., Erb, D. K., Reddy, N. A., & Hunt, M. P. 2004, *ApJ*, 604, 534
- Steinmetz, M., & Navarro, J. F. 2002, *New Astronomy*, 7, 155
- Stewart, K. R. 2009, in *Astronomical Society of the Pacific Conference Series*, Vol. 419, *Astronomical Society of the Pacific Conference Series*, ed. S. Jogee, I. Marinova, L. Hao, & G. A. Blanc, 243–+
- Stewart, K. R., Bullock, J. S., Barton, E. J., & Wechsler, R. H. 2009, *ApJ*, 702, 1005
- Stewart, K. R., Bullock, J. S., Wechsler, R. H., Maller, A. H., & Zentner, A. R. 2008, *ApJ*, 683, 597
- Stinson, G., Seth, A., Katz, N., Wadsley, J., Governato, F., & Quinn, T. 2006, *MNRAS*, 373, 1074
- Stone, J. M., & Norman, M. L. 1992, *ApJS*, 80, 753
- Tacconi, L. J. et al. 2010, *Nature*, 463, 781
- . 2008, *ApJ*, 680, 246
- . 2006, *ApJ*, 640, 228
- Taylor, J. E., & Babul, A. 2001, *ApJ*, 559, 716
- Teyssier, R. 2002, *A&A*, 385, 337
- Teyssier, R., Chapon, D., & Bournaud, F. 2010, *ApJL*, 720, L149
- Thompson, T. A., Quataert, E., & Murray, N. 2005, *ApJ*, 630, 167
- Tinker, J., Kravtsov, A. V., Klypin, A., Abazajian, K., Warren, M., Yepes, G., Gottlöber, S., & Holz, D. E. 2008, *ApJ*, 688, 709
- Tonini, C., Maraston, C., Thomas, D., Devriendt, J., & Silk, J. 2010, *MNRAS*, 403, 1749
- Toomre, A. 1964, *ApJ*, 139, 1217
- Toomre, A. 1977, in *Evolution of Galaxies and Stellar Populations*, 401
- Toomre, A., & Toomre, J. 1972, *ApJ*, 178, 623
- Tornatore, L., Borgani, S., Viel, M., & Springel, V. 2010, *MNRAS*, 402, 1911
- van Dokkum, P. G. 2005, *AJ*, 130, 2647
- van Dokkum, P. G. et al. 2008, *ApJL*, 677, L5
- van Starckenburg, L., van der Werf, P. P., Franx, M., Labbé, I., Rudnick, G., & Wuyts, S. 2008, *A&A*, 488, 99
- Veilleux, S., Cecil, G., & Bland-Hawthorn, J. 2005, *ARA&A*, 43, 769
- Wadsley, J. W., Stadel, J., & Quinn, T. 2004, *New Astronomy*, 9, 137
- Walter, F., Weiss, A., & Scoville, N. 2002, *ApJL*, 580, L21

- Wang, J. et al. 2010, ArXiv e-prints
- Warren, M. S., Abazajian, K., Holz, D. E., & Teodoro, L. 2006, ApJ, 646, 881
- Weil, M. L., Eke, V. R., & Efstathiou, G. 1998, MNRAS, 300, 773
- Weinberg, D. H., Hernquist, L., & Katz, N. 2002, ApJ, 571, 15
- Weiner, B. J. et al. 2009, ApJ, 692, 187
- Wetzel, A. R., Cohn, J. D., & White, M. 2009, MNRAS, 394, 2182
- Wetzel, A. R., & White, M. 2010, MNRAS, 403, 1072
- White, M. 2001, A&A, 367, 27
- . 2002, ApJS, 143, 241
- White, S. D. M. 1978, MNRAS, 184, 185
- White, S. D. M., & Frenk, C. S. 1991, ApJ, 379, 52
- White, S. D. M., & Rees, M. J. 1978, MNRAS, 183, 341
- Williams, R. E. et al. 1996, AJ, 112, 1335
- Wilson, M. L., & Silk, J. 1981, ApJ, 243, 14
- Yang, J., Turner, M. S., Schramm, D. N., Steigman, G., & Olive, K. A. 1984, ApJ, 281, 493
- Zehavi, I. et al. 2005, ApJ, 630, 1
- Zel'Dovich, Y. B. 1970, A&A, 5, 84
- . 1972, MNRAS, 160, 1P
- Zhang, D., & Thompson, T. A. 2010, ApJL, submitted (astro-ph/10054691)
- Zhang, J., Fakhouri, O., & Ma, C.-P. 2008a, MNRAS, 389, 1521
- Zhang, J., Ma, C.-P., & Fakhouri, O. 2008b, MNRAS, 387, L13
- Zwicky, F. 1933, Helvetica Physica Acta, 6, 110

Acknowledgements

First I would like to thank my mentors. I am grateful to Reinhard Genzel, my advisor, for the exciting scientific environment that he creates, for being always so supportive and encouraging me to pursue my interests, and for inspiring me with his amazing knowledge, sharp perception and creative thinking. I am grateful to Thorsten Naab for his great spirit and great ideas, for investing his time in guiding me through my first steps in the field and sharing his expertise with me. I am grateful to Nicolas Bouché for understanding his role as "my representative" in the Thesis Committee meetings in the broadest way possible and being always on my side, helping me with anything down to the smallest detail, and most of all - being a friend. And special thanks to Amiel Sternberg, who introduced me to the worlds of research and of Astrophysics, and from whom I first learned, with awe, how to approach scientific problems. Without him I would not be here, writing my PhD thesis in Garching. There is no way I could thank Amiel enough for shaping my life and making it what it is today.

I enjoyed very much working with the SINS team, and in particular I would like to thank Natascha Förster-Schreiber, Andi Burkert and Peter Johansson for the enjoyable experience of learning from them. I am very grateful to Linda Tacconi for always being attentive and helpful, and to Thomas Ott for never saying "no" to my requests...

Where would I be without my Amochette! It is a pleasure thanking Caroline, Margarita, Mona, Payel and Silvia, for their dearest friendship. I am so grateful for getting to know them, the charming and impressive people they are.

It is a great pleasure thanking my family and my Israeli friends - Ziv, Maya, Inbal, Yaron, Aviv, Tali, Daniel, Gal, Uri, Moshe, Idit, Noam and Nimrod - for making me feel that I still belong and being missed, and making me so happy on our infrequent reunions. I thank my aunt Varda for her love, and treasure the memories of my late great uncle Fima. Special thanks to my grandmother Zina, for her endless love and support (and supply of Plätzalech!).

Last but not least, I am indebted to my parents, Nava and Toly, who supported me with all their hearts on this PhD journey. I thank them for hosting me so wonderfully during my numerous visits to Israel, for coming here to Munich to visit me from time to time, for my dad's enthusiastic interest in my research and for my mom making sure that I did not miss any family news while I was away!

Curriculum Vitae

Formal Education

- 2006-2011 **Ph.D. in Astrophysics with Prof. Reinhard Genzel**
Max Planck Institute for Extraterrestrial Physics (MPE)
The Formation of Dark Matter Halos and High Redshift Galaxies
- 2002-2006 **B.Sc. in Physics**
Tel Aviv University
Summa Cum Laude
- 2002-2006 **B.Sc. in Electrical and Electronic Engineering**
Tel Aviv University
Magna Cum Laude

Additional Education and Research Experience

- 2009 **Summer Student**
Prospects in Theoretical Physics 2009 - Computational Astrophysics
Institute of Advanced Studies, Princeton
- 2007 **Summer Student**
NOVICOSMO 2007 - Galaxy Formation
Novigrad, Croatia
- 2004-2006 **Research Assistant with Prof. Amiel Sternberg**
Tel Aviv University
Chemical Evolution of Galaxies
- 2005 **Summer Student with Prof. Shlomit Tarem and Prof. Sylvia Schuh**
Summer Student Program
CERN

Employment History

- 2004-2005 **Programmer**
Siliquent Technologies / Broadcom
- 1998-2002 **Programmer**
Military Service, Israel Defense Forces (IDF)

Scholarships and Awards

- 2006-2011 **Research Fellowship**
International Max Planck Research School in Astrophysics (IMPRS)
- 2007,2010 **Marie Curie Host Fellowship for Early Stage Research Training**
- 2005 **Wolf Foundation Scholarship**
- 2004 **Tel Aviv University Rector Award**
- 2003 **Full scholarship for undergraduate studies**
Program for Outstanding Students, Tel Aviv University

Conference Contributions

- Santa Cruz Galaxy Workshop, Santa Cruz, CA, August 2010
- Galaxies in the Distant Universe: Dynamics and Early Evolution, Ringberg Castle, Germany, May 2010
- Galaxy Evolution: Emerging Insights and Future Challenges, Austin, TX, November 2008
- Galactic Structure and the Structure of Galaxies, Ensenada, Mexico, March 2008

Professional Talks at Astronomy Institutes

- Seminar, Canadian Institute for Theoretical Astrophysics (CITA), September 2010
- ITC Seminar, Harvard-Smithsonian Center for Astrophysics, September 2010
- Seminar, The American Museum of Natural History, September 2010
- Seminar, Columbia University, September 2010
- Theory Lunch, UC Berkeley, August 2010
- Astrophysics Seminar, Weizmann Institute of Science, December 2009
- Theory Lunch, UC Berkeley, July 2009
- Astrophysics Seminar, Hebrew University of Jerusalem, December 2008
- Astro Seminar, Tel Aviv University, December 2008

Professional Activities

- Referee for Nature

Publication List

- *Short-lived star-forming giant clumps in cosmological simulations of $z \approx 2$ disks*, **Genel, S.**, Naab, T., Genzel, R., Förster Schreiber, N. M., Sternberg, A., Oser, L., Johansson, P. H., Davé, R., Oppenheimer, B. D., Burkert, A., 2010 *The Astrophysical Journal Letters*, *submitted* [in press: arXiv:1011.0433]
- *The Growth of Dark Matter Halos: Evidence for Significant Smooth Accretion*, **Genel, S.**, Bouché, N., Naab, T., Sternberg, A., Genzel, R., 2010 *The Astrophysical Journal*, 719, 229
- *The Halo Merger Rate in the Millennium Simulation and Implications for Observed Galaxy Merger Fractions*, **Genel, S.**, Genzel, R., Bouché, N., Naab, T., Sternberg, A., 2009 *The Astrophysical Journal*, 701, 2002
- *Mergers and Mass Accretion Rates in Galaxy Assembly: The Millennium Simulation compared to Observations of $z \approx 2$ Galaxies*, **Genel, S.**, Genzel, R., Bouché, N., Sternberg, A., Naab, T., Förster Schreiber, N. M., Shapiro, K. L., Tacconi, L. J., Lutz, D., Cresci, G., Buschkamp, P., Davies, R. I., Hicks, E. K. S., 2008 *The Astrophysical Journal*, 688, 789
- *The Millennium Simulation Compared to Observations of $z \approx 2$ Galaxies*, **Genel, S.**, 2009 ASP Conference Series, Vol. 419
- *The SINS Survey of $z \sim 2$ Galaxy Kinematics: Properties of the Giant Star Forming Clumps*, Genzel, R., Newman, S., Jones, T., Förster Schreiber, N. M., Shapiro, K., **Genel, S.**, Lilly, S. J., Renzini, A., Tacconi, L. J., Bouché, N., Burkert, A., Cresci, G., Buschkamp, P., Carollo, C. M., Ceverino, D., Davies, R., Dekel, A., Eisenhauer, F., Hicks, E. K. S., Kurk, J., Lutz, D., Mancini, C., Naab, T., Peng, Y., Sternberg, A., Vergani, D., Zamorani, G., 2010 *The Astrophysical Journal*, *submitted* [in press: arXiv:1011.5360]

- *On the evolution of the intrinsic scatter in black hole versus galaxy mass relations*, Hirschmann, M., Khochfar, S., Burkert, A., Naab, T., **Genel, S.**, Somerville, R. S., 2010 Monthly Notices of the Royal Astronomical Society, 407, 1016
- *The Impact of Cold Gas Accretion Above a Mass Floor on Galaxy Scaling Relations*, Bouché, N., Dekel, A., Genzel, R., **Genel, S.**, Cresci, G., Förster Schreiber, N. M., Shapiro, K. L., Davies, R. I., Tacconi, L., 2010 The Astrophysical Journal, 718, 1001
- *Mergers in Lambda-CDM: Uncertainties in Theoretical Predictions and Interpretations of the Merger Rate*, Hopkins, P. F., Croton, D., Bundy, K., Khochfar, S., van den Bosch, F., Somerville, R. S., Wetzell, A., Keres, D., Hernquist, L., Stewart, K., Younger, J. D., **Genel, S.**, Ma, C.-P., 2010 The Astrophysical Journal, 724, 915
- *The SINS Survey: SINFONI Integral Field Spectroscopy of $z \sim 2$ Star-forming Galaxies*, Förster Schreiber, N. M., Genzel, R., Bouché, N., Cresci, G., Davies, R., Buschkamp, P., Shapiro, K., Tacconi, L. J., Hicks, E. K. S., **Genel, S.**, Shapley, A. E., Erb, D. K., Steidel, C. C., Lutz, D., Eisenhauer, F., Gillessen, S., Sternberg, A., Renzini, A., Cimatti, A., Daddi, E., Kurk, J., Lilly, S., Kong, X., Lehnert, M. D., Nesvadba, N., Verma, A., McCracken, H., Arimoto, N., Mignoli, M., Onodera, M., 2009 The Astrophysical Journal, 706, 1364
- *The SINS Survey: Broad Emission Lines in High-Redshift Star-Forming Galaxies*, Shapiro, K. L., Genzel, R., Quataert, E., Förster Schreiber, N. M., Davies, R., Tacconi, L., Armus, L., Bouché, N., Buschkamp, P., Cimatti, A., Cresci, G., Daddi, E., Eisenhauer, F., Erb, D. K., **Genel, S.**, Hicks, E. K. S., Lilly, S. J., Lutz, D., Renzini, A., Shapley, A., Steidel, C. C., Sternberg, A., 2009 The Astrophysical Journal, 701, 955
- *High-Redshift Star-Forming Galaxies: Angular Momentum and Baryon Fraction, Turbulent Pressure Effects and the Origin of Turbulence*, Burkert, A., Genzel, R., Bouché, N., Cresci, G., Khochfar, S., Sommer-Larsen, J., Sternberg, A., Naab, T., Förster Schreiber, N., Tacconi, L., Shapiro, K., Hicks, E., Lutz, D., Davies, R., Buschkamp, P., **Genel, S.**, 2009 The Astrophysical Journal, submitted [in press: arXiv:0907.4777]

-
- *The SINS Survey: Modeling the Dynamics of $z \sim 2$ Galaxies and the High- z Tully-Fisher Relation*, Cresci, G., Hicks, E. K. S., Genzel, R., Förster Schreiber, N. M., Davies, R., Bouché, N., Buschkamp, P., **Genel, S.**, Shapiro, K., Tacconi, L., Sommer-Larsen, J., Burkert, A., Eisenhauer, F., Gerhard, O., Lutz, D., Naab, T., Sternberg, A., Cimatti, A., Daddi, E., Erb, D. K., Kurk, J., Lilly, S. L., Renzini, A., Shapley, A., Steidel, C. C., Caputi, K., 2009 *The Astrophysical Journal*, 697, 115
 - *From Rings to Bulges: Evidence for Rapid Secular Galaxy Evolution at $z \sim 2$ from Integral Field Spectroscopy in the SINS Survey*, Genzel, R., Burkert, A., Bouché, N., Cresci, G., Förster Schreiber, N. M., Shapley, A., Shapiro, K., Tacconi, L. J., Buschkamp, P., Cimatti, A., Daddi, E., Davies, R., Eisenhauer, F., Erb, D. K., **Genel, S.**, Gerhard, O., Hicks, E., Lutz, D., Naab, T., Ott, T., Rabien, S., Renzini, A., Steidel, C. C., Sternberg, A., Lilly, S. J., 2008 *The Astrophysical Journal*, 687, 59
 - *Submillimeter Galaxies at $z \sim 2$: Evidence for Major Mergers and Constraints on Lifetimes, IMF, and CO-H₂ Conversion Factor*, Tacconi, L. J., Genzel, R., Smail, I., Neri, R., Chapman, S. C., Ivison, R. J., Blain, A., Cox, P., Omont, A., Bertoldi, F., Greve, T., Förster Schreiber, N. M., **Genel, S.**, Lutz, D., Swinbank, A. M., Shapley, A. E., Erb, D. K., Cimatti, A., Daddi, E., Baker, A. J., 2008 *The Astrophysical Journal*, 680, 246